Inaugural dissertation

for

obtaining the doctoral degree

of the

Combined Faculty of Mathematics, Engineering and Natural Sciences

of the

Ruprecht - Karls - University

Heidelberg

Presented by

Rajwinder Singh (M.Sc.)

Born in: Patiala, India

Oral examination: 10 May 2022

Development of a mesoscale oblique plane microscope for freely moving animals

Referees: Prof. Dr. Alexis Maizel
Dr. Jonas Ries

Abstract

Nematostella Vectensis belongs to the phylum cnidaria which is the closest relative of bilaterians and has become an important model organism for evolutionary developmental biology. However, because of its high light sensitivity, large size, and constant need to move freely in order to properly develop and survive, *in toto* live imaging of Nematostella is a major challenge in microscopy. Several important questions, e.g. how animal behavior during muscle hydraulics guides the animal morphology and how neuronal dynamics control muscle movements and body deformations that are necessary for animal development remain unanswered. In the field of microscopy, light-sheet fluorescence microscopy (LSFM) has emerged as a preferred tool to image light-sensitive large samples due to optical sectioning and high-speed functional imaging capabilities. In a conventional light microscope, the specimen needs to be embedded in agarose and placed within a narrow space between orthogonally lying illumination and detection objectives. These constraints however make it impossible to use on Nematostella or other freely moving animals. On the contrary, recently developed, so-called single objective light-sheet microscopes are capable of imaging freely moving animals, but the lateral field of view (FOV) in such existing techniques is limited to $1\times1\,\mathrm{mm}^2$. To overcome these challenges, in this thesis I developed **MesoOPM**-an oblique plane microscope for imaging freely moving specimens at mesoscopic scales that provide light-sheet scanning based rapid volumetric imaging capability with cellular resolution and over 2 mm FOV. By utilizing a long working distance illumination objective and placing it at 65° angle to the optic axis of the detection objective, we can maintain the open-top configuration that allows easy sample mounting. Furthermore, the rapid tilt-invariant light-sheet scanning along the image plane of the detection objective is achieved by precisely synchronizing an electrically tunable lens with the galvo scanner in the illumination arm. I performed meticulous optical design optimization of the microscope to maximize the spatial resolution under these conditions. The experimental PSF of the MesoOPM was then measured with sub-diffraction size beads and found to be $1.62\times2.81\,\mu\mathrm{m}^2$ in lateral dimensions and the 5.27 µm in the axial dimension. The total FOV offered by MesoOPM is $1.56\times1.56\times0.24\,\mathrm{mm}^3$. I would like to point out that the lateral FOV $1.56\times1.56\,\mathrm{mm}^2$ is limited by the camera chip size, although the system is capable of imaging over the FOV of $2.0\times2.0\,\mathrm{mm}^2$. Finally, the imaging capabilities of the microscope are showcased by imaging the muscle structure and the nervous system of a freely moving live Nematostella at

300 frames per second over the FOV of $1.56 \times 0.78 \times 0.24\,\mathrm{mm}^3$ in two seconds. This is the first-ever report of imaging 3d volume of a live freely moving Nematostella in its entirety using a fluorescence microscope. This technology opens up a whole new direction of imaging an entire freely moving specimen which will allow us to study the interactions between animal behavior and the environment by visualizing the underlying cellular structures, which so far has been a challenge.

Zusammenfassung

Die Seeanemone Nematostella vectensis gehört zu dem Phylum Cnidaria, dem engsten Verwandten von bilateralen Tieren, und hat sich daher zu einem wichtigen Modellorganismus für die evolutionäre Entwicklungsbiologie entwickelt. Allerdings bleibt eine große Herausforderung in der Mikroskopie die in toto Lebend-Bildgebung von Nematostella wegen der hohen Lichtsensitivität, der Größe und dem konstanten Anforderung, sich frei zu bewegen, um sich ordnungsgemäß entwickeln und überleben zu können. Einige wichtige Fragestellungen sind nach wie vor nicht beantwortet, beispielsweise wie das Tierverhalten während der Muskelhydraulik die Morphologie lenkt und wie die neuronale Dynamik die Muskelbewegung und die Körperdeformation kontrolliert, die für die Tierentwicklung notwendig ist. In dem Feld der Mikroskopie hat sich die Lichtscheibenfluoreszenzmikroskopie (LSFM) zu einer bevorzugten Methode entwickelt, um große und lichtsensitive Proben abzubilden, da LSFM optische Schnittdarstellungen und damit einhergehende funktionale Hochgeschwindigkeits-Bildgebung ermöglicht. In einem konventionellem Lichtmikroskop muss die Probe in Agarose eingebettet und in einen schmalen Bereich zwischen orthogonal-liegenden Beleuchtungs- und Detektionsobjektiven platziert werden. Diese Einschränkung macht es allerdings unmöglich, Nematostella oder andere, sich frei bewegende Tiere, abzubilden. Im Gegensatz hierzu sind neuartige, sogenannte Einzelobjektiv-Lichtscheibenmikroskope dazu in der Lage, freibewegliche Tiere abzubilden. Allerdings ist das laterale Sichtfeld in diesen Methoden auf $1\times1\,\mathrm{mm}^2$ limitiert. Um dieses Problem zu überwinden, habe ich in dieser Dissertation ein Schräg-Ebene-Mikroskop für die Bildgebung von freibeweglichen Proben im mesoskopischen Maßstab (MesoOPM) entwickelt. Diese Methode ermöglicht Lichtscheibenmikroskop-basierte, schnelle, volumetrische Bildgebung mit einer zellulären Auflösung und einem Sichtfeld von über 2 mm. Durch die Nutzung eines Beleuchtungsobjektives mit langer Arbeitsdistanz und dessen Platzierung bei einem Winkel von 65 Grad zur optischen Achse des Detektionsobjektives kann die offene Konfiguration beibehalten werden, welches eine einfache Platzierung der Probe ermöglicht. Des Weiteren wird das schnelle und neigungsinvariante Scannen mit Lichtscheiben dadurch erzielt, dass eine elektrisch kontrollierbare Linse präzise mit dem Galvanometer Scanner in dem Beleuchtungsarm präzise synchronisiert wird. Unter diesen Bedingungen habe ich eine sorgfältige Optimierung des optischen Designs des Mikroskops durchgeführt, um die räumliche Auflösung zu maximieren. Das experimentale Sichtfeld des MesoOPM wurde anschließend mithilfe von diffraktionslimitierten Kügelchen gemessen, was einen Wert von $1,62\times2.81\,\mu\mathrm{m}^2$ in der lateralen Dimension und 5.27 µm in der axialen Dimension ergeben hat. Letztendlich wurde das bildgebende Leistungsvermögen des Mikroskops demonstriert, in dem die Muskelstrukturen und das Nervensystem eines freibeweglichen Nematostella

bei 300 Bildern pro Sekunde abgebildet wurde, wobei das gesamte Tier über ein Sichtfeld von $1,56 \times 0,78 \times 0.24\,\mathrm{mm}^3$ innerhalb von zwei Sekunden erfasst wurde.

Acknowledgements

The work presented in this thesis has been carried out in the Prevedel group at the European Molecular Biology Laboratory (EMBL) in Heidelberg, Germany. I am grateful to Robert Prevedel for giving me chance to work on this exciting project in his lab. He has always been very supportive and encouraging. I really enjoyed the freedom I got while working in the Prevedel lab. I deeply appreciate the fact that he took me under his wings after the departure of Lars Hufnagel from EMBL.

Many thanks to Rory Power, whose guidance during this whole project has been invaluable. I am grateful for your expert help and the discussions about the microscopy design and debugging, without which this project would not be possible.

Special thanks go to Kaushikaram Subramanian and Aissam Ikmi for providing me with biological samples for the validation of microscope setup and taking part in discussions and generating new ideas.

I would also like to extend my gratitude to my thesis advisory committee (TAC) members: Alexander Aulehla, Steffen Lemke, and Pierre Neveu for taking the time to give valuable input to the project. Also thanks to Jonas Ries and Alexis Maizel for agreeing to be part of the thesis defense committee at the last minute.

I would also like to thank Lars Hufnagel who recruited me as his student at EMBL and introduced me to the world of light-sheet microscopy. Even after he departed from EMBL, he continued to be involved in the discussions about my work.

Thanks to Alejandro Ortiz, Tim Hettinger, Leo Burger and all other members of the electronics and mechanical workshop. Their help during the development of the microscope has been invaluable.

I am grateful to enjoy the company of great people from the Hufnagel and the Prevedel group during my stay at EMBL: Ulla, Nils Norlin, Nils Wagner, Tatjana, Lina, Carlo, Juan, Jakub, Fan, Ling, Amr, Marina, Ivo, Octave, Emmanuel, Nikita. Special thanks to Dimitri for sticking around until almost the end of my time at EMBL and I am glad we got to spend time together. Thanks to Balint for staying in touch and being available for help when needed.

Many thanks to Nikita, Octave, Fan, Ivo, Juan, Carlo, Kaushik, and Robert for reading parts of the thesis and giving constructive feedback. Also, thanks to Mathias and Jakob from my predoc batch for helping me to translate the abstract from English to German.

I would also like to thank my friends: Alberto, Aliex, Can, Carol, Chris, Erica, Ivan, Kristina, Mukesh, Natalie, Sara, Vasileos, Veronika, Vikas, and all the other Predocs of the 2017 and 2018 cohort for making this experience of PhD a pleasant one when I was not working in the lab. Thanks for the quality time we spent during our get-togethers on weekends and the trips we went together!

Special thanks to Nestor and Veronika, teachers of the salsa club EMBL and all the other members: Jonas, Ines, Juan, Gretel, Cynthia, Robin, Min, Patrick, Bettina for the dance parties we went to together and had great fun. I will miss these parties!

Danke Schön Martin!- the trainer of our boxing club at Jukadio Sports center and all the other members: Daniel, Theo, Harald, Tumay, Katarina, Michael, Nick, Fabian, Constantin, Heike, Julia, Naomi for bearing my punching when I was letting my steam off. It is always a pleasure to train, enjoy the sauna, and have a beer with you guys!

I am eternally grateful to my brother and my mom for their unconditional love and support. Finally Virginia: Thank you for your love and kindness. Having you by my side made this journey exciting and enjoyable.

Contents

List of Figures

List of Abbreviations

3d	3-**d**imensional
FM	**F**luorescence **M**icroscopy
BFP	**B**ack **F**ocal **P**lane
w.r.t.	**w**ith **r**espect **t**o
LSFM	**L**ight **S**heet **F**luorescence **M**icroscopy
OPM	**O**blique **P**lane **M**icroscopy
ODO	**O**rthogonal **D**ual **O**bjective
NODO	**N**on **O**rthogonal **D**ual **O**bjective
NOSO	**N**on **O**rthogonal **S**ingle **O**bjective
DM	**D**ichroic **M**irror
NA	**N**umerical **A**perture
FOV	**F**ield **o**f **V**iew
FN	**F**ield **N**umber
PSF	**P**oint **S**pread **F**unction
IIP	**I**ntermediate **I**mage **P**lane
ETL	**E**lectrically **T**unable **L**ens
SCAPE	**S**wept **C**onfocally **A**ligned **P**lanar **E**xcitation
SOPi	**S**canned **O**blique **P**lane **i**llumination
RMS	**R**oot **M**ean **S**quare
fps	frames **p**er **s**econd

Dedicated to my late father and my mother who always encouraged and supported me in pursuing my dreams...

Chapter 1

Introduction

1.1 Motivation

In recent years, *Nematostella vectensis* has become an established cnidarian model for studying the evolution of the nervous system due to its key phylogenetic position [1] and the functional relationships between morphogenesis and behavior [2]. Interest has also been growing to study this model organism due to its extensive regenerative capacity [3]. Nematostella (Figure 1.1(a)) is a sea animal with a life cycle of about 12 weeks in culture. It is easy to spawn and culture in the lab with each female providing tens of eggs after fertilization. Figure 1.1(c) summarizes the development of the Nematostella. The zygote undergoes reductive cleavages to form a blastula which is followed by gastrulation. The planula stage is initiated after the late gastrula, which lasts from 24 to 96 hours post-fertilization. Nematostella starts to undergo elongation at this stage and keeps on developing until it reaches a polyp stage. The morphology of Nematostella is very simple, consisting of two germ layers, endoderm, and ectoderm which are connected by an extracellular matrix that spans the whole body [4].

In toto imaging of biological model organisms like fish [5], fly [6], worm [7] has revolutionized the understanding of animal morphology during their development. Live imaging lets us extract quantitative and qualitative information of biological phenomena most directly. Most of the studies to understand the morphological processes and the nerve net structure of Nematostella using fluorescence imaging techniques have been done after fixing the specimen [1, 2, 8, 9, 10]. So far to my knowledge, there has been no report of Nematostella imaging in 3d and in real-time at organismal scale using any fluorescence microscope. In microscopy, it is a common practice to embed living samples in a gel to immobilize and not cause motion blur. Nematostella can't be immobilized because it goes through contractions regularly (shown in Figure 1.2) which are important for fluid and nutrient uptake

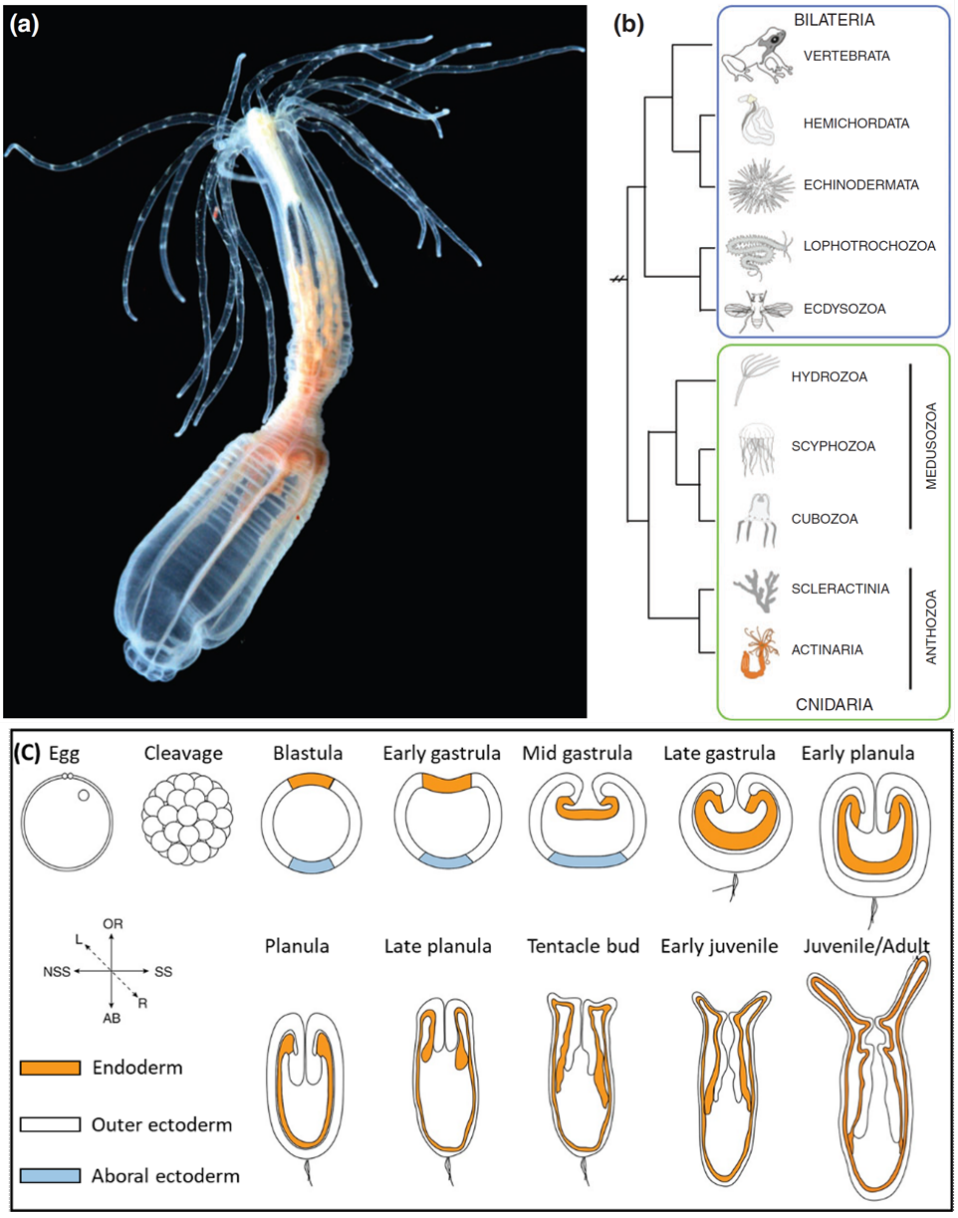

FIGURE 1.1: (a) An image of adult Nematostella. (b) Simplified metazoan phylogeny showing cnidaria, to which Nematostella belongs, as a sister group to bilaterians and its relationship to other major groups. (c) Schematic of developmental stages of Nematostella. Figure modified from Layden *er. al.*[4]

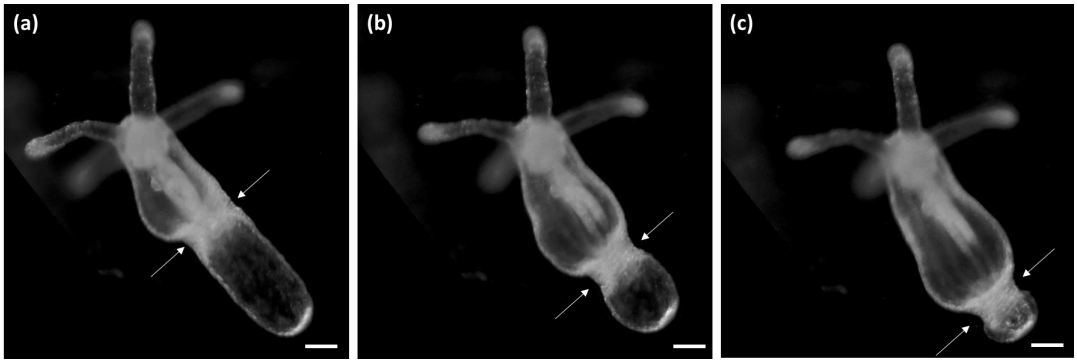

FIGURE 1.2: Nematostella undergoes peristaltic waves regularly during which it contracts perpendicular to the oral-aboral axis and the contraction wave travels from the oral to the aboral end. Through peristaltic waves, it uptakes fluid and nutrients to stay alive and each peristaltic wave lasts for less than a minute. Images were taken on a brightfield microscope. Scale bar: 100 µm [Images from Aissam Ikmi at EMBL]

to stay alive. These contractions are perpendicular to the body (oral-aboral axis), but they travel as a wave from the oral to the aboral end of the Nematostella. These contractions waves are called peristaltic waves and each wave is about one minute long. Unpublished work from Ikmi lab at EMBL shows that embedding nematostella halts its development. It is also highly light-sensitive and an early juvenile can grow up to 1.5 mm with a diameter of around 200 µm. Generally, mesoscopic scales are considered ranging from one millimeter up to a few centimeters, thus the animal dimensions fall in the mesoscopic range. Imaging such a large volume within a few seconds such that we capture multiple volumes while it is going through a contraction is highly challenging. Due to all these factors, *in toto* live fluorescence imaging of Nematostella has not been possible so far. Several important questions, e.g. how animal behavior during muscle hydraulics guides the animal morphology and how neuronal dynamics control muscle movements and body deformations that are necessary for animal development remain unanswered.

To understand these key questions in Nematostella development, the ability to extract quantitative information and to visualize dynamic processes in freely moving live animals at high spatiotemporal resolution *in toto* is highly desirable. An ideal fluorescence microscope would allow us to acquire multicolor images of biological specimens in three dimensions at a maximum attainable resolution. In practice, however, we are limited by various physical and biological factors such as the diffractive nature of light, photosensitivity

of samples, and photostability of fluorescent molecules. To answer a particular biological question at hand, one has to adapt their microscopy technique by optimizing tradeoffs between spatial resolution, temporal resolution, a field of view (FOV), contrast, and phototoxicity to make the imaging process as gentle as possible for the specimen [11]. If one tries to optimize one condition, due to a limited photon budget, we will move away from other conditions. So far, the only solution has been to tune these parameters and tailor a microscope that will target a specific biological application.

1.2 Aim of the thesis

My thesis aims to design and develop a fluorescence microscope capable of performing *in toto* imaging of a freely moving Nematostella at high volumetric imaging speed which will allow us to observe it's natural dynamic behavior and morphological changes, such as contractions.

1.3 Thesis structure

The thesis is organized as follows. **Chapter 2** provides a general introduction to different fluorescence microscopy techniques, especially light-sheet fluorescence microscopy. In subsection 2.5.2 of this chapter, it is explained in detail why we want to build a dual objective oblique plane microscope to image Nematostella. **Chapter 3** describes the optomechanical design optimization and development of the microscope and optomechanical system design. I used Zemax to optimize the optical design and 3d design of the microscope was done using SolidWorks. In **Chapter 4** I discuss the optical performance of the microscope, which is critically defined by the point spread function (PSF) and the light-sheet profile. The PSF was first simulated theoretically and using Zemax and was validated experimentally by imaging beads on the microscope. **Chapter 5** showcases the imaging capabilities of the microscope. Imaging of muscle structure and the nerve net of Nematostella is described in this chapter. In **Chapter 6** I discuss possible directions one can take to expand my work further. **Chapter 7** includes the summary of the thesis and concluding remarks. **Appendix A** lists all the optomechanical components used to build MesoOPM. **Appendix B** gives detailed instructions on how to align and calibrate the system.

Chapter 2

Fluorescence microscopy techniques

Fluorescence microscopy (FM) has become a common tool to study biological processes across scales from processes at the molecular level inside a cell to the development of a specimen at an organismal scale [12]. FM combines the properties of light microscopy like imaging magnified samples at high resolution with the visualization of fluorescence. FM is attractive due to two main reasons. First, isolating the wavelength at which the fluorescent molecules of interest emit from the rest of the spectrum from autofluorescence wavelengths or other fluorescence markers in the case of multicolor imaging provides high contrast. Second, fluorescent dyes or fluorescent proteins provide specificity by binding to specific molecules or by expressing genetically modified fluorescent proteins endogenously at a specific target [13]. FM has not only allowed us to understand various mechanisms of life in different model organisms, but the push to advance this field itself has led to the invention of some of the most powerful FM techniques such as light-sheet microscopy [14] and super-resolution microscopy [15].

2.1 Fluorescence

Fluorescence is a phenomenon where a molecule can be excited and then later emits a photon while transitioning from an excited state to its ground state instantly (*ns* timescale). Molecules that exhibit this phenomenon are called *fluorophores* [16]. The ground state of most fluorophores is a singlet state (S_0) which comprises several closely spaced vibrational states. When a photon of energy E is absorbed by a fluorophore, the quantum state of the molecule will change. If the energy of the photon is low, it will usually transition to higher vibrational states within the singlet state. If the energy of the photon is high enough, the fluorophore might jump to the excited state (S_1). After some

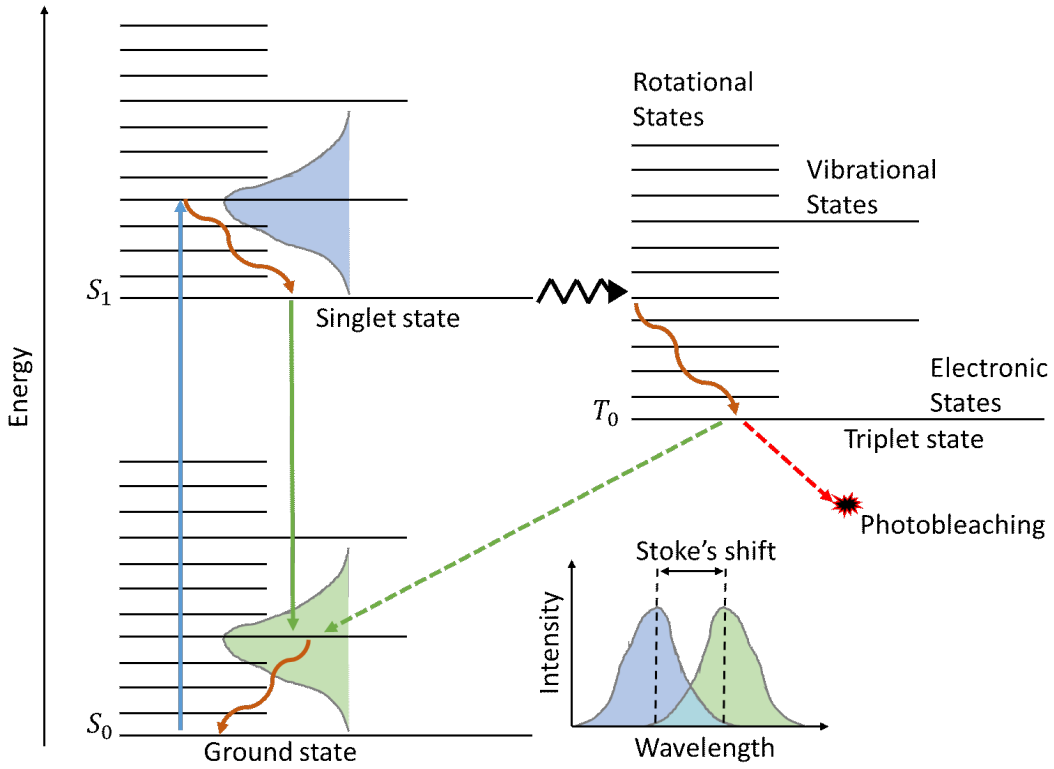

FIGURE 2.1: Jablonski diagram. A fluorophore will jump from the ground state (S_0) to an excited state (S_1) after absorbing a photon. Fluorophores will lose some of the energy in non-radiative heat dissipation and then will return to the ground state again. The difference between the peak intensity of the emission and the absorption spectra is called the Stokes shift. A less probable situation is when the fluorophore transitions from a singlet (S_1) to a triplet state (T_0). From here, the fluorophore can either jump back to the ground state or can react with the reactive oxygen species, leading to photobleaching.

vibrational relaxation in S_1, most probably the molecule will instantly return to its ground state by emitting a photon of lower energy than the absorbed photon. The difference between the emission and the absorption spectra of the molecule is called the Stokes shift and is the foundation of fluorescence imaging as it allows to spectrally separate the desired fluorescence emission from the excitation light [16].

Another less probable transition is when the molecule will make a non-radiative transition to a triplet state (T_0), also called the '*dark state*'. There can be two outcomes after this transition. First, the molecule might emit a photon after spending a long time (μs to s) in T_0 before returning to the ground state. This phenomena is called '*phosphorescence*'. Second, the molecule can react chemically with reactive oxygen species while in a triplet state, permanently damaging the fluorophore. This phenomenon is called '*photobleaching*' and is one of the major concerns in FM [17].

2.2 Widefield fluorescence microscopy

In a widefield fluorescence microscope (Figure 2.2), the fluorescent sample is kept at the working distance of an objective lens. The sample is usually illuminated evenly by a light source by focusing the light at the BFP of the objective lens. The desired illumination wavelength is filtered out using an excitation filter before entering the objective lens. The emitted fluorescence from the sample is then collected by the same objective lens and a dichroic mirror spatially separates the illumination and excitation light. After passing through a tube lens, an image is formed on the camera chip. The objective lens and the tube lens form an infinity space between them and this particular arrangement is called infinity-corrected optics. Such an arrangement allows us to place additional optical components such as dichroic mirrors and emission filters in the infinity space without compromising the image quality.

Magnification of the microscope is determined by the combination of the tube lens and the objective lens is equal to their ratios:

$$M = \frac{f_{TL}}{f_{OBJ}}. \tag{2.1}$$

The field of view (FOV) of a widefield microscope is determined by the total magnification of the microscope, the dimensions of the camera sensor chip

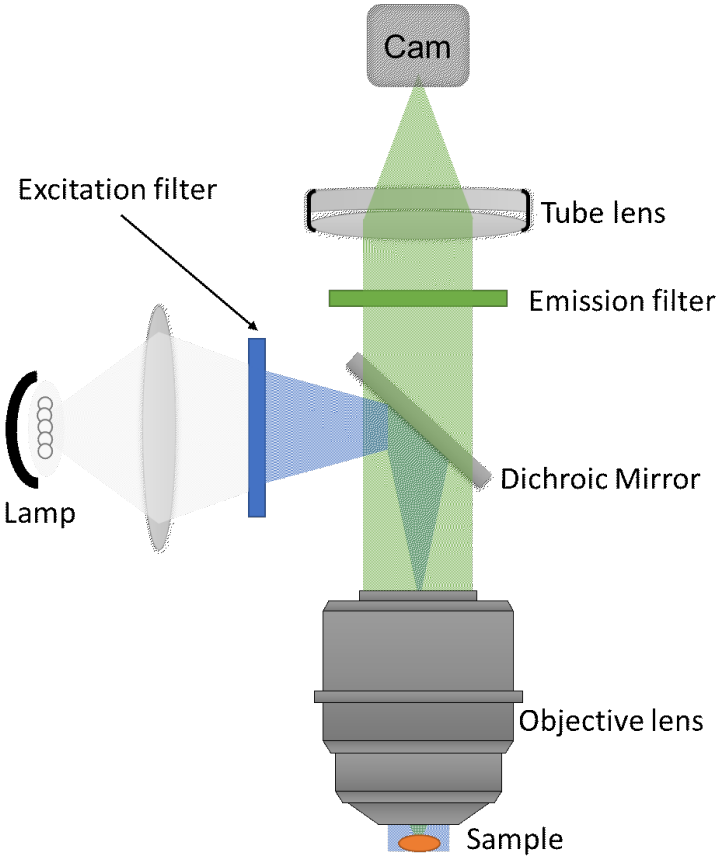

FIGURE 2.2: Schematic of a widefield fluorescence microscope. Light from the mercury lamp is focused at the BFP of the objective creating an even illumination at the sample. The fluorescence is then collected by the objective, which passes through the emission filter and then is focused onto the camera chip by the tube lens.

(D), and the field number FN of an objective stated by the manufacturer:

$$FOV = \frac{\min(D, FN)}{M}. \tag{2.2}$$

Another very important parameter of the objective is the maximum half-angle of the light cone that can enter or exit, α. This angle depends on the aperture and the focal length of the lens. Together with the refractive index (n) of the immersion media of the objective, it defines *numerical aperture* (NA) of the objective:

$$NA = n \cdot \sin \alpha, \tag{2.3}$$

NA determines the light collection efficiency and the maximum resolution of the microscope as shown in the next section.

2.2.1 Resolution of a widefield microscope

The resolution of a microscope is generally defined as the minimum distance at which two point-like objects are still distinguishable. Each fluorophore in a biological sample to be imaged under a fluorescent microscope can be considered as a point-like object. Due to the wave nature of light, when the light emitted by the fluorophore passes through a finite aperture of an objective lens, it will be diffracted. The diffraction pattern corresponding to that aperture for a particular wavelength will be formed at the plane conjugate to the object plane. This diffraction pattern is an image of the point source. As I will mathematically derive below, the image of a point source "spreads out" at the image plane after passing through the optical setup. This system response to a point object is generally termed a *point spread function (PSF)* [18]. The final image of the whole sample will be a linear combination (weights given by the object intensity) of all the PSFs corresponding to each fluorophore.

System response to the electric field originating from the point source or *amplitude* PSF is generally represented by a complex number $h(x,y,z) = |h(x,y,z)|e^{i\phi(xy,z)}$. The phase $\phi(x,y,z)$ corresponds to the oscillations of the electric field in the object and the image. Human eyes and image sensors usually detect the intensity and not directly the amplitude. *Intensity* PSF or an image of a point source through the microscope is given by:

$$H(x,y,z) = h^*(x,y,z) \cdot h(x,y,z) = |h(x,y,z)|^2 \tag{2.4}$$

Final image of the sample will be the convolution of the fluorophore distribution $O(x,y,z)$ in the object space and the detection PSF:

$$I(x,y,z) = O(x,y,z) \otimes H(x,y,z) \tag{2.5}$$

Microscope objectives have a round aperture and its size is determined by the front lens. Let's imagine that there is only one fluorophore in the sample which is being imaged through the optical setup. Fluorophores will emit light isotropically in all directions, but due to the finite aperture, fluorescence emitted at a certain solid angle enters the objective. One can derive the shape of intensity PSF mathematically using Kirchoff's diffraction theory. If the aperture has a radius a lying at a distance f along the z-axis, PSF of such a system will be given by [19]:

$$H(u,v) = C_0 \left| \int_0^1 J_0(v\rho) e^{-i\frac{1}{2}\cdot u\rho^2} \rho d\rho \right|^2 \tag{2.6}$$

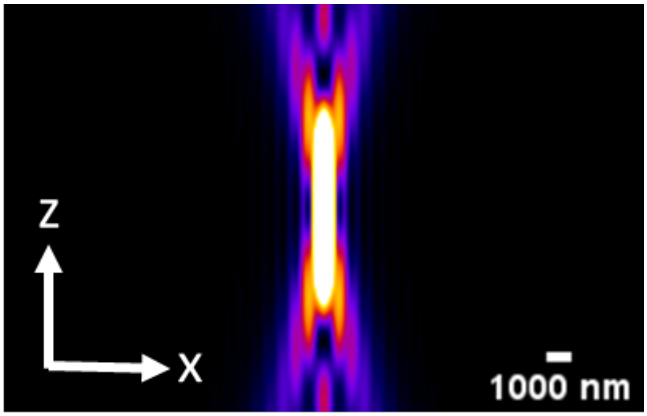

FIGURE 2.3: Axial (XZ) cross section of the PSF of a wide-field microscope. The axial PSF cross-section was simulated using PSF generator on ImageJ for $\lambda = 500nm$ and water immersion ($n = 1.33$) objective lens with NA of 0.5.

where C_0 is a normalization constant, J_0 is the zeroth-order Bessel function of the first kind. $\rho = r/a$ is the normalized distance from the optical axis where $r = \sqrt{x^2 + y^2}$, and u and v are dimensionless variable defined as:

$$v = \frac{2\pi n r}{\lambda_0} \sin\alpha, \quad u = \frac{8\pi n z}{\lambda_0} \sin^2\frac{\alpha}{2} \tag{2.7}$$

Lateral resolution of the microscope can be determined by substituting $u = 0$ in Equation 2.6:

$$H(0, v) = C_0 \left| \int_0^1 J_0(v\rho)\rho d\rho \right|^2 = C_0 \left(2\frac{J_1(v)}{v} \right)^2 \tag{2.8}$$

where J_1 is the first-order Bessel function of the first kind. $H(0, v)$ is a two-dimensional lateral distribution which has a maximum peak at the center and concentric rings of maxima and minima. This distribution is known as the Airy pattern and the cross-section is shown in (Figure 2.5). The smallest resolvable distance is generally defined as the distance between the central maxima and the first local minimum. The first minima lies at $v = 3.38$ and thus the lateral resolution can be calculated by substituting $v = 3.38$ into Equation 2.7 and solving for r:

$$\delta_{xy} = \frac{3.38}{2\pi} \frac{\lambda_0}{n \cdot \sin\alpha} \approx 0.61 \frac{\lambda_0}{NA} \tag{2.9}$$

Analogously, the intensity distribution along the optical axis can be calculated by substituting $v = 0$ into Equation 2.6:

$$H(u,0) = C_0 \left(\frac{\sin \frac{u}{4}}{\frac{u}{4}} \right)^2 \tag{2.10}$$

The first minimum for $H(u,0)$ lies at $u = 4\pi$. The axial resolution in the cartesian coordinate system can be calculated as:

$$\delta_z = \frac{2n\lambda_0}{NA^2} \tag{2.11}$$

An axial cross-section of the PSF of a wide-field microscope using 0.5 AN objective is shown in Figure 2.3. One must remember that lateral and axial resolution formulas were derived using paraxial approximation i.e. $sin\theta = \theta = tan\theta$. However, in section 4.1 of [20], authors discuss that even for higher NA objectives (NA=1.4) paraxial approximation is a good approximation.

2.2.2 Contrast and optical sectioning

The contrast in an object affects the overall resolution in the acquired image. Usually, there is a cut-off to the spatial frequencies that are allowed to transmit through an optical system which is dictated by the resolution limit of the system. Optical systems reduce the contrast of the higher spatial frequencies much more than the lower spatial frequencies. Higher spatial frequencies represent smaller features in the object whereas lower spatial frequencies represent larger features. Thus if the contrast in an image is poor, i.e. the background is higher, smaller features will not be distinguishable from the background. Hence, the resolution is negatively affected and the dynamic range of an image is reduced [21].

In a widefield microscope, contrast is fundamentally poor because the light from out-of-focus planes is also detected on the image sensor which leads to the higher background. The background intensity increases as the thickness of the sample increases. Some microscopy techniques like confocal microscopy and light-sheet microscopy can collect the light originating only from the focal plane. This property to either reject the out-of-focus light or collect light only from a focal plane is called *optical sectioning* [22].

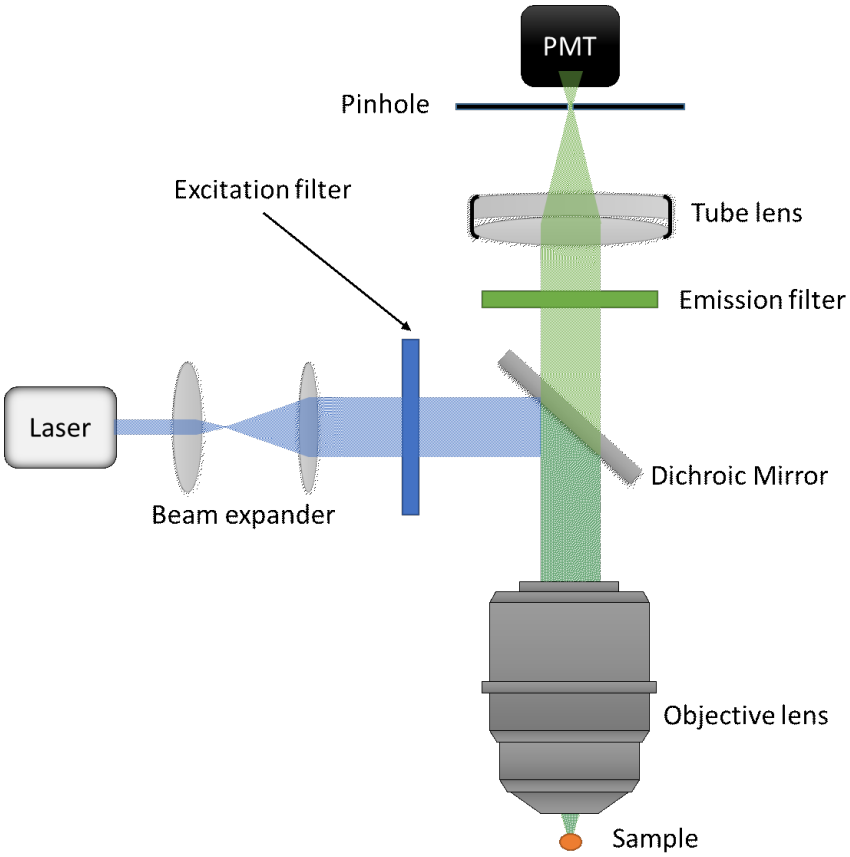

FIGURE 2.4: Schematic of a confocal microscope. The laser beam is first expanded to fill the back aperture of the objective, which will create a diffraction-limited spot at the focal plane. The fluorescence collected by the objective will pass through an emission filter and then be focused onto a pinhole by the tube lens. Light passing through the pinhole will be detected by the photon multiplier tube.

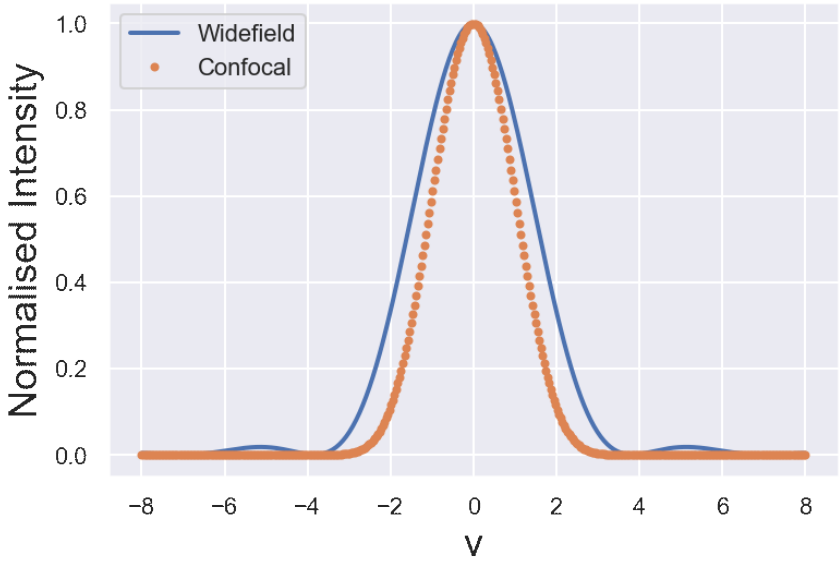

FIGURE 2.5: Comparison of the lateral PSFs (Airy pattern) in a widefield and a confocal microscope. The central peak of the confocal system is sharpened by a factor of ≈ 1.4 and the side lobes are decreased drastically.

2.3 Confocal microscopy

In a confocal microscope Figure 2.4, the objective lens first focuses light into a diffraction-limited spot. Then the fluorescent light from the same spot on the focal plane is collected back by the objective lens, hence the term "confocal". A pinhole is conjugated to the object plane and a point detector such as photomultiplier tube (PMT) is placed behind the pinhole. The pinhole is usually smaller than or equal to the size of the detection PSF. Most of the photons originating from above or below the focal plane will be cut out, significantly increasing the signal-to-noise ratio. The resolution of a confocal microscope can be calculated by convolving the Airy disk of the detection PSF with the pinhole. PSF of a confocal microscope is thus given by the product of excitation and detection PSF [23]:

$$\mathrm{PSF}_{\mathrm{confocal}} = \mathrm{PSF}_{\mathrm{ill}}.\mathrm{PSF}_{\mathrm{det}} \tag{2.12}$$

If the illumination and emission wavelengths lie close to each other, one can simply write the PSF in a confocal microscope as:

$$H(u,v)_{confocal} = C_0^2 \left| \int_0^1 J_0(v\rho) e^{-i\frac{1}{2}\cdot u\rho^2} \rho d\rho \right|^4 \tag{2.13}$$

Lateral and axial resolution for a confocal microscope case be written as:

$$H(0,v)_{confocal} = C_0^2 \left(2\frac{J_1(v)}{v} \right)^4 \tag{2.14}$$

$$H(u,0)_{confocal} = C_0^2 \left(\frac{\sin\frac{u}{4}}{\frac{u}{4}} \right)^4 \tag{2.15}$$

The pinhole in a confocal microscope increases both, lateral as well as axial resolution. Lateral resolution curve i.e. $H(0,v)_{confocal}$ is plotted in Figure 2.5. Comparing it with a widefield microscope, it becomes clear that the central peak is thinner (≈ 1.4 times). Also, the side lobes are decreased and the SNR ratio is improved drastically leading to a better dynamic range of detected signal in images. The axial resolution is also increased slightly in the confocal microscope compared to the widefield microscope.

Even though confocal microscopy increases contrast due to increased SNR, it is a point scanning method. It takes much longer to image a sample compared to a widefield microscope. Another issue is the phototoxicity induced by the confocal microscope [24].

2.4 Light-sheet fluorescence microscopy

Light-sheet fluorescence microscopy (LSFM) is an optical sectioning microscopy technique where a thin 'light-sheet' illuminates a single plane in the sample. Generally, the light-sheet is generated either using a cylindrical lens, called static light-sheet [25], or by scanning light beam at the BFP of the illumination objective, called digitally scanned light-sheet [5]. The fluorescence generated from this plane is then collected by a second objective lens. The detection unit of LSFM is similar to that of a widefield microscope consisting of an objective lens, a tube lens, an emission filter, and a camera. A schematic of an Orthogonal Dual Objective (ODO) microscope is shown in Figure 2.6. 3-D volume is usually acquired by moving the sample stage in a stepwise manner along the detection axis and capturing a sequence of images after each step. Compared to confocal microscopy, LSFM provides various advantages. Because only a thin slice of the sample is illuminated instead of the whole sample, phototoxicity and photobleaching are greatly reduced. Scanning a light-sheet through the sample for volumetric imaging rather than scanning a point makes it much faster.

The concept of light-sheet illumination in microscopy dates back to 1902 when Zsigmondy and Siedentopf used a slit to create light-sheet using sunlight to illuminate the sample from the side. They called it an *ultramicroscope* [26]. They imaged gold nanoparticles diffusing through the light-sheet by recording the scattered light. Zsigmondy was awarded the Nobel prize in 1925 for his studies on colloids using ultramicroscope. This method was then rediscovered by Voie *et al.* in the 1990s where they developed Orthogonal-plane Fluorescent Optical Sectioning (OPFOS) microscope [27]. They used a cylindrical lens to generate a light-sheet and acquired a 3D dataset of a fixed and optically clear guinea pig cochlea which was fluorescently labeled. The light-sheet microscopy gained momentum after Huisken *et al.* developed Selective-Plane Illumination Microscopy (SPIM) in 2004. They used this microscope to image complete embryonic development of a *D. melanogaster* and Medaka fish embryo [25].

LSFM quickly became popular among the developmental biology community because its design can be adapted to image various specimens. Various microscopes have been developed to meet specific environmental conditions and mounting techniques for specimens. Original SPIM had detection and illumination objective lens lying in a plane parallel to the optical table

and the sample (Drosophila and Medaka) was mounted in an upright position in an FEP tube. An inverted LSFM was used to image mouse embryos [28]. An upright LSFM allows us to image a specimen on a coverslip or a Petri dish [29]. Multi-view configurations in which the sample can be illuminated and the fluorescence can be detected from two sides have also been developed to achieve isotropic resolution [6]. LSFM has also been combined with super-resolution techniques like STED [30], SIM [31], SMLM [32], and RESOLFT [33].

2.4.1 Terminology used in the thesis

All the acronyms for different types of light-sheet microscopes can be confusing and thus I want to establish the terminology that I will be using further in this thesis. **Light-Sheet Fluorescence Microscopy (LSFM)** will be used which will include all the light-sheet microscopy techniques collectively. I will follow the terminology used in [34] for different configurations of light-sheet microscopes. **Orthognal Dual Objective (ODO)** will be used when referring to the conventional LSFM where the illumination and the detection objective lie perpendicular to each other. **Non-Orthogonal Dual Objective (NODO)** microscope which has separate illumination and detection objectives but is not orthogonal to each other. Single objective light-sheet microscopes will be referred to as **Non-Orthogonal Single Objective (NOSO)** microscope. In this thesis, **Oblique Plane Microscopy (OPM)** will be used when a fact or a statement is applicable or holds for both NODO and NOSO microscopes in general. The flow chart below summarises the hierarchy of the terminology:

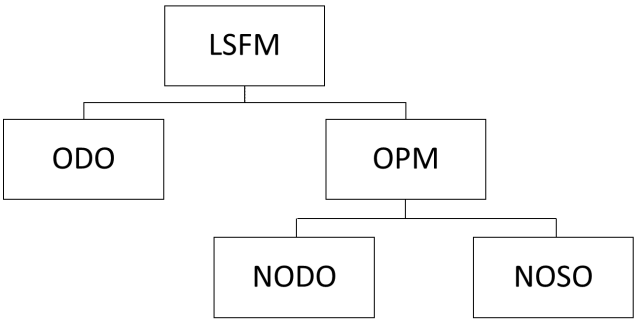

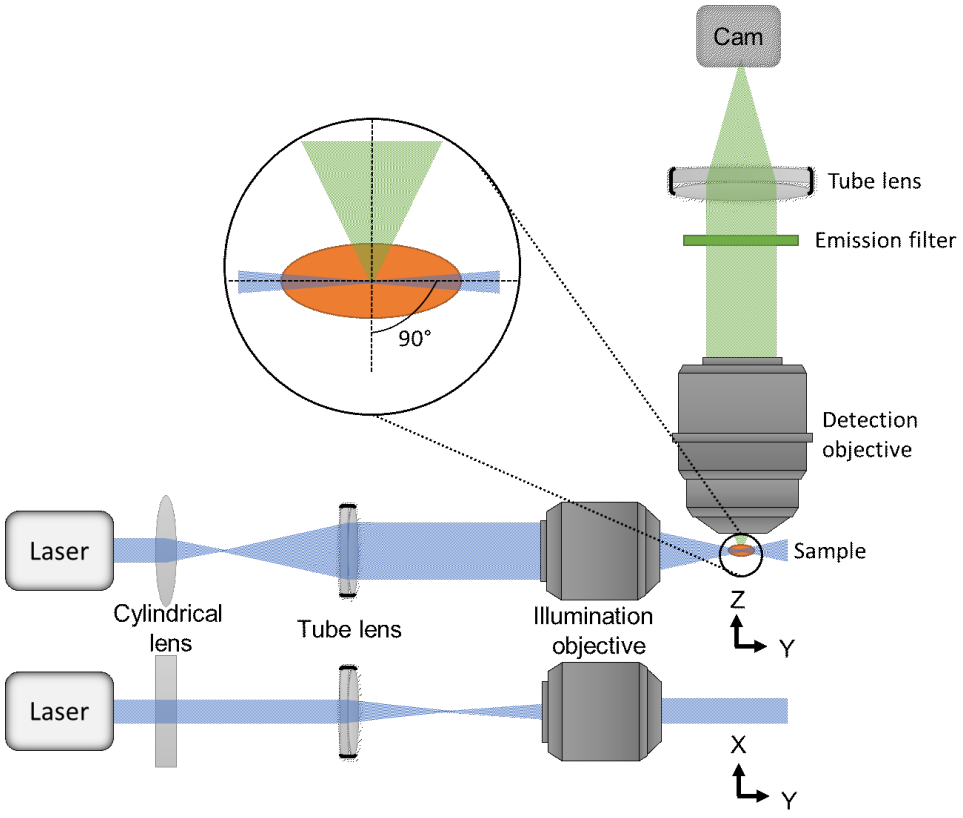

FIGURE 2.6: Schematic of an orthogonal dual objective light-sheet microscope. A light sheet is created using a cylindrical lens which will illuminate a very thin plane of the sample. The illumination is shown from two different views. In the YZ plane, the cylindrical lens will focus the beam and in the XY plane, the cylindrical lens will just act as a glass slab. The detection objective lying perpendicular to the illumination objective will collect the fluorescence and the tube lens will focus the light onto the camera forming an image.

2.4.2 Resolution

The detection arm of a light-sheet microscope is similar to that of any widefield microscope. Illumination being uniform at the focal plane, lateral resolution in a light-sheet microscope is determined by the detection objective lens. Axial resolution depends on the thickness of the light-sheet as well as the axial resolution of the detection objective. Overall PSF of a light-sheet microscope is the product illumination and detection PSF as in the case of confocal microscopy:

$$\mathrm{PSF}_{\mathrm{LSFM}} = \mathrm{PSF}_{\mathrm{ill}}.\mathrm{PSF}_{\mathrm{det}} \tag{2.16}$$

If the waist of the light-sheet is smaller than the axial resolution of the detection objective lens, the overall axial resolution of the microscope will be improved. However, if the thickness of the light-sheet is larger than the axial resolution of the detection objective lens, the axial resolution of the system will be equal to that of the detection objective lens. In any case, due to its optical sectioning properties, contrast is improved significantly. If we image a specimen with 500 µm thickness using 10 µm wide light-sheet, the contrast will be improved 50 times compared with widefield microscopy [24]. And as we discussed in section 2.2.2, improvement, in contrast, will lead to an improved dynamic range of images.

2.4.3 Light-sheet characteristics

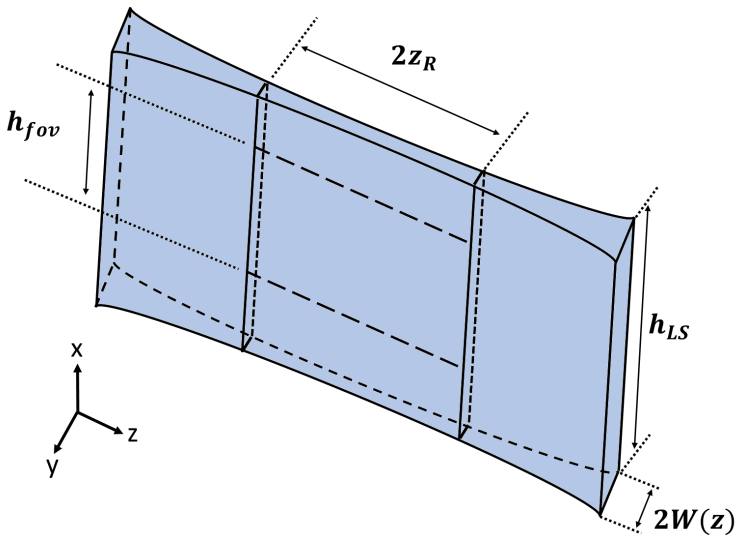

FIGURE 2.7: This figure depicts the light-sheet dimensions which are described in subsection 2.4.3. $\mathbf{h_{fov}}$ is the usable height of the light-sheet upto which the intensity drops by only 20%. $\mathbf{Z_R}$ is the Rayleigh length, $\mathbf{W(z)}$ is the light-sheet waist and $\mathbf{h_{LS}}$ is the total height of the light-sheet.

Light-sheet is usually generated using a laser beam launched from a single-mode fiber. Thus light-sheet characteristics are generally derived using Gaussian beam optics. A specimen can also be illuminated using non-Gaussian beams [35] such as the Bessel-beam, the Airy beam, the double beam, etc., but their discussion is out of the scope of this thesis.

Paraxial Helmholtz equation generally describes the propagation of paraxial waves (waves with nearly parallel k-vector) in space:

$$\nabla_T^2 \psi + i2k\frac{\partial \psi}{\partial z} = 0, \tag{2.17}$$

where $\nabla_T^2 = \frac{\partial^2}{\partial x^2} + \frac{\partial^2}{\partial y^2}$ is a transverse Laplacian operator, $\psi(\vec{r})$ is the complex amplitude of a paraxial wave with an associated wave vector $k = \frac{2\pi}{\lambda}$ and z is the direction of the wave propagation.

After passing through a convex cylindrical lens, the Gaussian beam will converge only along the axis perpendicular to the optical axis of the cylindrical lens and remain unchanged along the other. Thus the beam will now become elliptical and can be described as an elliptical Gaussian beam, which is one of the solutions of Equation 2.17:

$$\psi(x,y,z) = A_0 \cdot \sqrt{\frac{W_{0,x}}{W_x(z)}}\sqrt{\frac{W_{0,y}}{W_y(z)}} \cdot e^{-\frac{x^2}{W_x^2(z)}} \cdot e^{-\frac{y^2}{W_y^2(z)}} \cdot e^{-i\cdot\phi(x,y,z)} \tag{2.18}$$

where A_0 and $\phi(x,y,z)$ represents the amplitude and the phase of the paraxial wave. $W_{0,x}$ and $W_{0,y}$ are the beam waists along two lateral directions. The beam width $W_x(z)$ and $W_y(z)$ are hyperbolic function and can be written independently in orthogonal axes as:

$$W_x(z) = W_{0,x}\sqrt{1 + \left(\frac{z}{z_{\mathrm{R},x}}\right)^2} \quad \text{and} \quad W_y(z) = W_{0,y}\sqrt{1 + \left(\frac{z}{z_{\mathrm{R},y}}\right)^2}. \tag{2.19}$$

For the light-sheet generated in a media with refractive index n, the Rayleigh range along two axes is given by:

$$z_{\mathrm{R},x} = \frac{\pi n W_{0,x}^2}{\lambda}, \quad \text{and} \quad z_{\mathrm{R},y} = \frac{\pi n W_{0,y}^2}{\lambda}. \tag{2.20}$$

Light-sheet parameters can be defined based on Equation 2.20. If the light-sheet is focused along the y-direction, the light-sheet thickness is defined as twice the beam waist $W_y(z)$. The length of the light-sheet is defined as twice the Rayleigh length $z_{R,y}$. Given that the beam profile in the

x-direction is also Gaussian and the intensity drops off quickly towards the edges, only a small portion of the beam in the middle is used for imaging. The height of the light sheet is determined up to where the intensity of the Gaussian beam drops off 20% compared with the intensity in the middle. Thus the height

$$h_{fov} = 2 \cdot 0.472 \cdot W_{0,x} \approx W_{0,x} \tag{2.21}$$

is roughly equal to the beam waist in the x-direction.

From Equation 2.21 it is apparent that the height and the waist of a light-sheet are coupled if one uses a cylindrical lens. To decouple the beam waist and the height of a light-sheet, one can place a galvo scanner at the BFP of the objective and scan it rapidly mimicking a light-sheet (Figure 2.8). The advantage is that the light-sheet will have relatively uniform intensity across the FOV compared with using a cylindrical lens in which case the intensity drops off quickly towards the edges of the FOV.

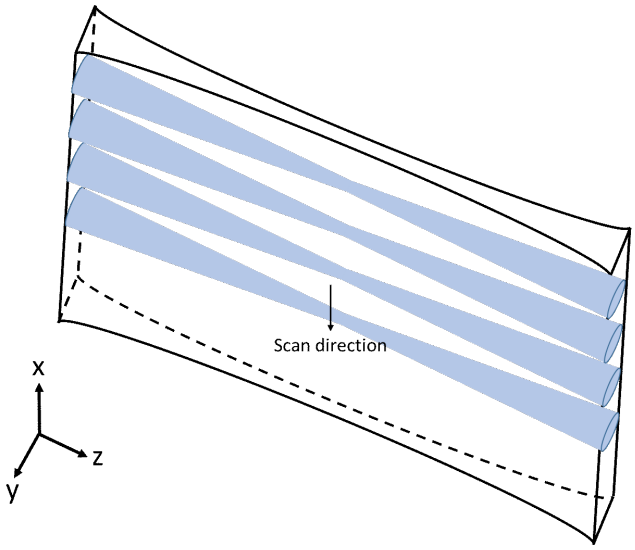

FIGURE 2.8: Digitally scanned light-sheet is generated by rapidly scanning the laser beam over the FOV.

2.5 Oblique plane microscopy (OPM)

Generally, in an ODO microscope, the sample is translated along the detection axis of the microscope to acquire a 3D volume [5]. This dual-objective configuration in which the sample needs to be illuminated from the side and sample stage translation present major limitations in sample mounting and volumetric imaging speed. Although there have been efforts to increase imaging speeds using an electrically tunable lens (ETL) [37] or by

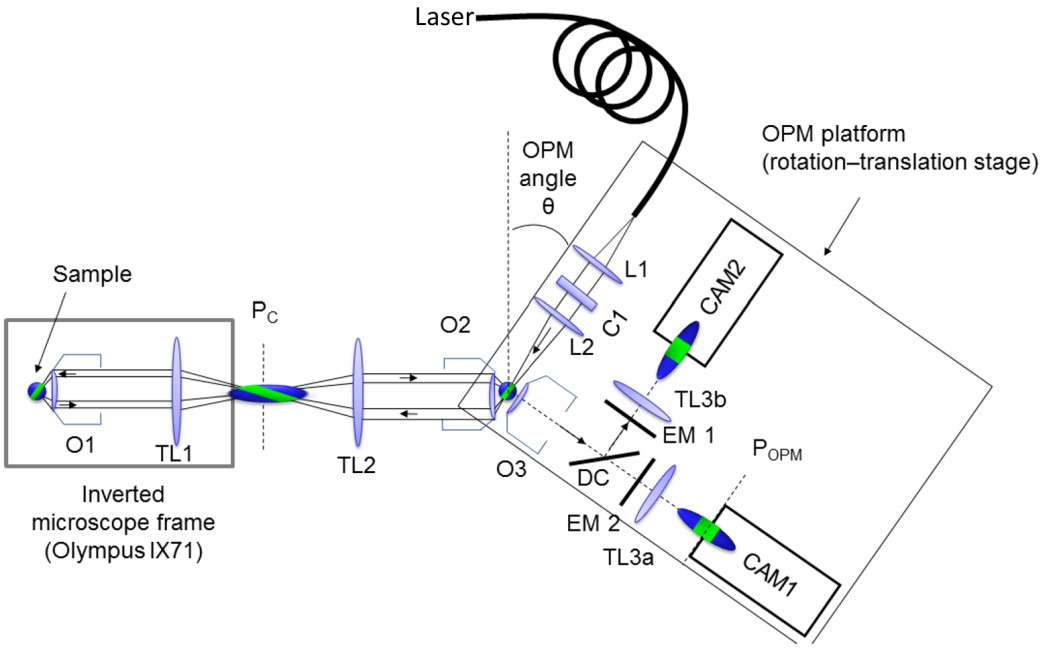

FIGURE 2.9: Schematic of an OPM. The light-sheet is launched through the secondary objective O2 at an angle, leading to the tilted illumination at the sample. The fluorescence is collected by the primary objective O1 and is then relayed at the remote focus of O2. The focal plane of the tertiary objective O3 is made to coincide with the tilted image, which is imaged onto the camera. [Modified from [36]]

rapidly translating the detection objective using a piezoelectric translator [36], volumetric imaging speeds have been limited to 1 Hz over a FOV of less than 1 mm^2. Moreover, imaging freely moving animals is still a challenge in such techniques. Recently developed OPM techniques [38, 39, 40, 41] overcomes the limitation of sample mounting by launching an oblique light-sheet through an objective lens and the same objective lens is then used to collect the fluorescence from the sample. Such a system also offers high speed by eliminating the need for a translation stage and a unique light-sheet scanning and descanning of the detected signal using a single galvo mirror.

C. Dunsby developed the first oblique plane microscopy (OPM) technique [42]. This microscope employed a moving sample stage to acquire volumetric data. Later, the moving stage was eliminated and the illumination beam was coupled into the system through the secondary objective O2 (Figure 2.9) [36]. The light-sheet was launched at an angle that is restricted by the NA of the objective lens. This was achieved by hitting the illumination beam at the edge of the back pupil of the objective lens. Fluorescence from the tilted plane was then captured by the same objective lens (called primary objective O1) and relayed to a remote focus of the secondary objective O2 in an aberration-free

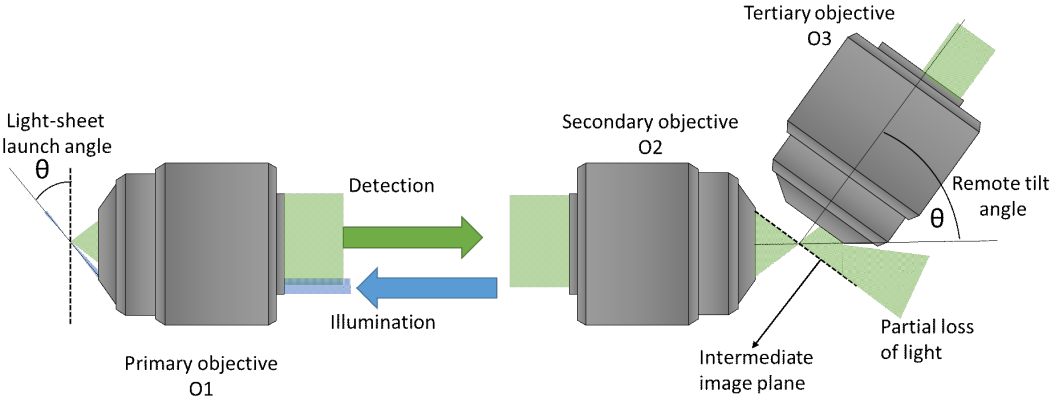

FIGURE 2.10: The OPM angle. The angle at the the light-sheet is launched with respect to the image plane of the primary objective is called the OPM angle. The intermediate image plane of the oblique illuminated plane is formed at the focus of the secondary objective and this process is called 'remote focusing'.

manner. This image was then further relayed onto the camera by a tilted tertiary objective lens O3. Scanning of the light sheet through the sample was achieved by axially scanning O2 using a piezo scanner. The reason for using three objectives to image a tilted illuminated plane has to do with the concept of *remote focusing* which is explained below.

2.5.1 The concept of remote focusing

OPM is based on the concept of remote focusing [42]. The light-sheet is launched at an angle (say θ) w.r.t. the image plane of the primary objective (O1). The fluorescence collected by the primary objective of an oblique plane is relayed at the focus of the secondary objective (O2) to form an intermediate image plane (IIP). The process of relaying the oblique illuminated plane from the focal plane of O1 to the IIP at the focus of O2 is called *remote focusing* and the optical unit from primary to the secondary objective is called *remote focusing unit*. The tertiary objective should be placed such that its image plane overlaps the intermediate image plane. This will happen when the tertiary objective is placed such that its optic axis makes an angle θ with the optic axis of the secondary objective. Thus the light-sheet launch angle and the remote tilt angle are the same as θ and it is termed as *OPM angle*.

To understand the concept of remote focusing and why it is important, we need to understand the concept of *perfect imaging system*. Theoretically, if all the rays from a single point from the 3D object space re-converge to a single point in the image space, such a system is called a perfect imaging

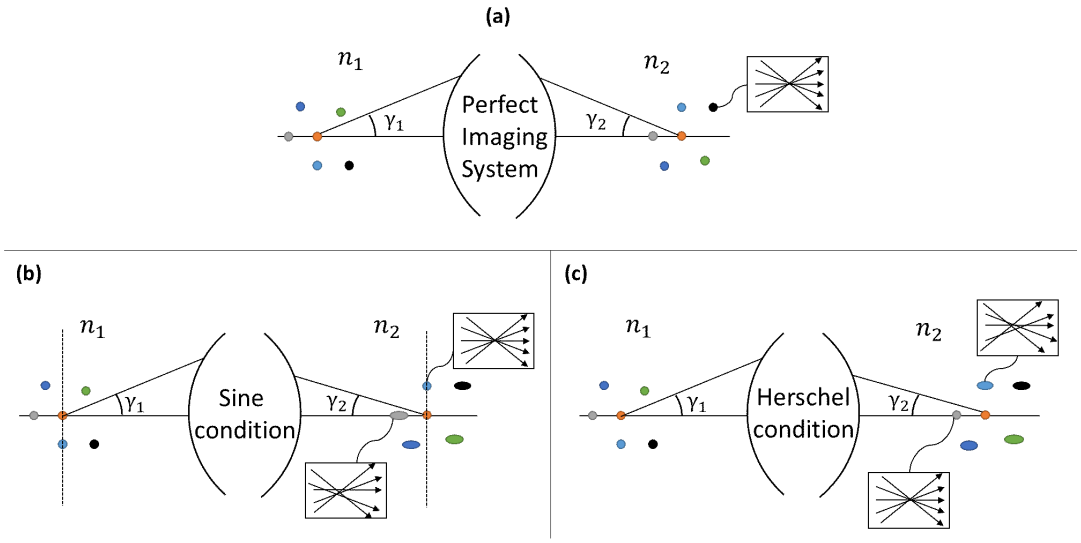

FIGURE 2.11: Sine and Herschel condition. (a) A perfect imaging system images each point in a 3D volume without any aberrations. (b) In an optical system satisfying Sine condition, points lying at the focal plane are imaged aberration-free. (c) In an optical system satisfying Herschel condition, points lying along the optic axis are imaged aberration-free.

system. A schematic of this system is shown in Figure 2.11. It was shown by J.C. Maxwell in 1858 that the system which magnifies the image such that:

$$\mathrm{M} = \frac{\mathrm{n_1}}{\mathrm{n_2}} \tag{2.22}$$

will be a perfect imaging system[43]. One can easily deduce that this condition implies that all the conjugate rays have equal angle w.r.t. the optic axis of the system (Figure 2.11), i.e.

$$\gamma_2 = \pm\gamma_1 \tag{2.23}$$

where γ_1 is the angle a ray makes before entering the imaging system and γ_2 is the angle a ray makes after exiting the imaging system with the optical axis of the the imaging system.

In the case of microscopy, usually, the sample is either imaged in air or liquid media with $1 \leq RI \leq 1.6$. Equation 2.22 puts a constraint on the maximum magnification possible for a microscope to be a perfect imaging system. In practice, almost all microscopes are manufactured to grossly magnify the image of a sample which breaks down the conditions for a perfect imaging system. In such cases, the system can be manufactured to create 'perfect imaging' for a subset of points in 3D object space if it either satisfies the sine condition or Herschel condition. A system in which the rays originating from

the points lying on the focal plane of the system are converged aberration-free satisfies the sine condition. All the objectives we use in microscopy fall under this category. An optical system can be manufactured such that the rays originating from the points lying along the optical axis are re-converged aberration-free. Such a system satisfies Herschel condition. It can be shown that if the lateral magnification of the system is M_l the sine condition imposes the following transformation between the conjugate rays:

$$\sin(\gamma_2) = \frac{n_1}{n_2}\frac{\sin(\gamma_1)}{M_l}. \tag{2.24}$$

For a system satisfying Herschel condition, the conjugate rays follow different transformation:

$$\sin^2(\gamma_2/2) = \frac{n_1}{n_2}\frac{\sin^2(\gamma_1/2)}{M_a}. \tag{2.25}$$

where M_a is the axial magnification of the system. If we create a system such that:

$$M_l = M_a = \frac{n_1}{n_2} \tag{2.26}$$

Equation 2.24 and Equation 2.25 reduces to Equation 2.23. Thus, such a system will be a perfect imaging system [43]. Such a perfect imaging system will 'remotely focus' a 3d volume lying at the sample space aberration-free to the image plane.

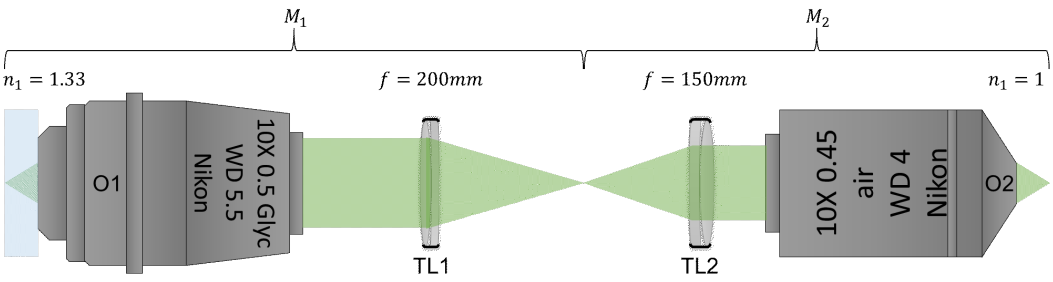

FIGURE 2.12: An example of a perfect imaging system. Each objective lens and corresponding tube lens pair forms a 4f-type system and also both TL1 and TL2 form a 4f-system together. Thus the image planes and the back focal planes of both objectives are conjugated.

Figure 2.12 shows an example of a perfect imaging system. The Objective O1 and the tube lens TL1 form '4f-type' system. Usually, the 4f system refers to the configuration of two lenses with equal focal lengths that are separated by the distance equal to the sum of their focal lengths i.e. 2f. In this thesis, I will refer to a lens configuration with two different focal lengths and are separated by the distance equal to the sum of their focal lengths $f_1 + f_2$ as a

4f-type system. Similarly, tube lenses TL1 and TL2, and the tube lens TL2 and the objective O2 form 4f-type systems, respectively. Thus the image plane and the BFP of the two objectives are conjugated. In this system, $M_1 = 10$ and $M_2 = 7.5$. The total magnification of the system, $M_l = 10.0/7.5 = 1.33$. The ratio of the refractive indices $n_1/n_2 = 1.33$. The axial magnification and the lateral magnification are related in general for a paraxial system as $M_a = (n_2/n_1){M_l}^2$. Putting the values, we get $M_a = 1.33$. Hence, combined lateral and the axial magnification of the system $M_l = M_a = n_1/n_2$, making it a perfect imaging system. Thus a 3d volume at the focus of O1 will be 'remotely focused' at the focus of O2 aberration-free.

2.5.2 Comparision of existing OPM techniques

Recently, various scanning methods have been implemented to perform high-speed scanning in OPM. Swept confocally-aligned planar excitation (SCAPE) microscopy [38] employed a polygon mirror scanner which was conjugated to the BFPs of both primary and secondary objectives. Although 3D volumetric speeds were increased dramatically, the light-sheet tilt varied across the FOV. Shin et. al. introduced a rectangular glass window that can be gradually tilted to perform tilt-invariant light-sheet scanning but introducing such glass window of high refractive index in the detection path lead to spherical aberrations [44]. A tilt-invariant light-sheet scanning method using a galvo mirror was developed by Kumar et. al. [45] and is now a preferred scanning method. This method has been implemented in SOPi microscopy [40] and SCAPE 2.0 [39] to perform high-speed imaging.

Even though using a single objective and implementing tilt-invariant scanning using galvo mirror address several challenges like sample mounting and imaging speed, the resolution and the light-collection efficiency of OPM techniques mentioned above remain low. This is because the tilted tertiary objective is unable to collect all the fluorescence from the secondary objective. Successful efforts have been made to increase the resolution and the light collection efficiency of the system. Yang et. al. [46] developed eSPIM where they used refraction trick by choosing water dipping tertiary objective and aligning the tilted image plane onto a glass coverslip window of the water chamber. The light cone is compressed and refracted towards the tertiary objective, increasing the light collection efficiency and the resolution of the system. In another similar approach of using refraction to increase the efficiency, a glass-tipped objective that is cut at a specific angle to allow the tilted

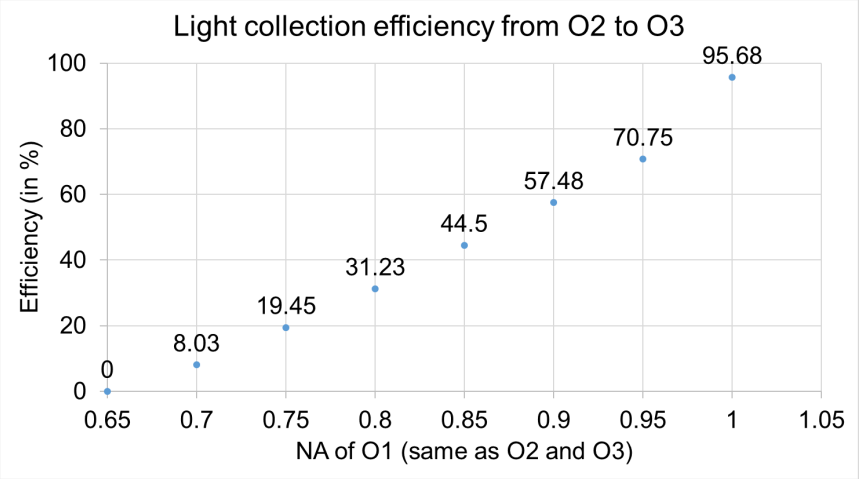

FIGURE 2.13: Dependence of light collection efficiency on the NA of the primary objective in an OPM. At NA=0.65, the collection efficiency drops to zero.[Data obtained after performing simulations using the simulation tool from [34]]

image plane to coincide with the glass surface was developed. The glass surface is also the focal plane of a tertiary objective thus allowing imaging of the tilted image plane onto the camera. A glass-tipped objective is relatively easier to align compared with the water chamber and also offers better resolution compared to eSPIM [47].

Although OPM techniques offer flexible mounting and fast volumetric imaging speed, such techniques have relied on high NA objectives, generally limiting the FOV to 1 mm laterally. This is because higher NA objectives have higher magnification and there exists no 10X objective with NA greater than 0.6. As seen from Figure 2.13, all the light going from O2 to O3 will be lost for an objective with NA below 0.7. Recently developed diffractive OPM technique got around this problem by using diffraction grating to direct light from secondary objective to tertiary objective [48]. By using low NA long working distance objectives they performed volumetric imaging across the lateral FOV of $3\times3\,mm^2$. While they achieved large FOV, the axial resolution of their setup was much worse, around 37 µm. Also, it is practically impossible to use diffraction grating for objectives with NA greater than 0.3 due to geometrical constraints. Another technique that allows oblique plane microscopy at medium or low NA objectives was developed by Glaser *et al.* [34]. They used a separate illumination objective at an angle w.r.t to detection objective. They called this configuration as Non-Orthogonal Dual Objective (NODO) (Figure 2.14) [34]. NODO configuration offers several advantages over Non-Orthogonal single Objective (NOSO) microscopes. First of all, the

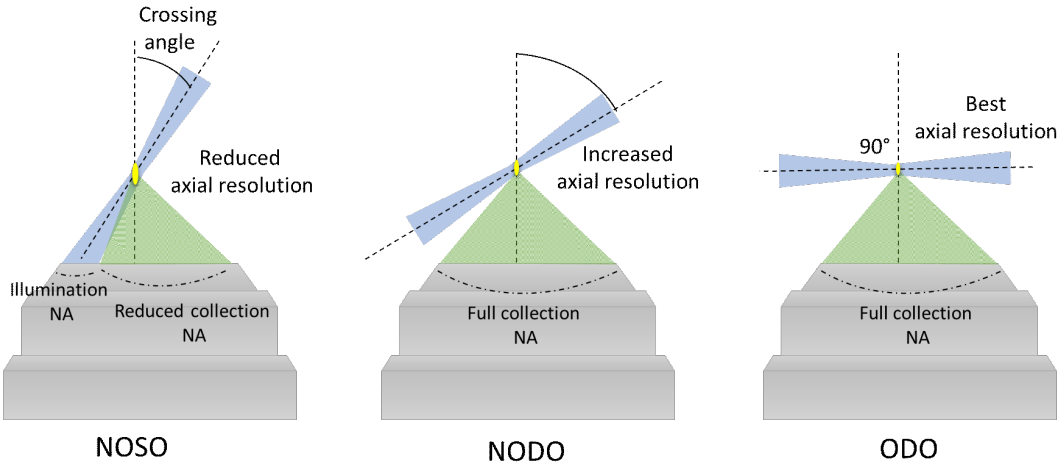

FIGURE 2.14: Comparison of crossing angle and axial resolution between Non-Orthogonal Single Objective (NOSO), Non-Orthogonal Dual Objective NODO, and Orthogonal Dual Objective (ODO) configurations. In the case of NOSO if the NA of an objective is low, the light-sheet thickness is increased leading to decreased axial resolution and optical sectioning. Moreover, the collection NA is also reduced. In the case of NODO, full collection NA is available and the axial resolution and optical sectioning are improved compared to NOSO configuration. ODO configuration offers the best axial resolution and optical sectioning but offers no flexibility in terms of sample mounting.

minimum tilt angle is no more constrained by the NA of the primary objective. For low NA objectives, such constraints lead to lower axial resolution and optical sectioning is reduced. Second, full detection NA is available for collecting the fluorescence. Third, we are flexible in terms of choosing the tilt angle and it can be optimized for desired system parameters like NA of the objectives and axial FOV required. Figure 2.14 compares the effect of crossing angle on the axial resolution and optical sectioning in various configurations. The maximum achievable FOV in their case is about 0.68 mm, and they use the translation stage to image large volumes of cleared tissue which limits the speed of the system. Thus, so far to my knowledge, no OPM has been developed to image lateral FOV greater than 1 mm and axial resolution of less than 10 µm.

Summary of comparison of different OPM techniques				
Technique	Lateral FOV	Axial FOV	Lateral resolution (x,y)	Axial resolution
DOPM [48] (2019)	$3.3 \times 3.0\,mm^2$	1 mm	$2.6 \times 3.1\,\mu m^2$	37 µm
SCAPE 2.0 [39] (2019)	$1 \times 1\,mm^2$	0.2 mm	$1.2 \times 0.6\,\mu m^2$	2 µm
Snouty 2.0 [41] (2020)	$0.75 \times 0.75\,mm^2$	0.3 mm	$0.4 \times 0.4\,\mu m^2$	2 µm
SOPi [40] (2018)	$0.85 \times 0.32\,mm^2$	0.5 mm	$1.3 \times 1.3\,\mu m^2$	unspecified
eSPIM [46] (2019)	$93 \times 93\,\mu m^2$	16 µm	$0.39 \times 0.31\,\mu m^2$	0.6 µm
dOPM [49] (2020)	$0.3 \times 0.3\,mm^2$	0.1 mm	$0.35 \times 0.39\,\mu m^2$	0.81 µm
Aim of the thesis	$2 \times 2\,mm^2$	0.2 mm	$2 \times 2\,\mu m^2$	<10 µm

Chapter 3

Optomechanical design and assembly of MesoOPM

3.1 Microscope design concept

Light-sheet microscopy is a preferred technique to image large (0.5-2mm) specimens due to its optical sectioning properties and high speed. We are interested in imaging Nematostella development and it is crucial to image while the specimen is moving freely. The body of an early juvenile Nematostella can be approximated as a cylinder with a diameter of about 200 µm and length around $1.0-1.5\,mm^2$. Most of the time animal lies on a flat surface with a long axis parallel to the surface and move in 2D on the surface. If we were to use a conventional LSFM, the moment the long axis of the specimen becomes parallel to the light-sheet propagation axis, the light-sheet will have to travel through $1.0-1.5\,mm^2$ tissue (Figure 3.1a). This is also not an open-top configuration which will lead to challenges in mounting Nematostella. Using inverted or upright configurations will also not be possible because the detection plane lies at an angle to the surface on which Nematostella moves. The sample has to be translated using a translation stage which will limit the imaging speed as well as agitate the specimen which might lead to a change in behavior. Moreover, the imaging depth in such configuration is decreased (Figure 3.1b). Imaging in such configuration can be possible if we use an ETL together with the galvo scanning to keep the light-sheet waist parallel to the sample holder surface (Figure 3.6), eliminating the need for a translation stage. However, another galvo and an ETL will be required on the detection arm such that the illumination plane and the detection focal plane overlap at all times. We are interested in imaging over a FOV of 2 mm, which means a 20mm beam at the BFP of the 10X objective. There is no ETL having a diameter more than 16mm and thus such configuration would not be possible. Moreover, ETL is known to cause aberrations especially around

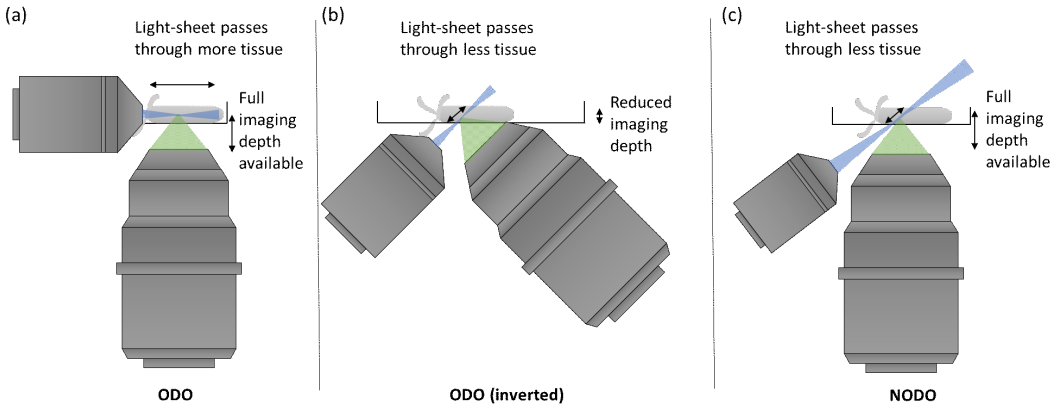

FIGURE 3.1: Orthogonal dual objective vs Non-orthogonal dual objective light-sheet microscope for imaging Nematostella. (a) The conventional ODO design is not ideal due to the distance light-sheet has to travel through the tissue. (b) The inverted configuration is not ideal because it provides less imaging depth as well a moving stage is required to acquire volumetric data. (c) NODO configuration offers increased imaging depth and the light-sheet has to travel shorter through the tissue. Moreover, the requirement of stage scanning is eliminated as is explained in subsection 3.2.3.

the edges, and thus putting it in the detection arm of the microscope with a large FOV is not ideal.

In OPM, the light sheet is launched at an angle that is limited by the NA of the objective. Higher the NA, the smaller the angle of the illumination beam w.r.t. the focal plane of the detection objective. This leads to higher light collection efficiency from secondary to tertiary objective and better resolution. From Figure 2.13 it is clear that the efficiency of light collection decrease drastically once the angle starts to increase. On the other hand, the smaller the angle, the smaller the axial FOV of the microscope (Figure 3.2). Hence, there is a trade-off between the collection efficiency and the axial FOV. Our goal is to image 2 mm lateral FOV which is only possible by choosing an objective with magnification less than or equal to 10X and using a camera with a large image sensor like the Kinetics camera from Photometrics with chip size $20.8 \times 20.8\,\mathrm{mm}^2$. To achieve the best resolution at this FOV, we decided to use the 10X 0.5 NA (Nikon CFI Plan Apochromat 10XC Glyc) multi-immersion objective. The maximum light-sheet launch angle which is possible with this objective is $\approx 26^\circ$, which is limited by the NA of the objective. Thus the tertiary objective will have to be rotated by 74° and all the light transmitted through the secondary objective will be lost as can be seen from the graph Figure 2.13. Thus medium single objective (0.4<NA<0.6) oblique plane microscopes are not possible due to the limitation on the launch angle allowed by the NA of the objective.

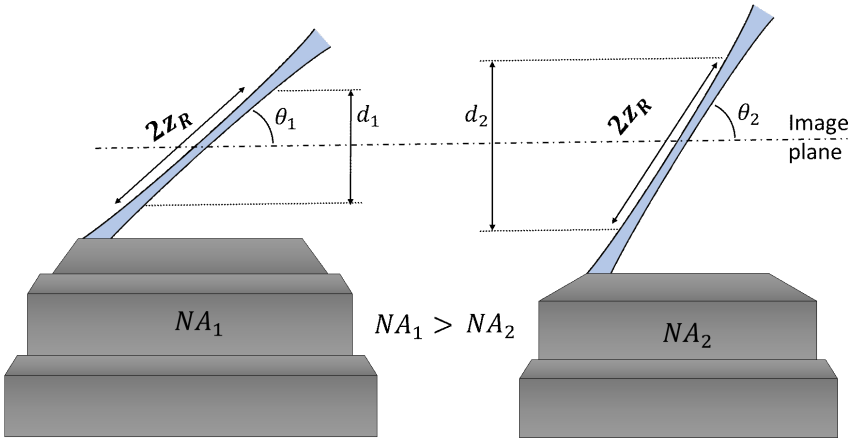

FIGURE 3.2: Trade-off between axial FOV and the light-sheet launch angle in OPM. For larger NA ($NA_1 > NA_2$), the axial FOV decreases ($d_1 < d_2$) and vice-versa, for a light-sheet with same Rayleigh length. For a given Rayleigh length, the axial FOV and the light-sheet launch angle are related as: $d = \sin(\theta) \cdot 2Z_R$

As discussed in section 2.5, the NODO microscope offers various advantages over the NOSO configuration. We decided to build a NODO type microscope. But so far, NODO microscopes have only been built with a sample scanning stage which will limit the imaging speed. Also, the lateral FOV has been limited to mm. To overcome this issue, we introduced an electrically tunable lens (ETL) in the illumination arm of the microscope (explained in detail in subsection 3.2.3) which when precisely synchronized with galvos in the illumination and the detection arm, allows us to image freely moving Nematostella at fast speeds (300 frames per second) over a large FOV (1.5 mm).

3.2 MesoOPM design

For designing the microscope, I first calculated the light-sheet parameters needed to image Nematostella. Keeping these parameters in mind, the microscope was designed which has three main units: the illumination arm, remote focusing arm, and the detection arm. The whole system was designed such that the sample can be loaded onto the microscope easily in an open-top configuration.

3.2.1 Light-sheet design

Light-sheet parameters such as Rayleigh length and the light-sheet height are generally decided based on the sample dimensions. In our case, we are interested in imaging Nematostella from polyp to early juvenile stage. In these

stages, Nematostella has a cylindrical shape with the diameter of the animal reaching up to 200 µm and length between $1.0-1.5\,\mathrm{mm}^2$. The animal needs to move freely, so the chamber size was decided to be 2 mm. From these dimensions, we can derive the light-sheet parameters required to design the microscope.

The light-sheet length usually referred to as twice the Rayleigh length of the light-sheet will be determined by the diameter of the specimen. The light-sheet is launched at 25° and thus the light-sheet length should be

$$\frac{200\,\mu\mathrm{m}}{\sin(25^\circ)} = 472\,\mu\mathrm{m}$$

and thus the Rayleigh length for imaging Nematostella should be:

$$z_R = 236\,\mu\mathrm{m} \tag{3.1}$$

Since the waist of the light-sheet and the Rayleigh length are coupled, the light-sheet waist can be calculated from Equation 2.20:

$$W_{0,x} = \sqrt{\frac{z_R \cdot \lambda}{n\pi}} = 5.2\,\mu\mathrm{m} \tag{3.2}$$

when $\lambda = 488\,\mathrm{nm}$ for GFP excitation. The full width at half maxima (FWHM) is given by:

$$FWHM_{ls} = \sqrt{2 \cdot \ln(2)} \cdot W_0 = 6\,\mu\mathrm{m}. \tag{3.3}$$

The numerical aperture required to generate a light-sheet with these parameters can be calculated as:

$$NA_{ls} = \frac{n \cdot W_0}{z_R} = 0.03 \tag{3.4}$$

The FOV of the microscope is limited by the camera chip size. The magnification of the system is 13.33 and the chip size of the camera (Kinetix from Photometrix) we are using is $20.8 \times 20.8\,\mathrm{mm}^2$. Thus the FOV is 1.56 mm and the height of the light-sheet should be:

$$h_{FOV} \geq 1.5\,\mathrm{mm}. \tag{3.5}$$

3.2.2 Optimum light-sheet launch angle

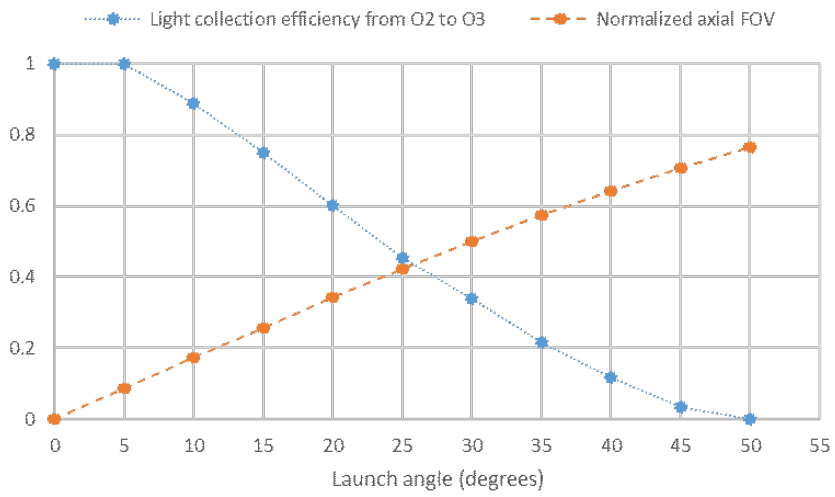

FIGURE 3.3: The light collection efficiency and the normalized axial FOV are plotted as the function of light-sheet launch angle. The curves intersect around 25 degrees which is taken as the light-sheet launch angle for our system.

As discussed previously, the light-sheet launch angle and the axial FOV must trade-off. For our system, we calculated the light collection efficiency at different launch angles using the simulation tool developed by Glaser *et al.* [34]. The explanation of how the efficiency is calculated using the code is described in subsection 4.2.1. The primary objective NA was chosen as 0.5 NA with a refractive index of 1.33. The secondary and tertiary objectives were chosen as 0.45 with a refractive index of 1.0. 0.45 is the maximum NA available for the 10X air objective. The primary objective was chosen to be water dipping to avoid the aberrations while going from the air to the water interface. This is important because Nematostella develops in water. The secondary and tertiary objectives were chosen to be air objectives. This makes it relatively easier to align the system compared to water dipping objectives. In the latter case, a special casing should be constructed and objectives will be mounted at fixed angles, taking away the flexibility.

In the last subsection, I described that the Rayleigh-length (Z_R) of the light-sheet is determined by the dimensions of the specimen. If the light-sheet launch angle is (θ), the axial FOV (d) is given by $d = \sin(\theta) \cdot 2Z_R$ (Figure 3.2). Thus the axial FOV is directly proportional to the $\sin(\theta)$ when Rayleigh length is kept constant. The normalized axial FOV by the factor of $2Z_R$ and the light collection efficiency from secondary to the tertiary objective are plotted as a function of light-sheet launch angle (θ) to find the optimum

tilt angle in Figure 3.3. The two curves intersect around 25 degrees, giving us the optimum light-sheet launch angle. Angle higher than 25 degrees will lead to lower light collection efficiency and an angle smaller than 25 degrees will lead to smaller axial FOV, not enough to span the dimensions of the specimen.

3.2.3 Illumination Unit

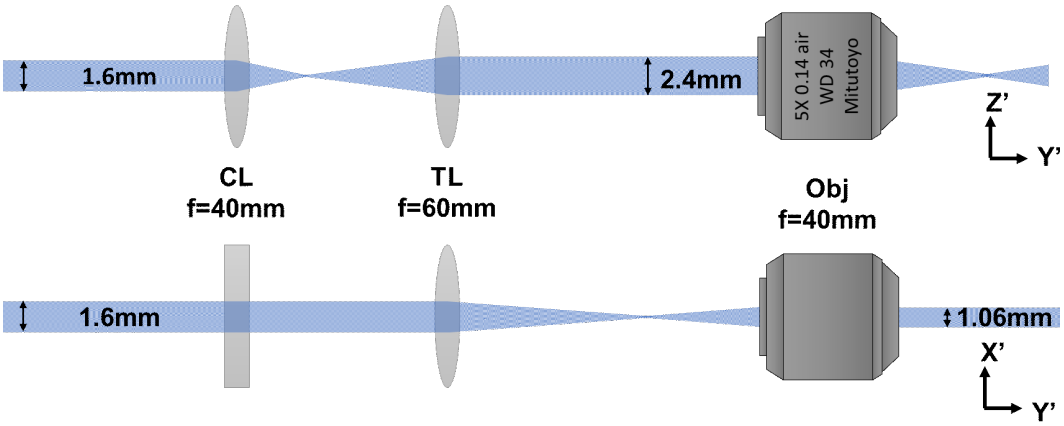

FIGURE 3.4: Optical setup to generate a light-sheet with required parameters. In $Z'Y'$ plane, a 1.6mm beam will be expanded by the factor of 1.5X and will later produce light-sheet with Rayleigh length of 236μm. In XY' plane, a 1.6mm beam size will be demagnified by the factor of 1.5X.

From section 3.1 it becomes clear that the system should offer no steric hindrance while loading the sample. Also, the NA required to produce the light-sheet from Equation 3.4 is 0.03. The illumination objective should have a long working distance as well as NA higher than 0.03. We decided to use a 5X 0.14 NA Mitutoyo objective lens which has a working distance of 34 mm in air. Now we can calculate the beam diameter at the BFP of this objective lens required to produce the light-sheet that fits our requirements. 0.14 NA air objective has BFP diameter $D = 11.2$ mm, from this we can calculate the beam diameter (b) required to produce required Rayleigh length (Equation 3.1):

$$b = D \cdot \frac{NA_{ls}}{NA} = 2.4\,\text{mm} \tag{3.6}$$

A simple scheme to produce light-sheet with parameters calculated is shown in Figure 3.4. A 1.6 µm diameter beam will pass through a cylindrical lens with 40 mm focal length and a tube lens with 60 mm focal length. Then the beam will illuminate the sample after passing through the objective lens. In Y'Z' plane, the cylindrical lens will act as a converging lens, thus the beam

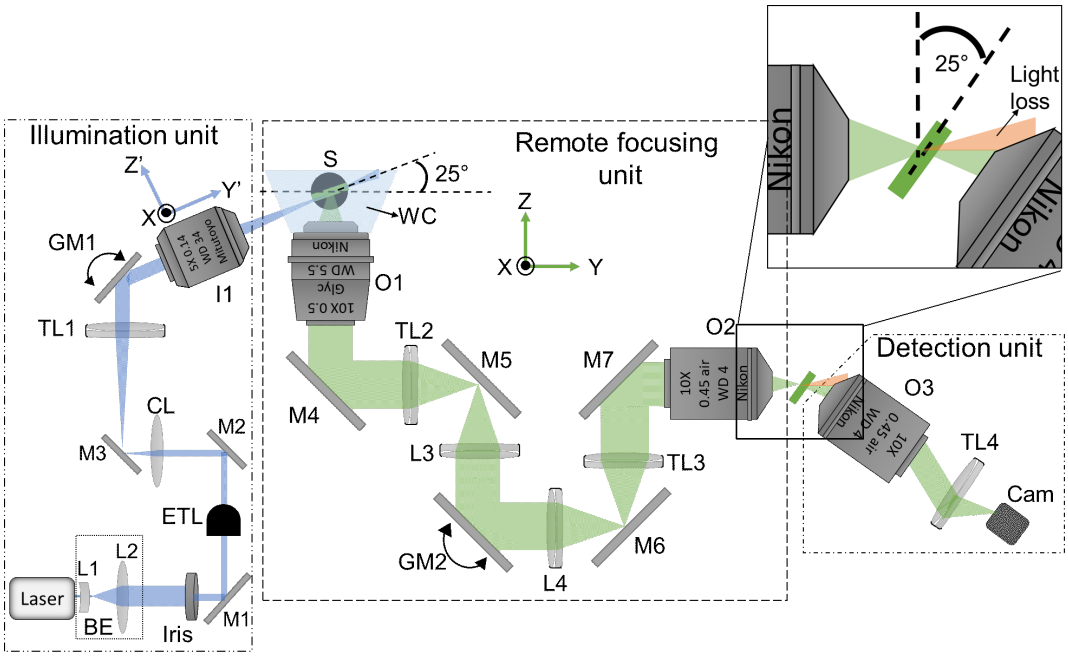

FIGURE 3.5: Optical layout of the microscope. The setup has three main units. The illumination objective (I1) launches the light-sheet into the water chamber (WC) through a glass window that lies perpendicular to the propagation axis of the light-sheet. The detected signal is then collected by the detection objective (O1). The tilted plane is then relayed at the focus of the secondary objective (O2). The image is demagnified by 1.33 times to satisfy the Sine and Herschel condition. The focal plane of the tertiary objective (O3) coincides with the tilted image which is then imaged onto the camera. Some of the light is lost due to the tilt of O3 w.r.t. O2 which is shown in orange.

will expand 1.5X and the diameter at the BFP of the illumination objective lens will be 2.4 mm. This diameter will generate the light-sheet with the required Rayleigh length and waist. One thing that should be noticed from Figure 3.4 is that the height of the light-sheet will not be sufficient to cover the full FOV on the camera. There are two options that we can consider to increase the height of the light-sheet. The first is to get rid of the cylindrical lens and place a galvo at the BFP of the objective which will scan the beam in the X'Y' plane. The light-sheet generated will have relatively uniform intensity over the FOV and depending on the scan range of the galvo, the height of the light-sheet can be adjusted. Another method is to over-expand the beam in such a way that the waist (same as the height of the light-sheet) in the X'Y' plane matches that of the required FOV. Once this is achieved, the remaining beam except for the diameter equivalent to the height of the light-sheet is clipped off. We took the latter method and it is further explained in subsection 4.3.1.

A complete illumination scheme of the microscope is depicted in Figure 3.5. Single-mode fiber coupled to the laser launches a Gaussian beam with a diameter 0.7 mm. This beam is then expanded to the desired diameter with a telescope formed by lenses L1 and L2. Then the beam passes through an Electrically Tunable Lens (ETL) after passing through an iris. The function of an ETL will be explained in the next paragraph in detail. The beam then hits the mirror M3 after passing through the cylindrical lens CL (f= 40 mm). Through the tube lens TL1 (f= 62 mm) and the illumination objective lens I1 (f= 62 mm), Mirror M3 is conjugated to the image plane of I1. The galvo mirror G1 is placed at the BFP of the objective. The BFP lies inside the objective lens, so the galvo is placed at the conjugated plane (formed by two lenses which are not shown in the figure) to the BFP of the objective. Rotating M3 will rotate the light-sheet about its mid-point and rotating GM1 or M2 will translate the light-sheet across the image plane of I1, thus providing us the necessary degrees of freedom to align the light sheet.

Function of the Electrically Tunable Lens (ETL)

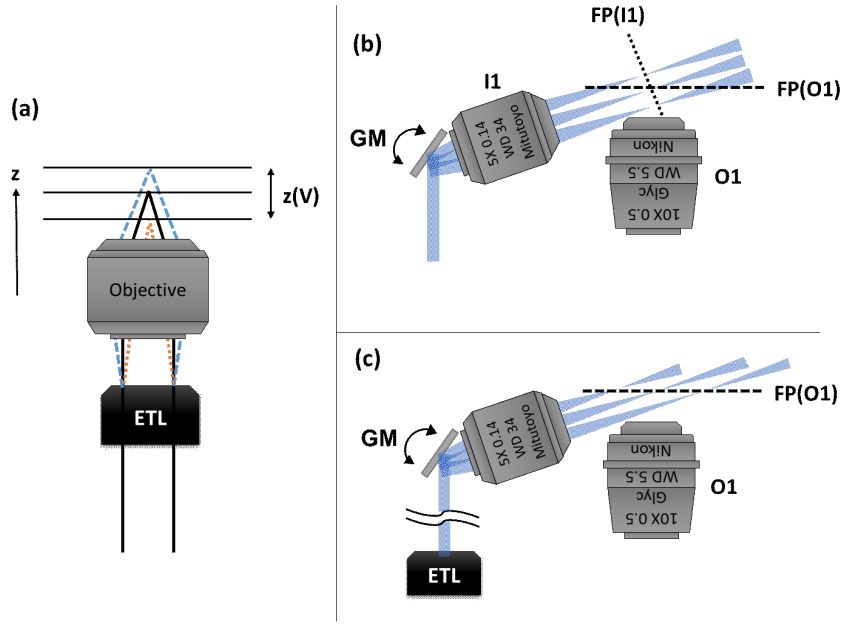

FIGURE 3.6: Function of an ETL. (a) The focus of a lens can be shifted axially using an ETL and the z-position of the focus is a function of the voltage applied. (b) Without an ETL in the setup, the light-sheet waist will not coincide with the focal plane (FP) of O1 while scanning with the galvo lying at the BFP of O1. (c) The light-sheet waist coincides with the focal plane of O1 using an ETL.

An ETL is a liquid lens that can change its curvature on the application of voltage, allowing dynamic tuning of the focal length as shown in Figure 3.6(a) [50]. The illumination objective lens is tilted by 25 degrees w.r.t. the focal plane of the detection objective lens in the microscope setup. This means that while scanning the light-sheet over the sample using the galvo mirror, the focus of the light-sheet and the focal plane of the objective lens O1 will not coincide (Figure 3.6(b)). When synchronized with galvo precisely, the ETL will shift the focus of the light sheet such that when the galvo will scan the light-sheet, the waist will always coincide with the focal plane of detection objective (Figure 3.6(c)).

3.2.4 Remote focusing unit

Ideally, the remote focusing unit recreates aberration-free 3D volume of the sample as far as Sine and Herschel conditions are satisfied as explained in subsection 2.5.1. Primary objective O1 (Nikon glyc 10X 0.5NA W.D.) collects fluorescence from the sample which is then focused using a tube lens TL2

(f=200 mm) to form an image at the mirror M5. Mirrors M5 and M6 are conjugated using L3 (f=200 mm) and L4 (f=200 mm) which forms 1:1 relay. The tube lens TL3 and the objective lens O2 (Nikon 10X 0.45 NA air) form a remote image of the sample with the same dimensions. This remote focusing unit satisfies Sine and Herschel condition as shown in Figure 2.12. The image plane at O2 is tilted and is called the intermediate image plane which is then re-imaged onto the camera using a detection unit. The tube lens TL3 has an effective focal length of 150 mm and is made with a combination of three lenses with focal lengths 200 mm, 750 mm, and 750 mm as shown in Figure 3.7. A tube lens with a focal length of 150 mm is not commercially available, so I had to design it myself. Further explanation on why this lens assembly is designed can be found in the next section.

FIGURE 3.7: TL3 tube lens assembly. Two identical ACT508-750-A-ML achromats from Thorlabs with focal lengths 750 mm each are separated by a 7.5 mm spacer. Then TTL200MP tube lens from Thorlabs is attached to the assembly with a 12.7 mm spacer. The effective focal length of the combination is 150mm.

3.2.5 Detection unit

The detection unit consists of an objective O3 (Nikon 10X 0.45 NA air), a tube lens TL4 (f=200mm), and a camera. The optic axis of objective O3 is placed at an angle of 25 degrees to the optic axis of the objective O2 as shown in Figure 3.5. Such an arrangement makes sure that the remote image of the tilted plane illuminated at the sample and focal plane of O3 coincides. The tube lens, the camera, and the objective O3, all are mounted on a separate breadboard which can be rotated and translated. Part of the light cone coming from O2 will not be collected by O3 due to the tilt and the remaining cone passing through the objective and the tube lens will form an image on the camera chip.

3.3 Optical design optimization using Zemax

Before designing any optical instrument like a microscope, evaluating its overall performance through simulations is desirable. The optical design of the microscope is optimized using Zemax. The most critical part of the system is the remote focusing unit. I simulated the remote focusing arm of the microscope using Zemax and I will be discussing some of the key design optimization processes to achieve optimum performance. In subsection 2.5.1 I discussed that the overall performance of any oblique plane microscope depends on the performance of the remote focusing optics. If the system satisfies Sine and Herschel conditions, the system will introduce minimum aberrations. I used root-mean-square (RMS) wavefront error to quantify the aberrations in the simulated systems. The wavefront converging at the image plane of the system can be aberrated and thus different from the ideal spherical wavefront (Figure 3.8). In Zemax, the wavefront of the system is compared against the ideal spherical wavefront on any particular image point. RMS wavefront error is given by a square root of the difference between the average of squared wavefront deviations minus the square of average wavefront deviation. Hence, it represents the statistical deviation from the ideal wavefront, averaged over the entire wavefront.

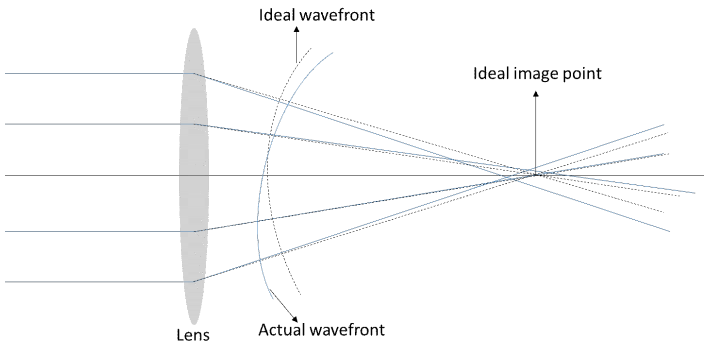

FIGURE 3.8: After passing through a lens, the wavefront is may be aberrated and is different from an ideal wavefront. RMS wavefront error is calculated by comparing the actual wavefront to the ideal wavefront.

3.3.1 Choosing the right tube lens

The design optimization of the system starts with choosing the right tube lens to combine with objective lenses. Generally speaking, the space between the objective and the tube lens is called the *infinity space*. The infinity space (d) between the objective and the tube lens is used to place optical elements like a dichroic mirror for aberration-free imaging, but is not a 'true infinity space'.

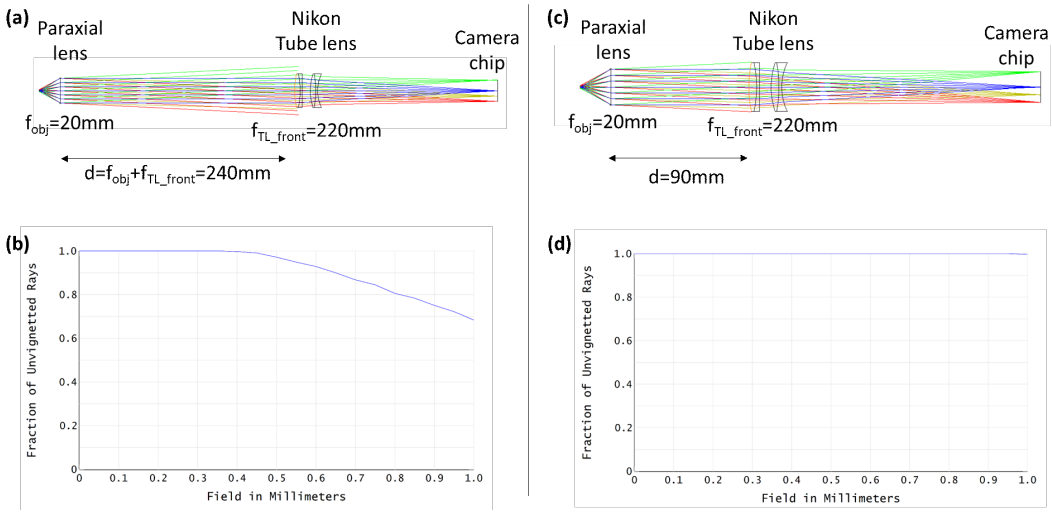

FIGURE 3.9: Nikon tube lens vignetting. (a) If the paraxial lens and the Nikon tube lens form a 4f-type system, vignetting occurs. (b) The vignetting is quantified across the 2mm FOV and the graph shows rays from the middle to the edge of the FOV. (c) The maximum distance between the paraxial lens and the tube lens should be 90mm for vignetting not to occur. (d) The graph clearly shows that in this case, the rays pass without vignetting across the FOV.

There is a limit to the maximum distance between the objective and the tube lens after which the vignetting starts to happen. The reason is that the rays originating from points lying away from the center of the FOV will exit the objective pupil at an angle. Any ray passing through the center of the lens passes without refraction and let us call this a 'central ray'. After exiting the pupil, the 'central ray' originating from any point source lying off-axis on the image plane will not be parallel to the optical axis of the objective and will make some angle which will depend on the height of the point in the sample plane from the center and the focal length of the lens. All the other rays originating from that point source will travel parallel the the 'central ray' after exiting the pupil. For points lying at the edge of the FOV, the angle at which rays exit the pupil will be large and the tube lens with a finite aperture at some distance will barely capture these rays. The tube lens should not be placed further than this distance.

In designing a remote focusing unit, we don't have the luxury to choose the distance between the objective and the tube lens. The BFP of the primary objective and the secondary objective are both conjugated, thus the objective and the tube lens have to be placed in a 4f-type configuration (see Figure 2.12). If the maximum distance where the vignetting starts are smaller than the sum of the back focal length of the objective and front focal length of the tube lens, the vignetting will occur. The situation is clarified in the

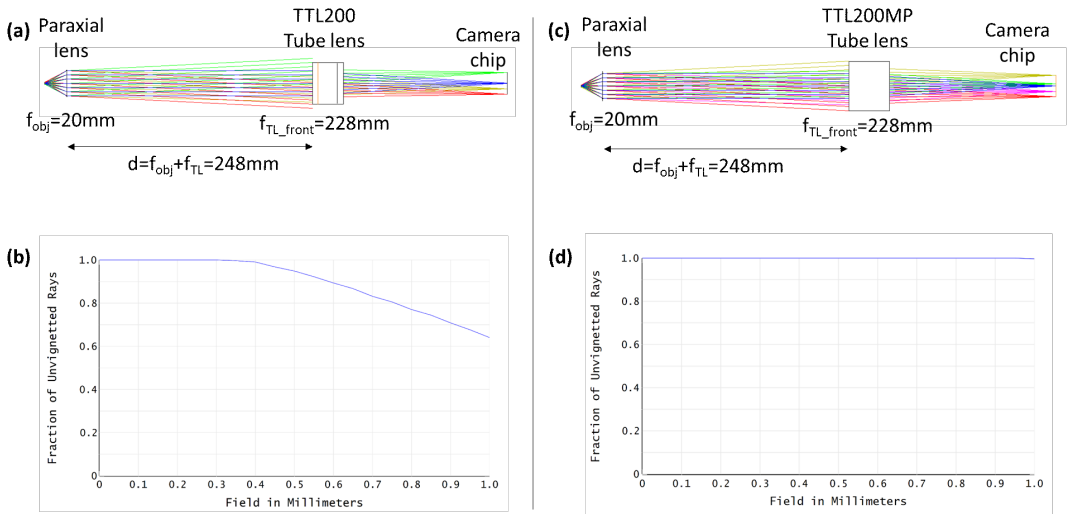

FIGURE 3.10: Thorlabs tube lens vignetting. (a) When the paraxial lens and the TTL200 forms a 4f-type system, vignetting occurs. (b) The vignetting is quantified across the 2 mm FOV and at the edge of the FOV, more than 35% rays are vignetted. (c) For TTL200MP, the vignetting doesn't occur in the 4f-type system with the paraxial lens. (d) The graph shows that the rays pass without vignetting across the FOV.

example below using a tube lens (f=200 mm) from Nikon which is combined with a paraxial lens ($f_{obj} = 20$mm). The paraxial lens has an NA of 0.5 and can be considered as an ideal case for a 10X 0.5 NA objective. The front focal length f_{TL_front} of this tube lens is 220 mm. From the Figure 3.9(a) we can see that some rays are clipped (also called vignetting). Figure 3.9(b) shows that the vignetting starts around 0.4 mm at the sample space in front of the objective. The total FOV defined here is 2 mm (± 1 from the center) and thus at the edge of the FOV, more than 30% rays are vignetted. The distance where the vignetting just starts to happen is 90 mm between the objective and the tube lens as shown in Figure 3.9(c). Figure 3.9(d) shows that 100% rays at the edge of the FOV pass unvignetted.

I modeled various commercially available tube lenses in combination with the paraxial lens (f=20mm) across the FOV of 2 mm to check for vignetting. Out of all commercially available tube lenses modeled, only TTL200-MP was found to have an aperture large enough to not cause vignetting. Another example of tube lenses from Thorlabs TTL200 and TTL200MP are compared in Figure 3.10. One can see that if the TTL200 is placed in a 4f-type configuration with the paraxial lens, the vignetting occurs, which is not the case for TTL200MP.

As mentioned in the previous chapter, to satisfy the Sine and Herschel conditions in the remote focusing unit, the tube lens used together with the

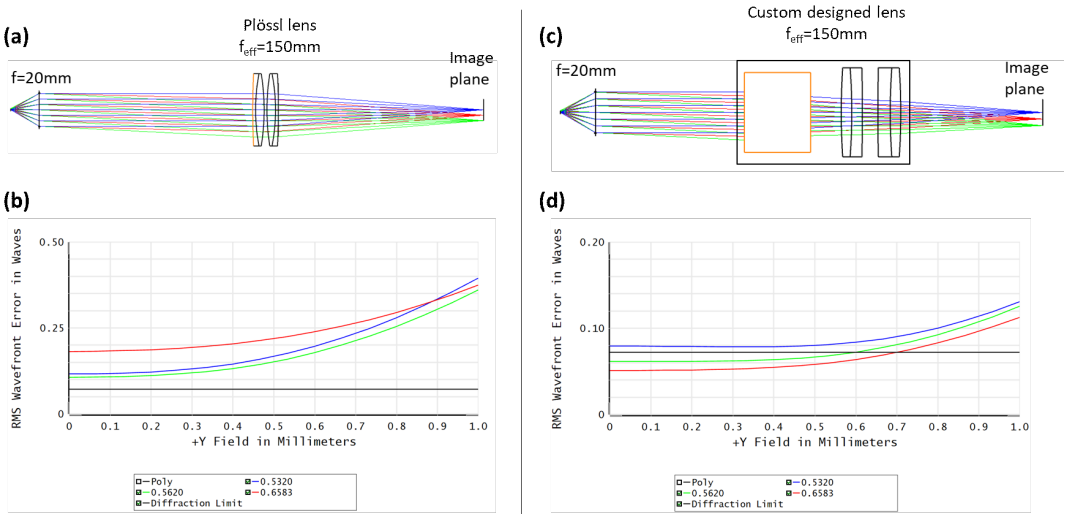

FIGURE 3.11: Comparing the custom-made tube lens with Plössl lens. (a) The object plane is conjugated to the image plane by the paraxial lens (f=20 mm) and the Plössl lens (f=150 mm) in the zemax model. (b) The aberrations are quantified and are expressed on the graph as RMS wavefront error at each field (point) on the image plane. The aberrations are prominent at the edge of the FOV. (c) The Plössl lens is replaced by the custom-designed tube lens with an effective focal length of 150mm. (d) The graph shows that the aberrations remain closer to the diffraction limit and are well below a quarter of the wavelength.

secondary objective should have a focal length of 150 mm. There is no commercial tube lens available for this focal length. It is common practice in microscopy to use Plössl type lens in which two achromatic lenses of higher focal length are combined to form a single lens of lower focal length. This method lowers the aberrations introduced especially around the edges of the lens. I first simulated the combination of two lenses with the focal length of 300mm each such that the effective focal length is 150mm. Figure 3.11(a) shows the Zemax model where the Plössl type lens is used as a tube lens. From Figure 3.11(b) it can be seen that the wavefront error increases exponentially closer to the edge of the FOV, reaching well above a quarter of the wavelength.

Higher the focal length of a lens, lesser will be the spherical aberrations at the focal point, which is due to the lower curvature of the refracting surface of a lens. With this in mind, I custom-designed the tube lens by combining two 750mm achromats with a TTL200MP lens from Thorlabs. TTL200MP is a telecentric lens that is also optimized for diffraction-limited imaging over its full aperture. The design optimization is done in Zemax by sending parallel rays through a paraxial lens of focal length 150 mm. The three lenses that are to be optimized are placed after the paraxial lens. Then the distance between the lenses is adjusted until the rays come out almost parallel and the beam

diameter exiting the system should be the same as the beam entering the system. Finally, using the *Optimization Wizard* in Zemax, the wavefront is optimized iteratively until the best merit function is achieved in the simulation. At this point, the rays will be perfectly parallel. The simulation was done using the tube lens I designed as shown in Figure 3.11(c). One can appreciate that the wavefront error remains close to the diffraction limit and remains well below the quarter of the wavelength. Thus the custom-designed tube lens which will be used in the system has superior optical performance compared with the Plössl lens.

3.3.2 Modeling remote focusing unit

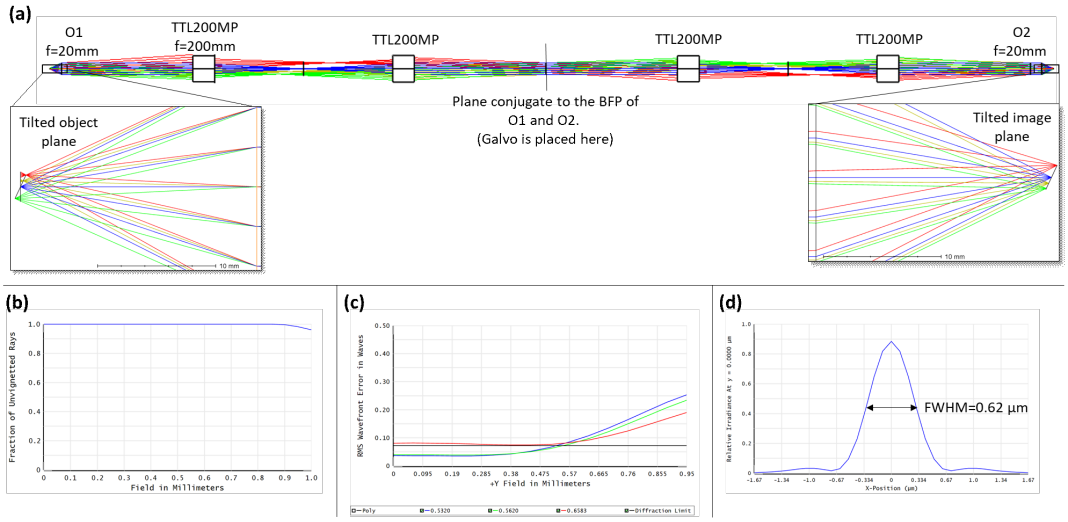

FIGURE 3.12: Modelling the remote focusing unit using TTL200MP tube lens. (a) The remote focusing arm was modeled with a tilted object plane using TTL200MP lenses. (b) The overall vignetting of the remote arm was checked and remains less than 5% at the edges. (c) The RMS vs field graph shows that at the edges of the FOV, the aberrations increase. (d) The Huygens PSF cross-section is plotted at the image plane.

Zemax model of the objective lenses that I am using in the system is not available, thus I am using a 20 mm paraxial lens with 0.5 NA in the modeling. The primary objective in the system is 10X 0.5 NA and the secondary and the tertiary objective are both 10X 0.45 NA. One very important point to note here is that because ZEMAX models of commercial objective lenses are typically not available, I modeled two different scenarios of the remote focusing unit. In the first scenario (Figure 3.12), I used the TTL200MP from Thorlabs as tube lenses and the 1:1 relay. I used Zemax black boxes that can be downloaded from Thorlabs. Two TTL200MP lenses conjugate the BFP of O1 to the galvo

as indicated in Figure 3.12 and the other two conjugate the BFP of O2 to the galvo. Thus both BFPs of O1 and O2 are conjugated to each other. In the second scenario (Figure 3.13), the tube lens behind the primary lens was replaced by an ideal lens of focal length 150 mm, and the tube lens used with the secondary objective lens was replaced by a custom-designed tube lens from Thorlabs lenses which has an effective focal length of 150 mm. This was to check the performance of the custom-designed tube lens in the remote focusing unit.

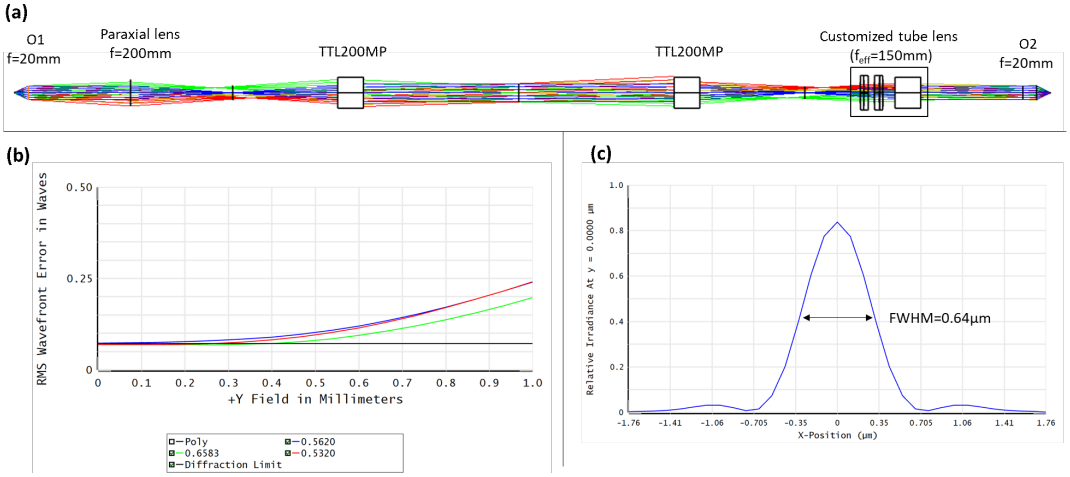

FIGURE 3.13: Modelling the remote focusing unit using custom-designed tube lens. (a) The remote focusing arm was modeled with a tilted object plane and using a custom-designed tube lens with an effective focal length of 150 mm. (b) The aberrations are quantified and the performance remains similar to the commercially available TTL200MP tube lens. (c) The FWHM of the lateral PSF also remains similar to Figure 3.12(d) at the image plane.

3.3.3 SolidWorks model of the microscope

Once the microscope is designed 'on paper', a 3d model is constructed in SolidWorks. There are several advantages of making a 3d model of the microscope. 3d model helps us realistically visualize what the microscope will look like once constructed. This provides us with an accurate representation of the physical dimensions of the optomechanical components and their distance from other components. We can avoid costly mistakes as it gives us the possibility to modify or edit instantly in case of potential design issues. The 3d-model of the microscope is shown in Figure 3.14. The design of the illumination arm is shown separately in Figure 3.15.

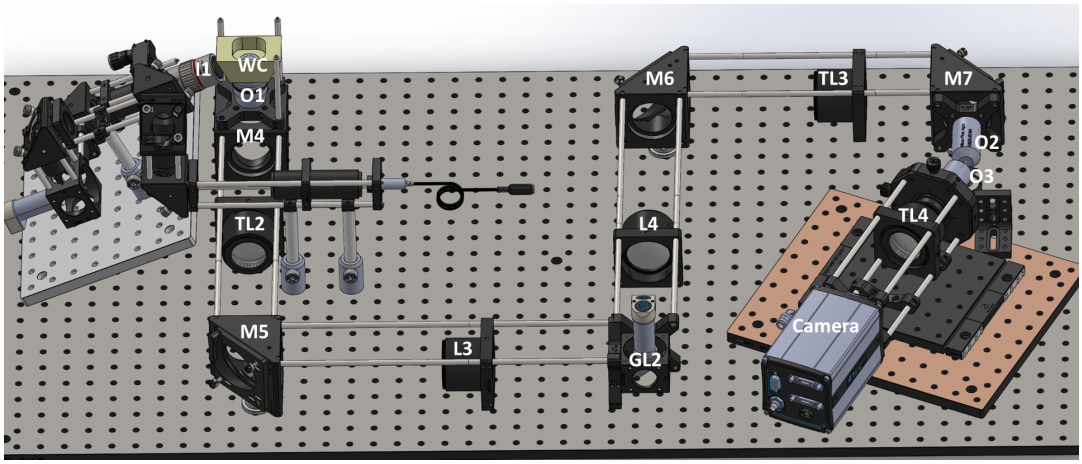

FIGURE 3.14: 3D model of the microscope designed on SolidWorks.

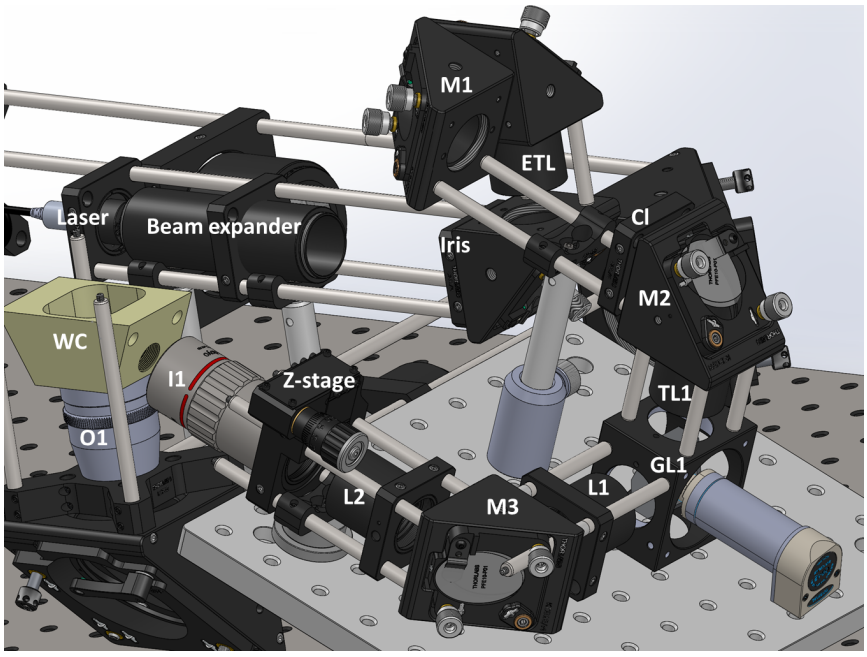

FIGURE 3.15: 3d design of the Illumination arm of the microscope.

3.4 Microscope assembly and alignment

After the 3d model is built the microscope is assembled in the lab on the optical table. Figure 3.16 shows the assembled microscope in the lab and in this section, we will discuss the assembly and alignment of the microscope.

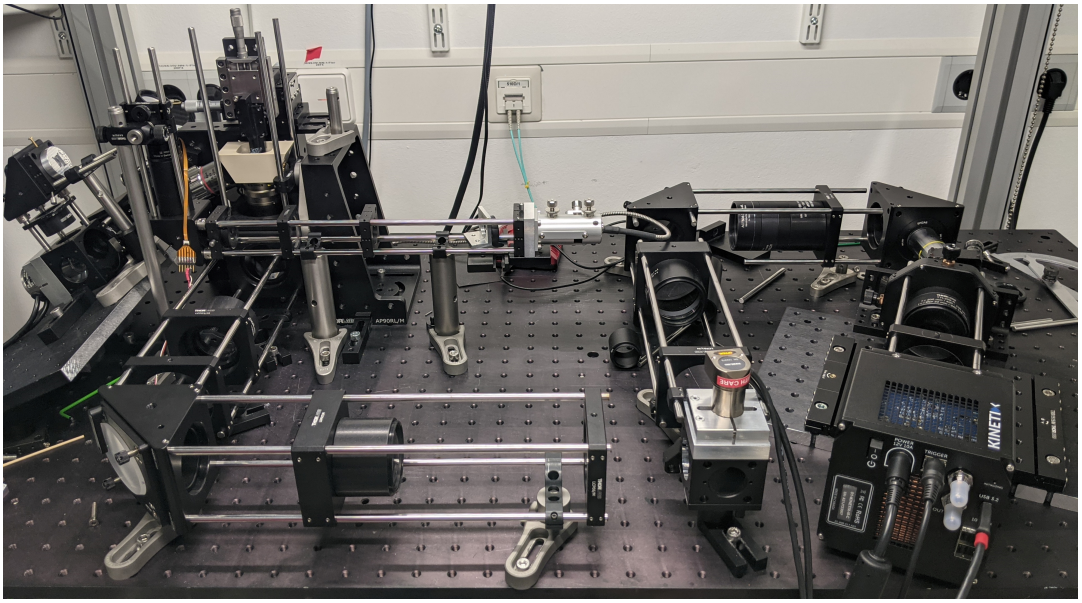

FIGURE 3.16: Assembled microscope on an optical bench.

All three units the illumination unit, the remote focusing unit, and the detection unit of the microscope are aligned separately. The order of alignment of critical for good results. The remote focusing unit is aligned first, followed by the detection unit, and then at last the illumination unit. The alignment protocol for the microscope is discussed in detail in Appendix A

3.5 Microscope control unit

There are five devices in the microscope that need to be synchronized precisely: a galvo scanner in the illumination unit, a galvo scanner in the remote focusing unit, an ETL, a camera, and the laser shutter. All devices are connected to the embedded system (Zynq-7000, xc7z020 SoC) which is connected to the workstation with a user interface for device communication. The device synchronization, FPGA programming, and the development of custom LabVIEW code were done by Alejandro Ortiz from the EMBL electronics workshop. An FPGA is responsible for generating the signals to drive the devices while being synchronized. The LabVIEW software takes input parameters from the user and sends them to the FPGA which calculates the output signals in real-time with microsecond precision. The signal traces for the synchronized devices to acquire two stacks in one galvo scan is shown in Figure 3.17. Signals for both galvos are the same, so only one galvo is shown in this figure.

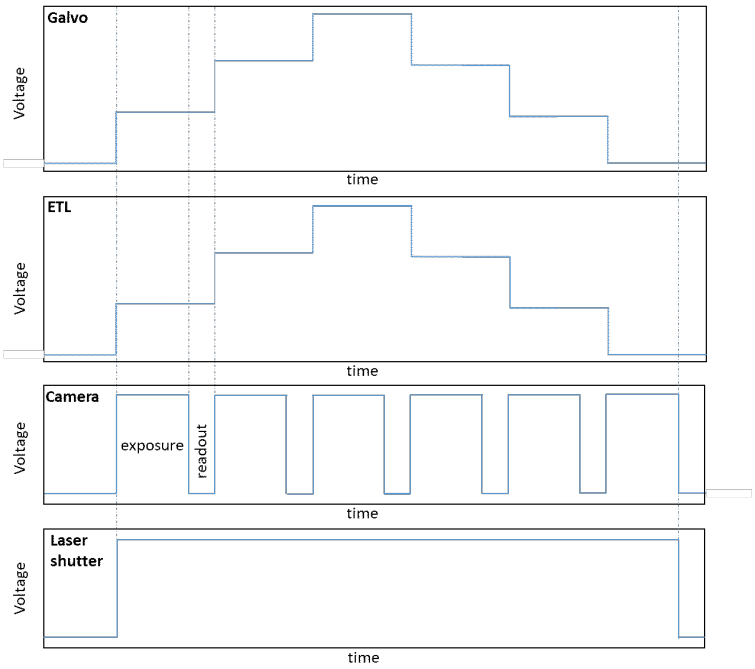

FIGURE 3.17: Example traces for recording a stack with three images. In one scan, two stacks of 3 images each are recorded. One when the galvos are moving in the forward direction and one when the galvos are moving back to the initial position. The camera records an image at each galvo step, thus capturing six images in total. The laser shutter is programmed to remain open until the galvos finish a complete scan, coming back to their initial position.

Chapter 4

Optical properties of the MesoOPM

The point spread function (PSF) of the system is indicative of the overall optical performance of the system. I simulated the PSF of the microscope that I built using two different approaches. In the first approach, I theoretically calculated the PSF by obtaining an overall pupil of the system and transmitting the emitted fluorescence through that pupil. This can be taken as a benchmark and a practically built system should approach this theoretical limit. In practice, optical components introduce various aberrations which can lead to deterioration of the experimentally measured PSF. A more practical approach is to simulate the PSF using Zemax. This method takes into consideration the effect of different optical components on the overall system PSF. Although it is closer to the real-life situation, the drawback of such a method is that usually, the exact Zemax models of objective lenses are not available. To experimentally validate the resolution of the system, the PSF of the system is measured by imaging diffraction-limited beads. Before calculating the resolution of the microscope, one has to figure out the correct 3d volume reconstruction of acquired stacks. Due to the non-orthogonal reference system in the acquired volume, the reconstruction of the volume requires some 3D transformations. Hence, I start by first discussing the 3d volume reconstruction in OPM.

4.1 3d volume reconstruction

The process of acquiring 3d stack on a NODO microscope is described in Figure 4.1. Imagine we acquire a 3d stack of a cylinder with diameter d. The light-sheet is scanned through the volume at 65° w.r.t the optic axis (z-axis) of the detection objective along the y-axis. On the camera, each acquired image of the cylinder will be an ellipse with dimensions d and $d/\cos(65^\circ)$.

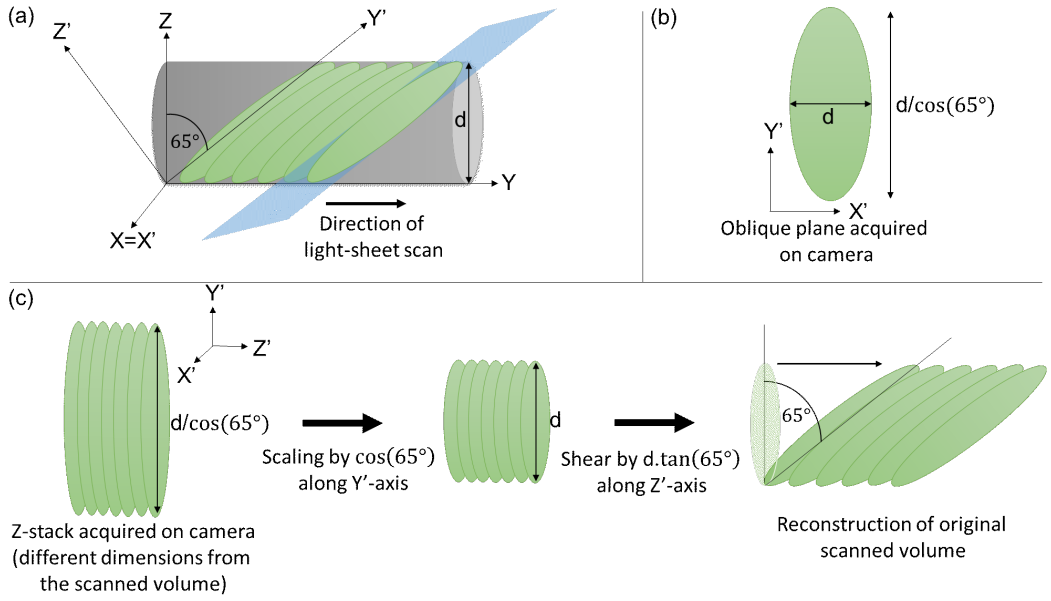

FIGURE 4.1: 3d volume reconstruction in OPM. (a)The light-sheet scanned along the y-axis through the sample which makes 65 degrees angle with the optic axis (z-axis) of the detection objective. (b) Single image acquired of a slice through the cylinder on the camera. (c) 3d reconstruction of the volume in coordinate system corresponding to the sample space.

The 3d stack of these images will not be a cylinder anymore. Now we want to reconstruct the volume from the stack which matches the true dimensions of the sample. The stack is first scaled down by $\cos(65°)$ in y'-axis and then sheared along the z'-axis by $d.\cos(65°)$ as shown in Figure 4.1(c). Finally, the volume reconstructed will match the actual dimensions of the sample.

To establish the transformation matrix for 3d reconstruction volume correctly, a cylindrical sample of known diameter was imaged using MesoOPM. The cylinder was made with 1% gelrite solution in water. The gelrite solution is sucked up through a cylindrical micropipette which has an inner diameter of 0.64 mm. Once the gel solidifies, it is pushed out of the micropipette and placed on the sample holder. The sample holder is then filled with fluorescene solution, which is fluorescent in visible light. The gelrite solution is transparent and is non-fluorescent. When the sample chamber is illuminated, the fluorescence signal will be detected around the cylinder and the cylinder itself will appear dark. 3d stack of the cylinder is acquired on the camera and the volume is reconstructed as shown in Figure 4.2. The final matrix (M_{final}) for Affine transformation is combination of the scaling (M_{scale}) and shearing (M_{shear}) matrices. Matrix multiplication is non-commutative, thus the order of matrix multiplication must be taken care of. The final transformation matrix can be constructed as follows:

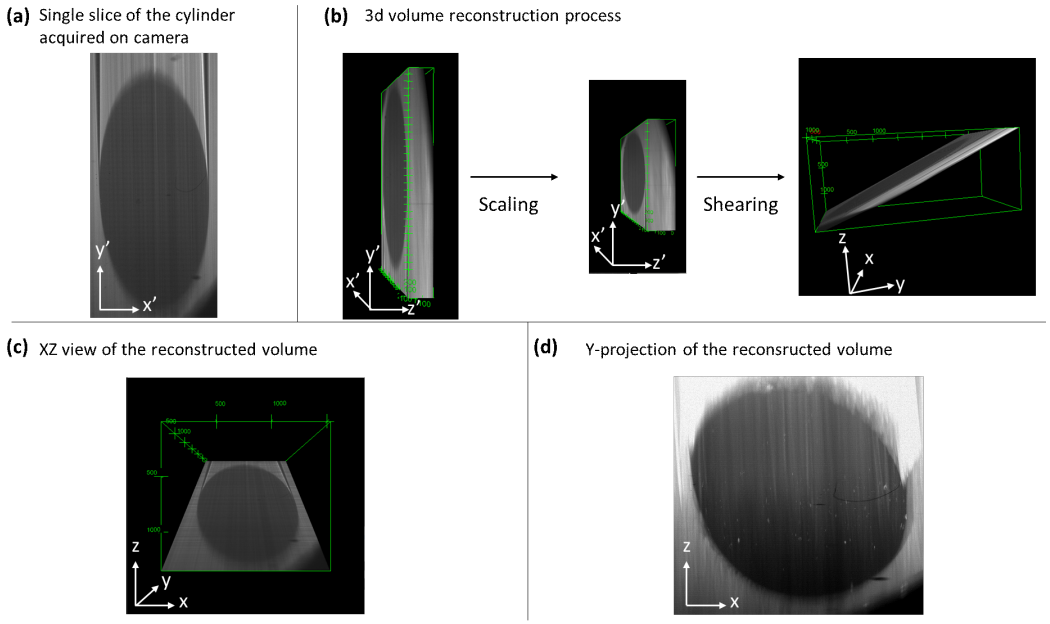

FIGURE 4.2: Reconstructing a cylinder experimentally. (a) Single image acquired of a slice through the cylinder of diameter 0.62mm on the camera. (b) Process of 3d reconstruction of the cylinder in coordinate system corresponding to the sample space. (c) The XZ view of the reconstructed stack. (d) y-projection of the cylinder.

$$M_{final} = M_{scale} * M_{shear}$$

$$M_{final} = \begin{bmatrix} 1 & 0 & 0 \\ 0 & \cos(65^\circ) & 0 \\ 0 & 0 & 1 \end{bmatrix} * \begin{bmatrix} 1 & 0 & 0 \\ 0 & 1 & 0 \\ 0 & \tan(65^\circ) & 1 \end{bmatrix}$$

$$M_{final} = \begin{bmatrix} 1 & 0 & 0 \\ 0 & \cos(65^\circ) & 0 \\ 0 & \sin(65^\circ) & 1 \end{bmatrix}$$

4.1.1 Setting the correct voxel size

One thing that should be taken into consideration when reconstructing the volume is the voxel size. The total magnification of the system is 13.33X and the pixel size of the camera is $6.5 \times 6.5\,\mu m^2$. Thus, the lateral voxel size is straightforward to calculate and is $0.488 \times 0.488\,\mu m^2$. In NODO, the volume is scanned using an additional galvo on the illumination side. In MesoOPM I am using a digital galvo scanner with a minimum step size of d= $0.552\,\mu m$. This is measured by placing a camera directly at the focal plane of the illumination objective and distance moved along the focal plane by the light-sheet

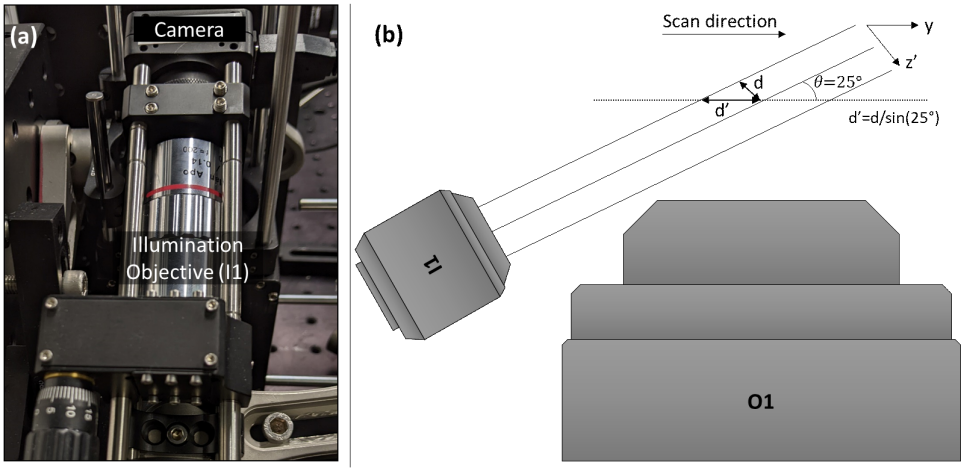

FIGURE 4.3: Measuring the axial voxel dimensions in an OPM. (a) The distance 'd' moved by the light-sheet along the focal plane while galvo scanning can be measured by placing the camera directly at the focal plane of the illumination objective. An image is acquired at each galvo step and by projecting the images, one can calculate the distance moved when the digital galvo moved one step, which is the minimum step possible for this digital galvo. (b) The galvo will scan the light-sheet along the z'-axis, but an ETL (explained in Figure 3.6) will push the light-sheet waist to always stay along the image plane of the detection objective O1. Thus galvo scanning combined with ETL focal length adjustment effectively scans the light-sheet along the y-axis in MesoOPM.

in each galvo step increase can be measured. But this distance is along the focal plane of the illumination objective (z'-axis) as indicated in Figure 4.3. With the help of ETL, the light-sheet is effectively scanned along the image plane (y-axis) of the detection objective (Figure 3.6). Thus the step size in the y-direction is d'$= 0.552/\sin(25^\circ) = 1.3\,\mu$m. During the scaling and shearing process, the distance between the two planes along the y-axis (d') remains unchanged. Hence to match the actual distance between the two planes, the voxel size should be set to $0.488 \times 0.488 \times 1.3\,\mu m^3$ before reconstructing the stack. After setting the pixel size, apply the transformation matrix to the acquired stack and the outcome will be a volume reconstructed into sample coordinates.

4.2 PSF Simulations

4.2.1 Theoretical simulation of the PSF

The fluorescence emitted from the sample is considered to be isotropic. Due to the limited NA of the primary objective, only a part of the solid angle is allowed to transmit through the pupil of O1 (Figure 4.4). The O2 pupil is

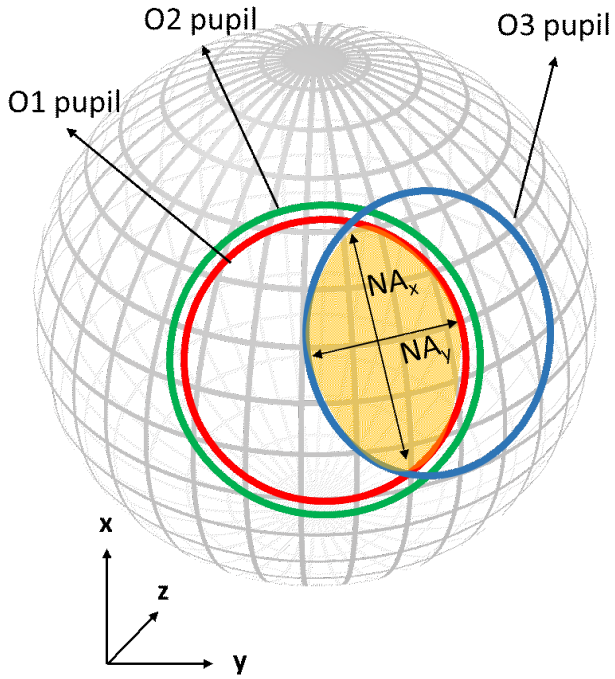

FIGURE 4.4: Visualization of the system pupil. The unit sphere represents the isotropic fluorescence emission. The red circle is the pupil of O1 that will transmit only a part of fluorescence which is dictated by its NA. The O2 pupil (green circle) is concentric to O2 and is bigger than that of O1 due to the demagnification of the beam. The blue circle represents the pupil of O3 which is tilted by 25 degrees about the x-axis in the yz plane. The shaded region in yellow is the overall pupil of the system. Due to tilt, the NA along the x and y axes is different leading to anisotropic lateral resolution.

conjugated to that of O1 and doesn't limit the transmission because the beam is demagnified 1.33 times before entering the O2 pupil. After exiting the O2 pupil, the beam will hit the pupil of O3. Pupils of objective O2 and O3 lie at an angle, thus only part of the light cone will be allowed to transmit through the O3 pupil. The overall effective pupil of the system will have different dimensions in the x and y direction and thus the effective NA in the x and y direction will be different leading to anisotropic lateral resolution. The overall pupil function of the system was calculated using a simulation tool developed by Glaser *et. al.* [34] and is plotted in Figure 4.5(a). If the final pupil function is given by $P(k_x, k_x)$, the 3d PSF is simply the square of the Fourier transform of the pupil function and can be calculated as:

$$PSF(x,y,z) = \left| \int\int P(k_x,k_y) e^{2\pi i(k_x x + k_y y)} e^{2\pi i k_z(k_x,k_y) z} dk_x dk_y \right|^2 \tag{4.1}$$

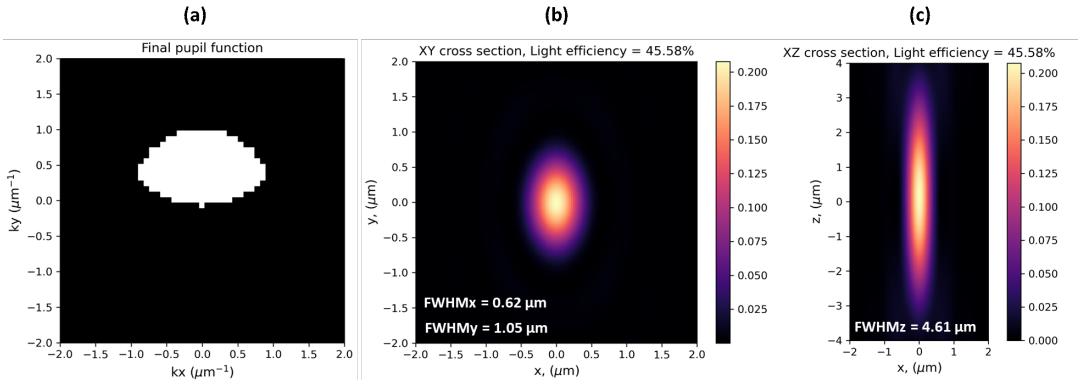

FIGURE 4.5: Theoretically simulated PSF.(a) Overall pupil function of the system is calculated by dividing the overlapping area of the pupil O1 and O2 by the total area of the O1 pupil. (b) The lateral PSF is plotted and the FWHMx and FWHMy are 0.62 µm and 1.05 µm respectively. (c) The axial cross-section of the PSF is plotted and the FWHMz is 4.61 µm. The geometrical light loss due to the tilt of the system is approx. 54%.

where k_z is a function of k_x and k_y and is given by $k_z = \sqrt{\frac{2\pi n}{\lambda^2} - (k_x^2 + k_y^2)}$. I calculated the 3d PSF of the system using the same simulation tool. The lateral PSF is shown in Figure 4.5(b). The FWHMx and FWHMy are 0.62 µm and 1.05 µm respectively. The NAy is smaller than NAx, thus the resolution in y-direction is worse than x-direction. The axial PSF is plotted in Figure 4.5(b) and the FWHMz is 4.61 µm.

The total transmission loss in OPM is composed of two different types of losses. One, due to transmission loss from optical elements, and the second, due to the geometrical loss caused due to the angle between O2 and O3. The geometrical light loss can be simply calculated by measuring the overlapping area of the pupils of O1 and O3 shown as a shaded region in Figure 4.4 divided by the total area of the O1 pupil. For our system, the geometrical loss is approximately 54%.

4.2.2 Simulating the PSF using Zemax

After calculating the theoretical PSF, I built the Zemax model of the microscope and simulated the 3d PSF. The model is described in Figure 4.6(a). In practice, I use 10X 0.5 NA WD objective as O1 and 10X 0.45 NA air objective as O2 and O3. The Zemax models of these objectives are not available, so I used a Zemax blackbox of 10X air objectives as O1, O2, and O3. The entrance pupil NA was set to 0.45 in Zemax. All other lenses in the model are the same, which are blackboxes of the TTL200MP tube lens from Thorlabs. The

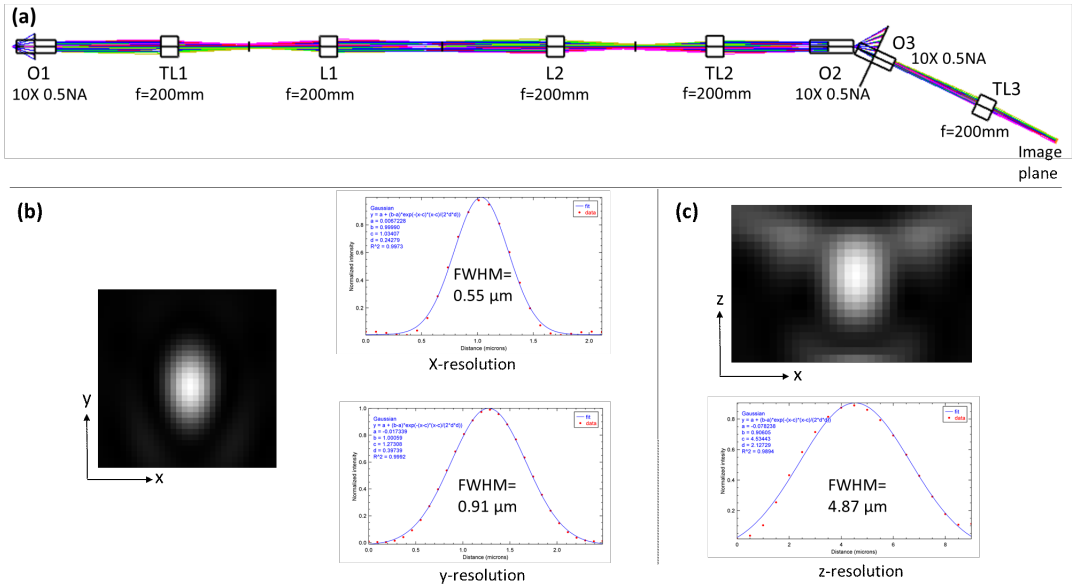

FIGURE 4.6: Simulated PSF using Zemax. (a) The Zemax model of the microscope. (b) Lateral PSF was simulated using Zemax and the x and y resolution is quantified in the graphs. (c) The axial PSF is simulated using defocus method in Zemax and the axial resolution is quantified to be 4.87 µm.

object plan was tilted by 25 degrees as is the case in practice and the detection arm was thus also tilted by 25 degrees w.r.t the objective O2. The lateral PSF of the microscope was measured at the image plane. For calculating the 3d PSF, the gray values of a point source were measured at defocused planes and later projected in the xz plane. The final voxel size of the 3d volume was $0.083 \times 0.083 \times 0.5\,\mu m^3$. The lateral resolution is plotted in Figure 4.10(b), the FWHMx is 0.55 µm and FWHMy is 0.91 µm. These numbers are slightly better than the theoretical PSF calculated. The reason for that might be the use of 0.5 NA objective as O3 in the Zemax model which will effectively increase the NAx and NAy slightly. The FWHMz (Figure 4.10(c)) is 4.87 µm, which is slightly worse than the theoretical model, which might be due to the aberrations caused by optical elements of the system. It is worth mentioning here that while simulating the PSF, the illumination was not taken into consideration. The PSF of the system might vary depending on the thickness of the light-sheet.

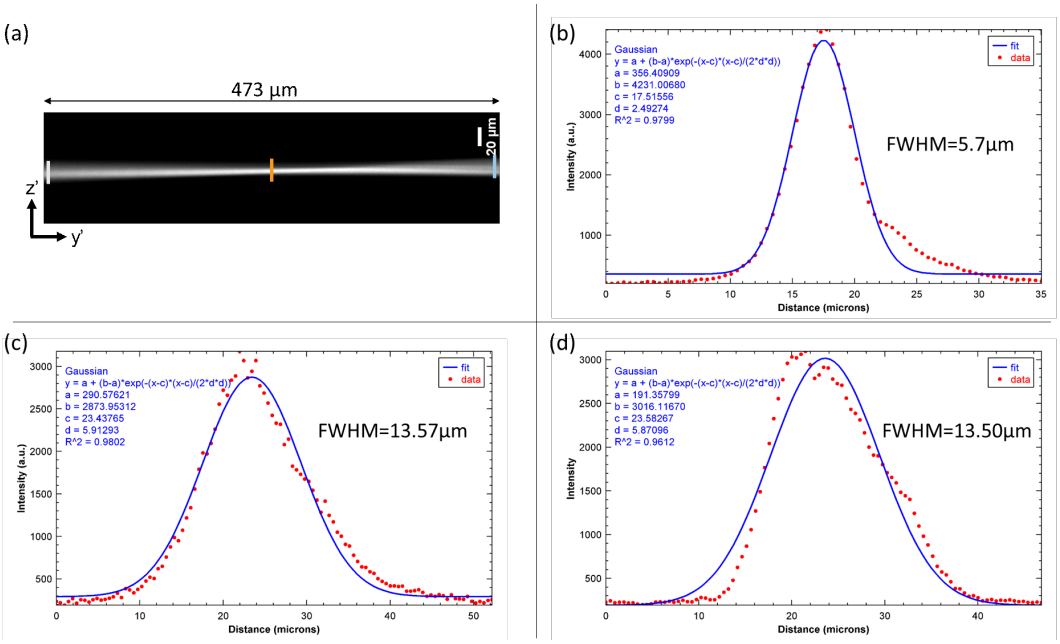

FIGURE 4.7: Light-sheet profile. (a) The illumination Gaussian beam across the FOV which corresponds to the axial FOV is shown. Three measurment cross-sections are indicated. The beam diameter (FWHM) at the center is plotted (b) and is slightly above the theoretical axial resolution (5.25 µm) of 10X 0.45 NA objective. At the edges, the light-sheet thickness becomes 13.5 µm as seen from (c) and (d).

4.3 Experimental validation of the MesoOPM

4.3.1 Light-sheet profile

In light-sheet microscopy, the illumination beam profile plays a major role in determining the resolution and the optical sectioning capabilities of the microscope. The first step towards measuring the optical properties of the system is to measure the light-sheet profile. The appropriate parameters required to image Nematostella and to cover the full FOV are discussed in subsection 3.2.1. The light-sheet with beam waist 5 µm is generated using the illumination scheme of the microscope discussed in subsection 3.2.3. Light-sheet parameters such as the light-sheet waist, thickness of the light-sheet at the edges of the axial FOV were quantified and are plotted in Figure 4.7. A Gaussian curve was fitted to the measured gray values on the camera to calculate the light-sheet thickness. The side-view of the light-sheet as imaged on the camera is shown in Figure 4.7(a). The length of the light-sheet is 473 microns and this light-sheet is tilted by 65 degrees w.r.t. the detection optic axis. Thus in the detection coordinate system, this light-sheet will cover $473 \cdot \sin(65°) = 236$ µm FOV in the axial direction, which is about the width of a Nematostella. The gray values across the light-sheet waist (also called

light-sheet thickness) are plotted in Figure 4.7(b). The light-sheet thickness (w) can be calculated from the FWHM as:

$$W_{y'=0} = 5.7\,\mu m/\sqrt{2 \cdot \ln(2)} = 4.9\,\mu m.$$

I also calculated the thickness at the edges of the light-sheet similarly,

$W_{y'=+236} = 13.57\,\mu m$ and $W_{y'=-236} = 13.5\,\mu m$. I further went on to calculate the height of the light-sheet. The lateral cross-section (x'z' plane) of the light-sheet at its focus is shown in Figure 4.8(a). The Gaussian curve was fitted to the measured gray values. The FWHM is measured to be 1.03 mm and thus the waist of light-sheet along the x' direction is

$$h_{ls} = 1.3\,\mu m/\sqrt{2 \cdot ln(2)} = 0.88\,mm.$$

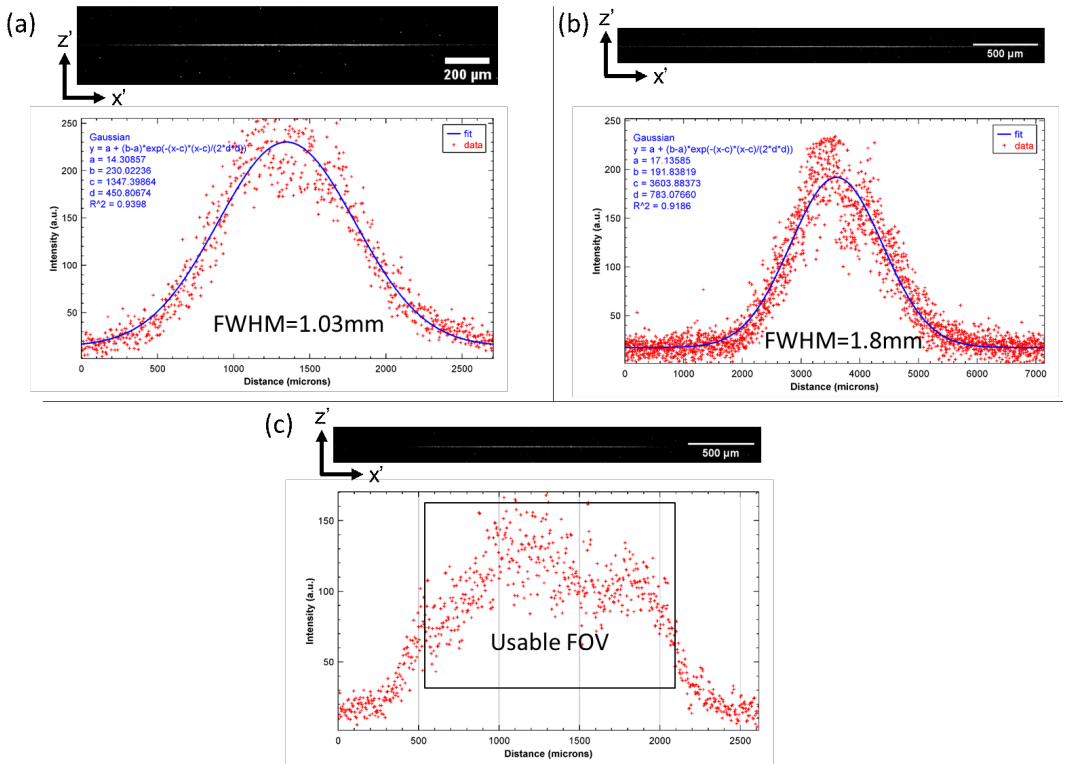

FIGURE 4.8: Field of view of the light-sheet. (a) The Gaussian beam generated with required beam waist of 4.9 µm has the FWHM of 1.03 mm and thus is not enough to cover the FOV on the camera. (b) The beam is expanded such that the final diameter is 5.8 mm. One can appreciate that the FWHM is enough to cover the full FOV on the camera. (c) The beam is clipped using an iris such that it illuminates only 1.5 mm FOV and the gray values over the FOV are plotted. The intensity drops slowly over the FOV.

The height of the light-sheet is approximately equal to the beam waist (Equation 2.21). Thus the FOV with this light-sheet will not be enough to

cover the full camera chip. To solve this issue, we expanded the beam 8.33 times such that the final beam diameter is 5.8mm. Then I calculated the height of this light-sheet. The height of this light-sheet is 1.54 mm. This matches the FOV we can image on the camera chip. The drawback of this beam is that the length of the light-sheet will be smaller because the NA of the beam has increased. The expanded beam is then clipped off to illuminate 1.5mm FOV, i.e. entire camera chip. The resulting beam shown in Figure 4.8(c) will not be a Gaussian anymore. The measured gray values at the focus of this light-sheet are plotted in Figure 4.8(c) and useable FOV is marked. The thickness of this beam at the center and the edges was calculated and is shown in Figure 4.9. One can appreciate the fact that the FWHM of the light-sheet is now comparable to the theoretical axial resolution of the microscope. At the edges, the width of the thickness of the light-sheet is similar to that of the Gaussian beam shown in Figure 4.7.

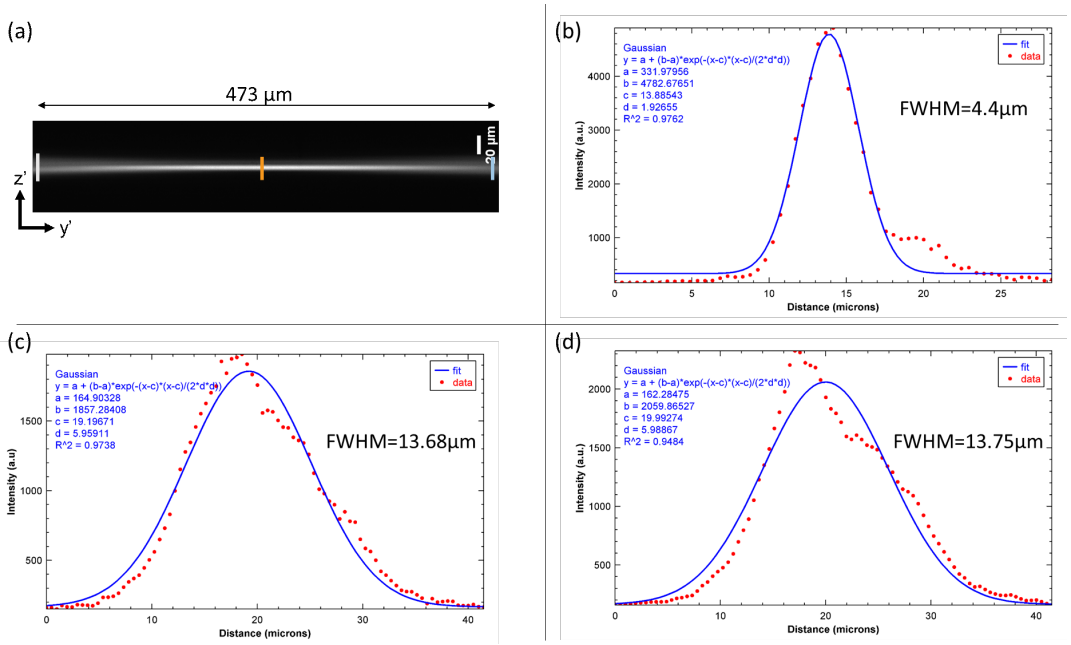

FIGURE 4.9: Illumination light-sheet profile. (a) The clipped beam profile is shown here. Three measurement cross-sections are indicated. (b) The FWHM at the waist is 4.4 µm, which is smaller than the Gaussian beam we characterized in Figure 4.7 and at the edges of the FOV, the thickness is comparable in both the beams as shown in (c) and (d).

4.3.2 Experimental measurement of PSF

The optical properties of any microscope are demonstrated by acquiring a 3d stack of beads suspended in the transparent gel through the system. The resolution and usable FOV are determined by calculating the FWHM of beads

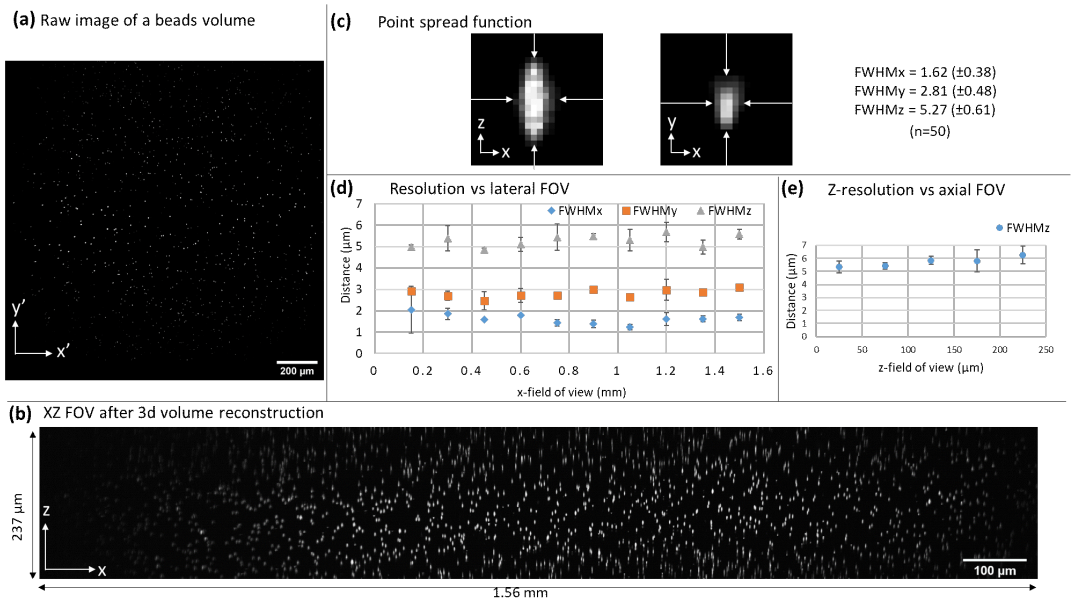

FIGURE 4.10: Experimental measurement of the PSF. (a) A single raw image of a 3d stack of beads over the FOV of ($1.56 \times 1.56\,\text{mm}^2$). (b) The beads projected along y-axis in xz plane are shown over the axial FOV of 237 µm. (c) The lateral PSF and the axial PSF are shown and the FWHMx, FWHMy and FWHMz are 1.62 µm (± 0.38), 2.81 µm (± 0.48) and 5.27 µm (± 0.61) respectively. (d) The resolution as a function of lateral FOV is plotted. (e) The axial resolution is plotted as a function of axial FOV.

across the desired FOV in axial and lateral directions. I prepared bead samples by suspending beads with diameter 0.5 µm in 1% gelrite solution. I mounted this beads sample on the microscope and acquired a 3d stack under ordinary atmospheric conditions and room temperature. Figure 4.10(a) shows a single raw image of the sample ($1.56 \times 1.56\,\text{mm}^2$). 3d stack was then transformed to an appropriate coordinate system. I previously discussed that the sample is scanned in the y-direction, thus to calculate the axial FOV of the microscope, the beads 3d volume was projected in the y-direction and is shown in Figure 4.10(b). The PSF of the system is shown in Figure 4.10(c) where a single representative image of axial and lateral PSF is shown. The whole FOV was divided into 10 sections of 150 µm width (along the x-axis) each and five beads were picked at random to calculate FWHMx, FWHMy, and FWHMz for each bead. The FWHM averaged over these 50 beads and the FWHMx, FWHMy, and FWHMz are 1.62 µm (± 0.38), 2.81 µm (± 0.48) and 5.27 µm (± 0.61) respectively. The average value and the standard deviation from each section are plotted on the graph in Figure 4.10(d) which gives us an idea of the dependence of resolution on the FOV. The x-resolution in

the microscope is limited by the pixel size. According to the Nyquist sampling theorem, the data should be sampled at least twice the frequency of the signal to reconstruct the signal properly [51]. The pixel size is 0.488 µm and thus the resolution should be approximately two times i.e. $\approx$ 1 µm. One can see from Figure 4.10(d) that the x-resolution is worse at the edges of the FOV than in the middle, where the values approach the theoretical limit. The y-resolution is limited by the minimum scan step of the galvo. Each step of the galvo corresponds to 1.3 µm in the y-direction as discussed in detail in subsection 4.1.1 and thus according to the Nyquist criteria, the y-resolution should be around two times i.e. 2.6 microns, which matches the experimentally measured value of 2.81 µm. From Figure 4.10(d) one can see that the y-resolution remains below 3 µm across the whole FOV. z-resolution values fluctuate between 5 and 6 µm across the lateral FOV. The dependence of axial PSF was also plotted across the axial FOV. The axial FOV was divided into five sections of 50 µm each and the FWHM of five beads from each section are averaged and plotted. One can notice that as the light-sheet goes deeper into the gel, the z-resolution starts to deteriorate and can reach up to 7 µm at the far end of the FOV from the detection objective surface. Once again, I would like to emphasize that at the lateral FOV >1.5 mm, this is the first-ever report of an oblique plane microscope with axial resolution below 10 µm. The values for PSF that I achieved on the MesoOPM are near the theoretically predicted values.

Chapter 5

Nematostella imaging

In this chapter, I will demonstrate the imaging capabilities of the microscope I designed and built. Nematostella lines which are used for imaging in this chapter were a kind gift from Ikmi lab at EMBL. The biological sample preparation and mounting were solely done by Kaushikaram. I carried out image acquisition of the data presented here in presence of Kaushikaram and I solely performed the data analysis. All the data was acquired under ordinary atmospheric conditions and room temperature.

5.1 Sample mounting

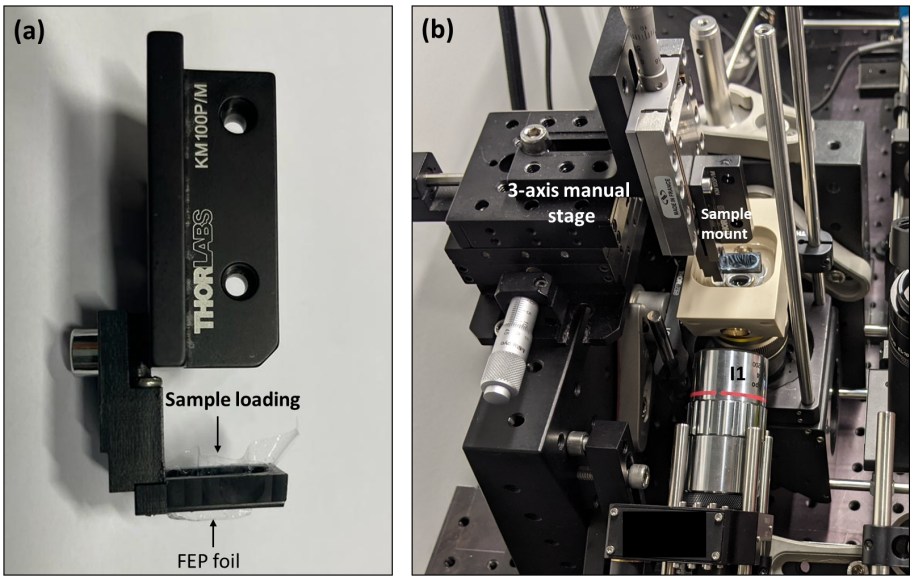

FIGURE 5.1: Sample mounting. (a) The sample is loaded in the mount from the top and it will rest on the FEP foil which exposes the sample to illumination light-sheet. (b) The sample mount is fixed on the 3-axis stage for locating the sample.

The MesoOPM is built in an open-top configuration. Any custom-designed sample mount with an FEP bottom can be used to load a sample to be imaged. In our case, as a proof of concept, we are using a wedge-shaped FEP bottom mount as shown in Figure 5.1. The FEP foil is transparent and has a refractive index ($n = 1.34$) close to water, thus introducing minimal aberrations when light crosses foil and water interface. The mount is fixed on a manual 3-axis stage using which the specimen can be brought to the center of the FOV. The animal is loaded on the mount from the top and is then free to move around in the sample mount.

5.2 Imaging muscle structure

The first example that I will show is imaging Nematostella muscle structure in an anesthetized animal. Muscles play an important role in the survival of Nematostella by allowing the animal to uptake fluids and food from the surroundings by generating peristaltic waves along the oral-aboral axis. Imaging muscle structure can thus shed more light on how the animal behavior changes according to the surroundings. I imaged Nematostella in which the muscle cells express mNeonGreen protein, which is excited by $\lambda_{ex} = 488\,\text{nm}$ and emit fluorescence at $\lambda_{em} = 532\,\text{nm}$. The total laser power at the sample was 0.5 mW for an exposure time of 40 ms and images were acquired at 20 fps. The 3d volume of an anesthetized Nematostella was reconstructed using *TransformJ* plugin in the ImageJ software which is shown in Figure 5.2. 3d projection of the volume is shown in Figure 5.2(a). The cross-section which is indicated is shown in Figure 5.2(b). The bright spots are the longitudinal muscles and the structure between the longitudinal muscles are the circular muscles present in the gastrodermis. The quality of details that are present on the side of illumination is better than the far end of the sample. Due to the scattering and absorption of the illumination beam passing through the initial layer, the quality deteriorates. From the zoom-in shown in Figure 5.2(c) well-formed circular muscles present in the gastrodermis can be resolved and is quantified for the line marked here in Figure 5.2(d). The structure is similar to what has been reported in the literature imaged in fixed specimen [52]. Although I imaged an anesthetized animal, as a proof of principle, I have shown that MesoOPM can resolve the muscle structure in the Nematostella which opens up new possibilities to study the changes in morphology while the animal is behaving freely.

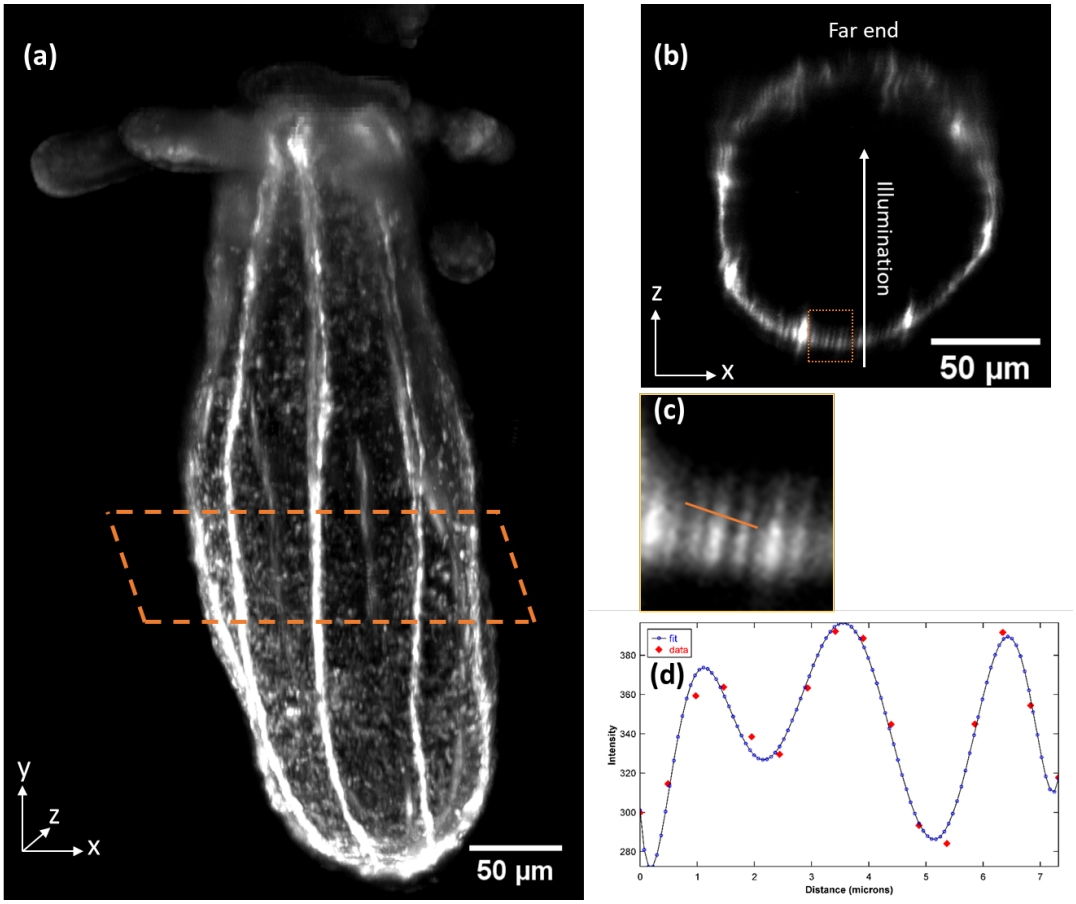

FIGURE 5.2: Imaging muscle structure of Nematostella. (a) 3d projection of the reconstructed volume of Nematostella imaged on MesoOPM. The bright fiber-like structures running along the body are longitudinal muscles, also called *parieral muscles*. (b) The cross-section of the 3d volume is indicated in (a). The bright spots are the longitudinal muscles and the structure between the longitudinal muscles with a relatively weak signal are the circular muscles present in the gastrodermis. Both muscle types are well resolved. The area marked in the dotted square is further zoomed-in in (c). The gray values along the line indicated are plotted in (d) for quantification and the circular muscles are well resolvable.

5.3 Imaging nervous system of Nematostella

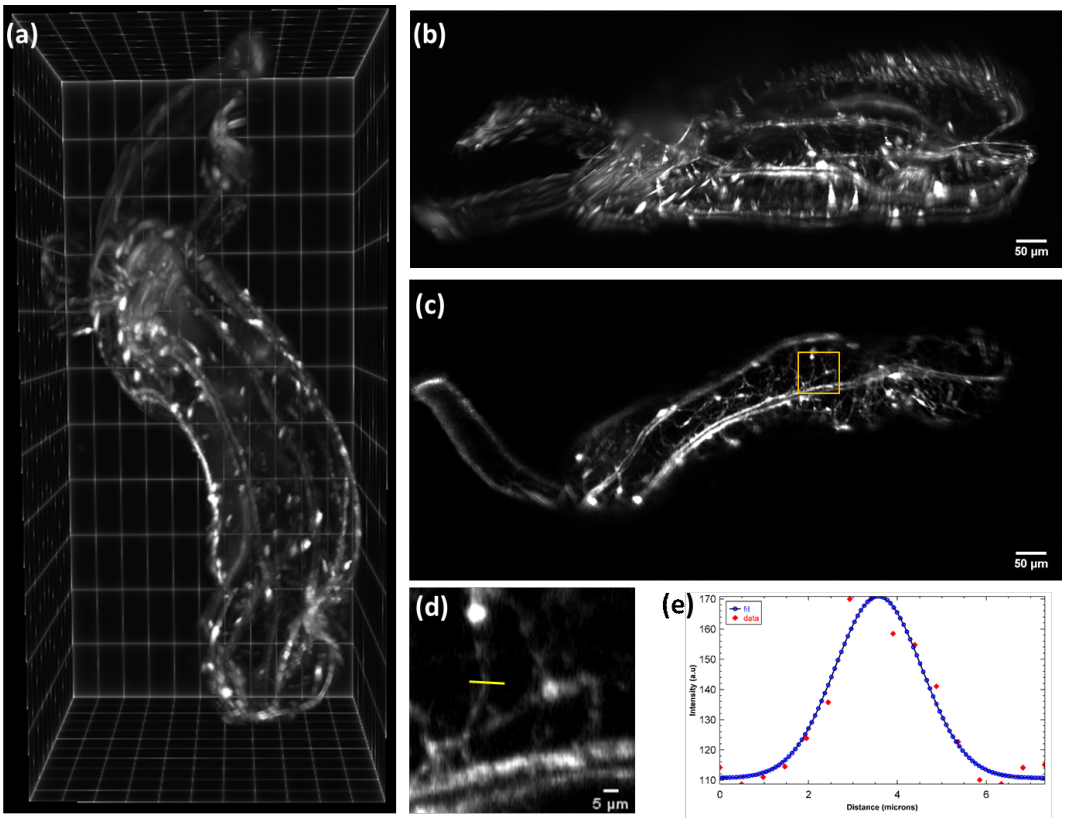

FIGURE 5.3: Imaging Nervous system Nematostella. (a) 3d rendering of the reconstructed volume showing the nervous system of Nematostella. (b) 3d projection of the volume shows that the movement of the specimen causes motion blur. (c) The single plane from the 3-d volume is shown and the detailed nervous system is visible. (d) Zoom-in of the single plane (e) Thickness of an axon in the nervous system is quantified.

In evolutionary terms, Nematostella belongs to the phylum Cnidaria which is one of the earliest animals to develop the nervous system. Thus studying the nervous system in Nematostella can help advance our knowledge about the nervous system evolution. I imaged the nervous system of Nematostella that expressed GFP driven by the Elav promoter. The GFP is excited by $\lambda_{ex} = 488\,\text{nm}$ and emits fluorescence at $\lambda_{em} = 532\,\text{nm}$. The total power was 0.5 mW with an exposure time of 50 ms and the images were acquired at 20 fps. The 3d rendering of the reconstructed volume is shown in Figure 5.3(a). The 3d projection is shown in Figure 5.3(b) and it is clear that the image acquisition is too slow at this rate. The specimen movements caused motion blur and makes it hard to extract any quantitative information. A single plane from the 3d stack is shown in Figure 5.3(c) and one can

appreciate the details present in the image. Neurons and the neurites connecting neurons are resolvable and a zoom-in from this image is shown in Figure 5.3(d). The Gaussian curve fitted to the measured gray values across the cross-section indicated in Figure 5.3(d) is plotted in Figure 5.3(e). Even though one can resolve the nervous system structure in nematostella, imaging animal at low speeds is not ideal. High-speed volumetric imaging is preferred which will allow us to image the nervous system while the animal is 'quasi-static'.

5.3.1 High-speed volumetric imaging

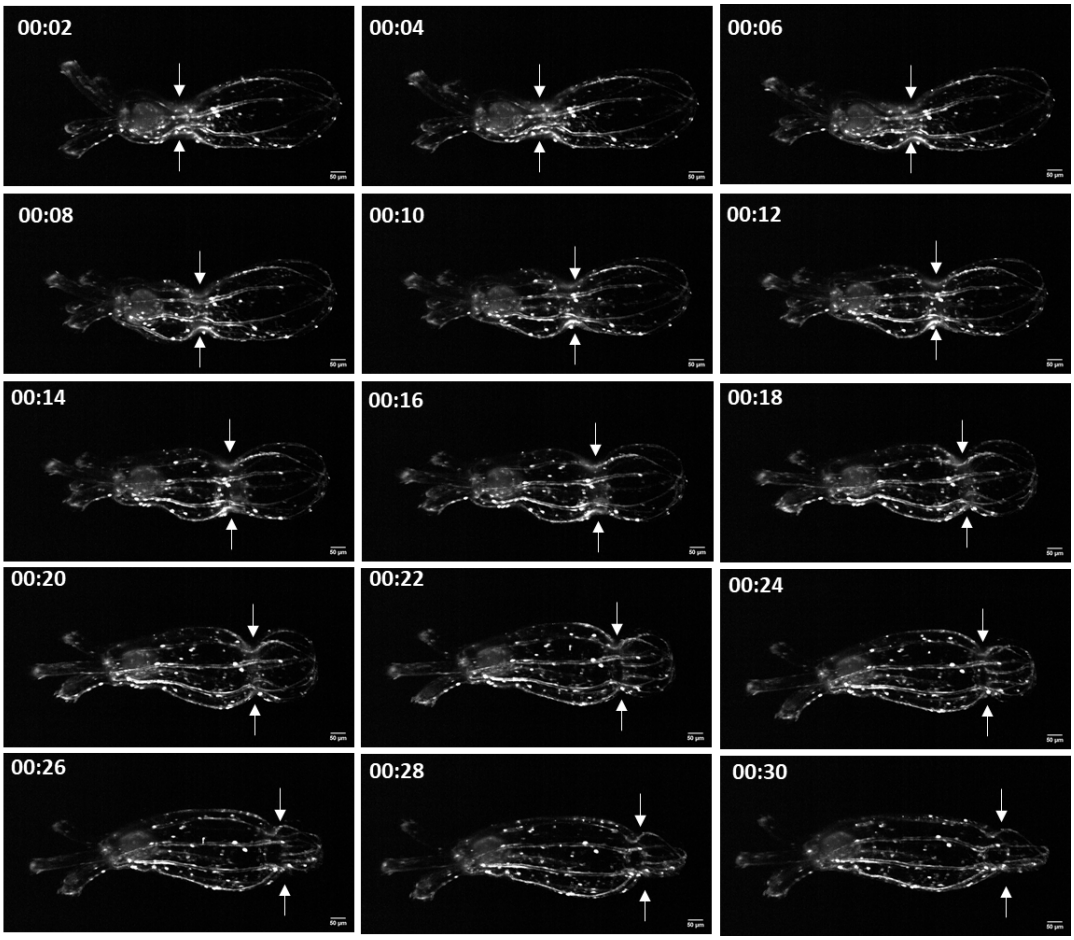

FIGURE 5.4: Time series of Nematostella undergoing Peristaltic wave along the oral-aboral axis. Scale bar: 50 µm Timestamp: mm:ss.

From Figure 5.3 it is clear that the microscope is capable of spatially resolving the nervous system of Nematostella, but slow image acquisition speeds cause the motion blur. I went on to showcase the high-speed volumetric imaging capabilities of MesoOPM by imaging Nemmatostella nervous system while it was going through a contraction wave. The results are shown

in Figure 5.4. Each image is a 3d projection of a volume acquired. The total laser power at the sample was 2 mW and the acquisition time was 1 ms. The images were acquired at 300 fps and each volume is composed of 600 frames. Thus each volume ($1.56 \times 0.78 \times 0.24\,\mathrm{mm}^3$) is acquired every 2 seconds, which has never been possible before for imaging live freely moving Nematostella. MesoOPM is capable of imaging over the FOV of $1.56 \times 1.56 \times 0.24\,\mathrm{mm}^3$, by scanning 1200 frames to cover the whole FOV, but 600 frames were enough in this case to image the animal in its entirety. This demonstration of imaging several 3d volumes at such spatiotemporal resolution allows us to visualize the nervous system of Nematostella while the animal is behaving freely. Such capabilities can have huge implications in the future to study how the nervous system and muscle structure interact with each other leading to particular animal behavior and how their interaction changes if the environment is changed. In general, MesoOPM can be used to study the interaction between animal behavior and the environment by visualizing the underlying cellular structure of Nematostella.

Chapter 6

Outlook

The development of a new microscope is an iterative process and one can keep on making improvements gradually or direct its capabilities to tailored imaging requirements and sample properties. Making efficient use of my limited time working on this project, I have designed and built the microscope and showcased the imaging capabilities by demonstrating high-speed imaging of freely moving Nematostella at an organismal scale. In this chapter, I will discuss possible directions one can take to expand the horizon of my work further.

6.1 Improving signal strength

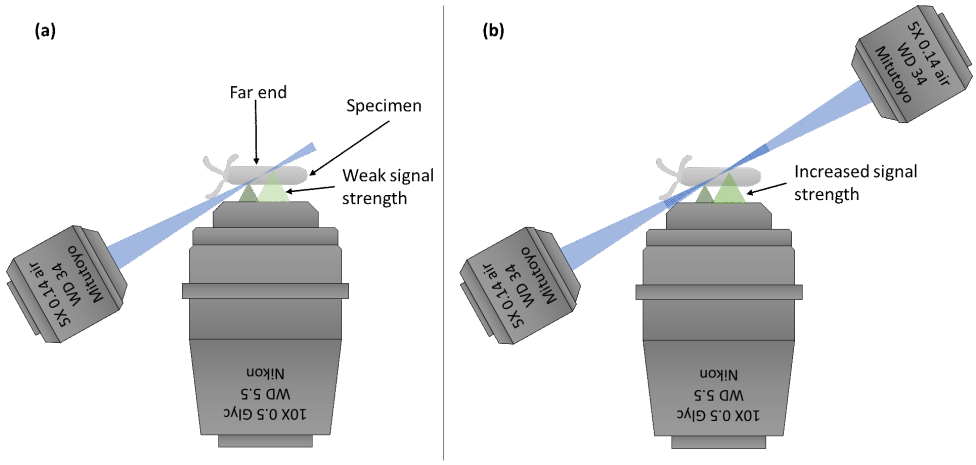

FIGURE 6.1: Dual illumination MesoOPM. (a) The specimen is illuminated from one side as a result of which the fluorescent signal coming from far end is weak. (b) Dual illumination will enhance the signal collected from the far end.

Currently, the Nematostella is illuminated using a single objective lens (Figure 6.1) and as a consequence, the signal from the far end of the specimen is weak. There are two main reasons for this. One, the illumination beam gets

scattered by the layer of tissue facing the illumination objective directly before it reaches the tissue layers on the opposite side. Second, the fluorescence that is emitted from the tissue layers lying at the far end has to pass through more tissue layers before reaching the detection objective.

A possible solution would be to implement dual illumination on the microscope. It will directly illuminate the far end of the animal, the result of which the fluorescence signal will be enhanced from that side. The fluorescence signal will still be scattered before reaching the detection objective, but due to increased fluorescence signal, more light will be collected from the far end compared to the single illumination without compromising the flexibility of open-top mounting.

Another possibility to decrease the scattering through the tissue would be to use a self-constructing illumination beam (e.g. Bessel beam) instead of the Gaussian beam illumination. Using Bessel beams increases the penetration depth and decreases the shadowing artifacts [53].

6.2 Dual color imaging

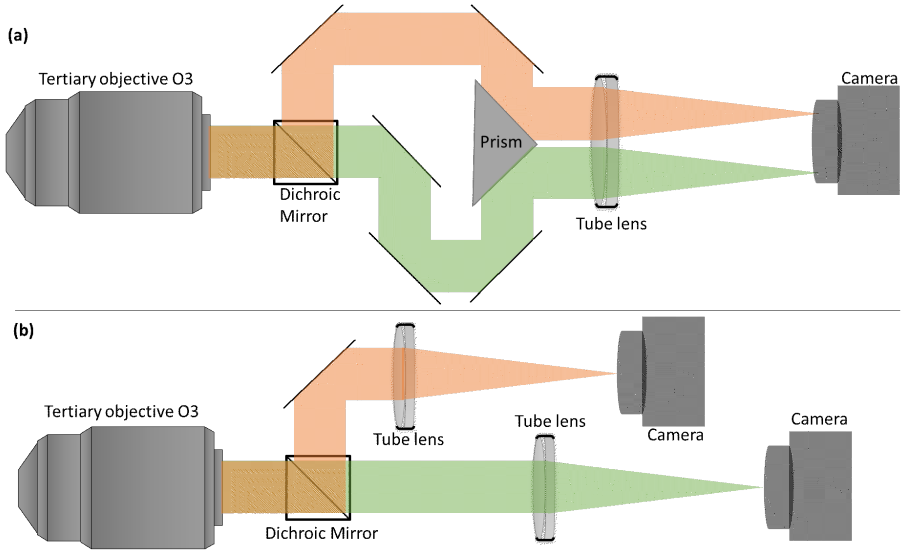

FIGURE 6.2: Dual color imaging configuration. (a) The camera chip is divided into half to image two different fluorescence wavelengths. (b) Two colors can be imaged on a separate cameras, which will give full excess to each camera chip and both colors can be recorded simultaneously.

Dual or multiple color imaging in fixed samples is relatively straightforward. The emission filters are mounted on a filter wheel somewhere in the *infinity space* between the objective and the tube lens. Depending on which color we

want to image, an emission filter can be chosen by rotating the wheel mechanically. Thus, multicolor imaging is done sequentially. The filter wheels require mechanical movements to change the filters and thus will limit the speed of the system drastically. Sequentially imaging dual colors will also make registration harder if the specimen is highly dynamic nature as is the case for us. Another commonly used method that also allows imaging dual colors simultaneously is splitting the wavelengths using a dichroic mirror and then using a prism to image each wavelength of one half of the camera chip (Figure 6.2(a)). The drawback of this method is that the camera chip is divided in half to image each color and we are already limited by the chip size in our system in terms of FOV. A large camera chip is critical to image a large sample. The other option that we have is to image two colors on separate cameras as shown in Figure 6.2(b). The drawback of this method is that the camera that we are using is very expensive (25000 EUR), so the setup will become very expensive.

6.3 Improving imaging and post-processing speed

Currently, MesoOPM is capable of acquiring 300 frames per second. The camera is capable of acquiring 500 frames per second. The galvos in the system are run as master and thus the trigger signal to acquire a frame on the camera is sent by the galvo. I realized that running the camera as a master and sending the trigger signal to drive galvos will enable the system to acquire images at the maximum achievable speed with the camera i.e. 500 frames per second.

So far, the post-processing of images has been done manually using ImageJ. The process is slow and reconstructing one 3d volume takes between 5-15 minutes depending on whether the volume is acquired at 8-bit, 12-bit, or 16-bit. Image analysis pipeline can be developed to process raw volumes and GPU accelerated image processing can be implemented to increase the speed of post-processing.

Chapter 7

Summary and Conclusion

The work presented in this thesis was focused on developing a novel oblique plane microscopy technique that would allow us to acquire volumetric imaging data of a freely moving Nematostella at high speed. The main points of the thesis are summarized below:

- For *in toto* imaging, the size of Nematostella (1-1.5 mm) which requires large lateral FOV is beyond the limits of existing oblique plane microscopy techniques as is discussed in subsection 2.5.2. A 10X objective would be required to achieve the FOV of 1.5-2.0 mm. For any 10X objective, in single objective oblique plane illumination and detection, the light collection efficiency would be zero from secondary (O2) to tertiary objective (O3). Hence, it was decided to decouple the illumination and the detection paths by using separate objectives and launch the light-sheet with the illumination objective at a steeper angle to increase the collection efficiency from O2 to O3.

- Using a different objective for launching the light-sheet at an angle presented with the challenge of light-sheet not being scanned along the image plane of the detection objective which is explained in section 3.2.3. This challenge was solved by implementing an electrically tunable lens that would be synchronized with the galvo scanner. The focus of the light-sheet would be pushed such that it always coincided with the focal plane of the detection objective while scanning.

- Large part of my thesis was devoted to coming up with a microscope design by optimizing trade-offs between the FOV, imaging speed, light-sheet launch angle, and overall light-collection efficiency. Further, I optimized the optical design of the microscope using Zemax software. I started with comparing different tube lenses available commercially and finding the one which can be successfully combined with the primary objective. To achieve aberration-free imaging in oblique plane

microscopy, two tube lenses of different focal lengths are required to combine with the primary and the secondary objective. We required a tube lens of 150 mm focal length in our set-up to be used in combination with O2, which is not available commercially. I eventually custom-designed this lens using Zemax software by combining three different commercially available lenses with an effective focal length of 150mm.

- A complete model of the detection arm of the microscope was simulated using Zemax and the PSF of the simulated system was measured. The PSF of the system was also simulated theoretically by calculating the effective pupil function of the system. Both models are in good agreement with each other and within the ideal design criteria based on the requirements to image Nematostella.

- The 3d Solidworks design of the microscope was developed which provides us with a realistic picture of what the final microscope assembly looks like and one can eliminate possible design flaws.

- The final assembly of the microscope was done on the optical bench and a considerably large amount of time was spent on aligning the microscope. Aligning an oblique plane microscope is known to be tedious due to its unique geometry comprising of multiple objective lenses and some optical components lying in a tilted position to the optical axis of the primary objective.

- After successful assembly and alignment, sub-diffraction-sized beads were imaged on the system and the PSF measurements were shown to be in good agreement with the simulated PSF. The microscope was further validated by imaging the muscle structure of anesthetized Nematostella and the nervous system of a live Nematostella.

Concluding remarks: I accomplished the aim of my thesis by designing and building the MesoOPM, which is the first of its kind, capable of imaging live freely moving large (1-1.5mm) specimen in 3d and 0.5 Hz. I imaged the nervous system and acquired several volumes of live Nematostella while undergoing peristaltic waves at the speed of 300 frames per second. MesoOPM opens a whole new dimension of imaging 3d volume of freely moving specimen with cellular resolution at high-speed. This microscope can be used to understand how certain animal behavior arises at cellular levels while it interacts freely with the environment.

Appendix A

Optomechanical component List

Optomechanical component List			
Label in Figure 3.5	Properties	Supplier & Catalogue #	Comment
L1	f=30 mm	Thorlabs LA1805	
L2	f=250 mm	Thorlabs AC254-250-A	
ETL	f=200 to 100 mm	Optotune EL-10-30-C	
CL	f=40	Thorlabs LJ1402L1-A	
TL1	f=62 mm	Thorlabs AC254-125-A + AC254-125-A	Two f=125 mm achromats arranged back-to-back
GM1	scan range $\pm$22.5 degrees	Hans Scanner	
I1	5X 0.14 NA air	Mitutoyo M Plan Apo	
O1	10X 0.5 NA WD	Nikon MRD71120	
TL2	f=200 mm	Thorlabs TTL200 MP	
L3	f=200 mm	Thorlabs TTL200MP	
L4	f=200 mm	Thorlabs TTL200MP	

GM2	Scan range ±22.5 degrees	Thorlabs QS20X-AG	
TL3	f=150 mm	Thorlabs TTL200MP + ACT508-750-A-ML + ACT508-750-A-ML	Multi-element lens (Figure 3.7)
O2	10X 0.45 NA air	Nikon MRD00105	
O3	10X 0.45 NA air	Nikon MRD00105	
TL4	f=200 mm	Thorlabs TTL200A	

Appendix B

Microscope alignment and calibration

B.1 Aligning the remote focusing unit

- All the elements required to align the remote focusing unit are shown in Figure B.1.
- An additional alignment laser is mounted on the setup which will pass through the primary objective O1.
- Mirrors M′ and M″ give us the degrees of freedom to send the beam through the center of the primary objective. Irises I′ and I″ can be used to make sure the beam is straight.
- The beam is expanded using lenses L′ and L″ to the size of the back aperture of the primary objective O1.
- There is an alignment objective AO shown in the figure. It is not required in the beginning and thus is not mounted yet.
- From now on, I will be referring to the optical components in Figure 3.5. The collimated beam is sent through O1 and the position of the tube lens TL2 relative to O1 is set where the beam becomes collimated once again behind the tube lens.
- Then the primary objective O1 is removed and the position of the lens L3 is set where the beam is collimated again using a shearing interferometer available from Thorlabs.
- Positioning the galvo is critical to the overall performance of the system. One would think that both L3 and L4 lenses are the same, so the galvo can be placed in the middle. This is might not be true because

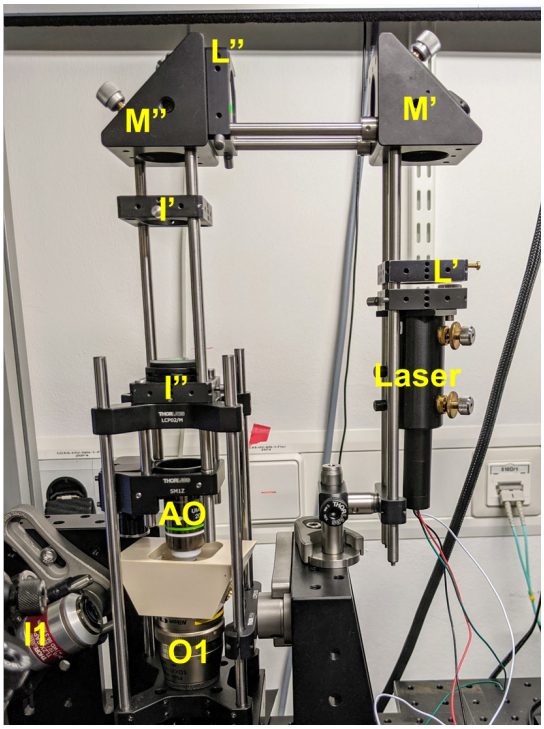

FIGURE B.1: Remote focusing unit alignment. An additional laser beam is expanded using L′ and L″ lenses. Mirrors M′ and M″ are used to align the beam through irises I′ and I″. After the beam is aligned along the optic axis of AO, irises are opened to fill the back aperture of AO.

there is 1% tolerance in focal length from the manufacturer. Using two 200mm tube lenses together, the combined focal length can be off by more than 2mm from the specified number which can create 'tilt variant scanning'.

- The focal length of both lenses L3 and L4 is measured relative to another lens by collimation method before placing into the setup and the galvo is then placed such that both foci coincide at the center of the galvo.
- The position of all the components is set using a shearing interferometer and the beam is aligned with mirrors M4, M5, M6, and M7 using irises.
- Finally, if the collimated beam passing through objective O1 comes out collimated through the objective O2, back focal planes of these two objectives are conjugated.

B.2 Aligning detection unit to the remote focusing unit

- The detection unit is mounted separately on the breadboard which can be rotated and translated.
- First, the primary objective O1 is removed and the iris is opened to allow an expanded beam to pass through the objective O2 which will be focused at the focal plane of O2. The detection unit is placed such that the secondary objective O2 and the tertiary objective O3 are lying parallel with their front windows facing each other.
- The detection breadboard is translated until the beam is collimated behind the tertiary objective.
- The tube lens is placed behind the objective O3 and the emission filter is placed in the infinity space between O3 and the tube lens.
- Now the camera is placed where that spot size is the smallest.
- Finally to check if the back focal planes of the objective O1 and O2 are conjugated properly, the alignment objective AO is mounted on the translation stage of the alignment unit (Figure B.1). When AO is translated, the spot should go in and out of focus at the same position without 'wobbling around' on the FOV.
- This is how the setup is supposed to look like following these steps:

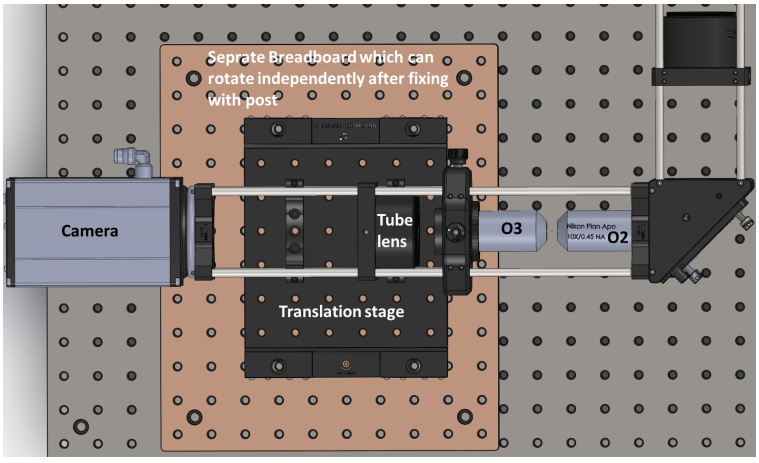

- Now a post is fixed on the optical table such that the midpoint of the post passes through the focus of the objective O2 (which is the same for

objective O3). Of course, we can't place it perfectly, but we should be as precise as possible.

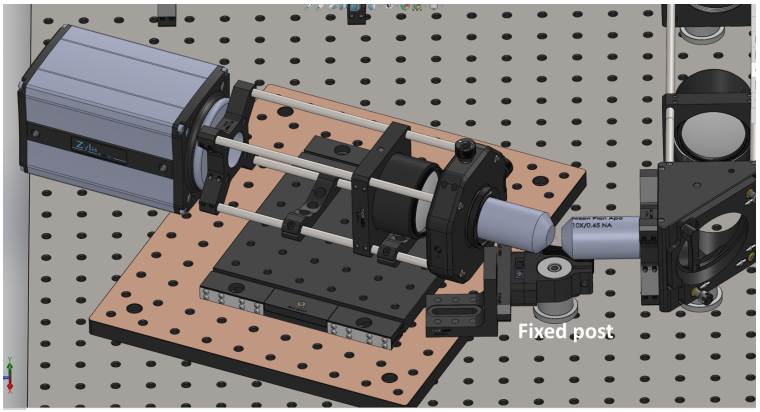

- Once the post is fixed, a clamp is attached to the post and then fixed with the breadboard on which the detection unit is mounted. This will allow us to rotate the detection unit relative to the remote focusing unit by 25 degrees.
- After rotating two things can happen if the post is not positioned exactly at the center anymore, which will most likely be the case. First, the spot is blurred, which can be easily fixed by moving the translation stage. Second, the spot has moved a bit away from the center, which can easily be fixed by the adjusting xy stage on which O3 is mounted.
- This finishes the alignment of the detection unit relative to the remote focusing unit and it is fixed in that position.

B.3 Aligning the illumination unit

- The illumination unit is assembled on a small breadboard which is fixed at an angle of 25 degrees w.r.t. the focal plane of O1.
- The objective I1 is placed on the breadboard such that the focal points of I1 and O1 coincide. This is made sure by mounting the illumination optomechanical parts on a 30mm cage system and the rods can be inserted into the holes on the chamber fixed on the detection objective for reference as shown below. There will be some imprecision in coinciding with the foci, but we have a galvo GM1 at the BFP and a mirror conjugated to the image plane of I1 and an ETL to translate and tilt the light-sheet to bring it in focus.

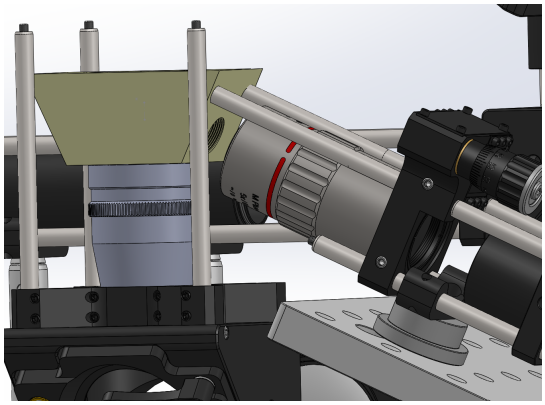

- The position of the objective I1 is fixed by sending the laser beam directly through I1 and looking at the camera, where the beam is in focus at the center of the FOV.
- All the other optical components are placed using the shearing interferometer.
- Final adjustments to the beam are done by using the mirrors and the ETL. Once the light-sheet is in focus, this finishes the alignment of the whole setup.

B.4 Protocol for microscope calibration

- During the microscope alignment, the two galvos, and an ETL have some initial values where the illumination beam can be seen in the focus on the camera with beam waist in the center of the FOV. These initial values are taken as default initial values for the galvos and the ETL.
- The step of illumination galvo is increased by one, while the ETL and the detection galvo are kept at their initial values. On the camera, one will notice that the beam will be out of focus.
- Keeping the illumination galvo fixed at this new position and ETL at its initial value, the steps of the detection galvo are increased until the beam becomes in focus again.
- The focus of the beam will shift away from the center of the FOV. The reason for this shift is discussed in Figure 3.6.
- Now the value of the two galvos is kept at these new values and the voltage is varied for the ETL until the focus of the beam moves in the center of the FOV.

- The new values for the galvos and the ETL are noted down.
- These steps are repeated with larger illumination galvo step sizes to check if the relationship between the three devices remains linear.

Bibliography

[1] Nagayasu Nakanishi et al. “Nervous systems of the sea anemone Nematostella vectensis are generated by ectoderm and endoderm and shaped by distinct mechanisms”. In: *Development* 139.2 (2012), pp. 347–357.

[2] Anniek Stokkermans et al. “Ethology of morphogenesis reveals the design principles of cnidarian size and shape development”. In: *bioRxiv* (2021).

[3] Aissam Ikmi et al. “Feeding-dependent tentacle development in the sea anemone Nematostella vectensis”. In: *Nature communications* 11.1 (2020), pp. 1–13.

[4] Michael J Layden, Fabian Rentzsch, and Eric Röttinger. “The rise of the starlet sea anemone Nematostella vectensis as a model system to investigate development and regeneration”. In: *Wiley Interdisciplinary Reviews: Developmental Biology* 5.4 (2016), pp. 408–428.

[5] Philipp J Keller et al. “Reconstruction of zebrafish early embryonic development by scanned light sheet microscopy”. In: *science* 322.5904 (2008), pp. 1065–1069.

[6] Uros Krzic et al. “Multiview light-sheet microscope for rapid in toto imaging”. In: *Nature methods* 9.7 (2012), pp. 730–733.

[7] Yicong Wu et al. “Inverted selective plane illumination microscopy (iSPIM) enables coupled cell identity lineaging and neurodevelopmental imaging in Caenorhabditis elegans”. In: *Proceedings of the National Academy of Sciences* 108.43 (2011), pp. 17708–17713.

[8] Jamie A Havrilak et al. “Characterization of the dynamics and variability of neuronal subtype responses during growth, degrowth, and regeneration of Nematostella vectensis”. In: *BMC biology* 19.1 (2021), pp. 1–19.

[9] Heather Q Marlow et al. “Anatomy and development of the nervous system of Nematostella vectensis, an anthozoan cnidarian”. In: *Developmental neurobiology* 69.4 (2009), pp. 235–254.

[10] Ashleigh E Fritz et al. "Mechanisms of tentacle morphogenesis in the sea anemone Nematostella vectensis". In: *Development* 140.10 (2013), pp. 2212–2223.

[11] P Philippe Laissue et al. "Assessing phototoxicity in live fluorescence imaging". In: *Nature methods* 14.7 (2017), pp. 657–661.

[12] Michael J Sanderson et al. "Fluorescence microscopy". In: *Cold Spring Harbor Protocols* 2014.10 (2014).

[13] Brian Herman. *Fluorescence microscopy*. Garland Science, 2020.

[14] John M Girkin and Mariana Torres Carvalho. "The light-sheet microscopy revolution". In: *Journal of Optics* 20.5 (2018), p. 053002.

[15] Bo Huang, Mark Bates, and Xiaowei Zhuang. "Super-resolution fluorescence microscopy". In: *Annual review of biochemistry* 78 (2009), pp. 993–1016.

[16] Jeff W Lichtman and José-Angel Conchello. "Fluorescence microscopy". In: *Nature methods* 2.12 (2005), pp. 910–919.

[17] Stefan W Hell. "Toward fluorescence nanoscopy". In: *Nature biotechnology* 21.11 (2003), pp. 1347–1355.

[18] Joseph W Goodman. *Introduction to Fourier optics. 3rd*. Roberts and Company Publishers, 2005.

[19] Max Born and Emil Wolf. *Principles of optics: electromagnetic theory of propagation, interference and diffraction of light*. Elsevier, 2013.

[20] Lukas Novotny and Bert Hecht. *Principles of nano-optics*. Cambridge university press, 2012.

[21] James Pawley. *Handbook of biological confocal microscopy*. Vol. 236. Springer Science & Business Media, 2006.

[22] T Wilson. "Optical sectioning in fluorescence microscopy". In: *Journal of microscopy* 242.2 (2011), pp. 111–116.

[23] Tony Wilson. "Confocal microscopy". In: *San Diego* (1990).

[24] Jan Huisken. "Multi-view microscopy and multi-beam manipulation for high-resolution optical imaging". PhD thesis. 2004.

[25] Jan Huisken et al. "Optical sectioning deep inside live embryos by selective plane illumination microscopy". In: *Science* 305.5686 (2004), pp. 1007–1009.

[26] Henry Siedentopf and Richard Zsigmondy. "On the visualization and sizing of ultramicroscopic particles, with special application to gold ruby glasses". In: *Annals of Physics* 315.1 (1902), pp. 1–39.

[27] Arne H Voie, DH Burns, and FA Spelman. "Orthogonal-plane fluorescence optical sectioning: Three-dimensional imaging of macroscopic biological specimens". In: *Journal of microscopy* 170.3 (1993), pp. 229–236.

[28] Petr Strnad et al. "Inverted light-sheet microscope for imaging mouse pre-implantation development". In: *Nature methods* 13.2 (2016), pp. 139–142.

[29] Raju Tomer et al. "Quantitative high-speed imaging of entire developing embryos with simultaneous multiview light-sheet microscopy". In: *Nature methods* 9.7 (2012), pp. 755–763.

[30] Mike Friedrich et al. "STED-SPIM: stimulated emission depletion improves sheet illumination microscopy resolution". In: *Biophysical journal* 100.8 (2011), pp. L43–L45.

[31] Philipp J Keller et al. "Fast, high-contrast imaging of animal development with scanned light sheet–based structured-illumination microscopy". In: *Nature methods* 7.8 (2010), pp. 637–642.

[32] Francesca Cella Zanacchi et al. "Live-cell 3D super-resolution imaging in thick biological samples". In: *Nature methods* 8.12 (2011), pp. 1047–1049.

[33] Patrick Hoyer et al. "Breaking the diffraction limit of light-sheet fluorescence microscopy by RESOLFT". In: *Proceedings of the National Academy of Sciences* 113.13 (2016), pp. 3442–3446.

[34] Adam Glaser et al. "A hybrid open-top light-sheet microscope for multi-scale imaging of cleared tissues". In: *bioRxiv* (2021).

[35] Elena Remacha et al. "How to define and optimize axial resolution in light-sheet microscopy: a simulation-based approach". In: *Biomedical optics express* 11.1 (2020), pp. 8–26.

[36] Sunil Kumar et al. "Application of oblique plane microscopy to high speed live cell imaging". In: *European Conference on Biomedical Optics*. Optical Society of America. 2011, p. 80860V.

[37] Florian O Fahrbach et al. "Rapid 3D light-sheet microscopy with a tunable lens". In: *Optics express* 21.18 (2013), pp. 21010–21026.

[38] Matthew B Bouchard et al. "Swept confocally-aligned planar excitation (SCAPE) microscopy for high-speed volumetric imaging of behaving organisms". In: *Nature photonics* 9.2 (2015), pp. 113–119.

[39] Venkatakaushik Voleti et al. "Real-time volumetric microscopy of in vivo dynamics and large-scale samples with SCAPE 2.0". In: *Nature methods* 16.10 (2019), pp. 1054–1062.

[40] Manish Kumar et al. "Integrated one-and two-photon scanned oblique plane illumination (SOPi) microscopy for rapid volumetric imaging". In: *Optics Express* 26.10 (2018), pp. 13027–13041.

[41] Bin Yang et al. "High-resolution, large imaging volume, and multi-view single objective light-sheet microscopy". In: *bioRxiv* (2021), pp. 2020–09.

[42] C Dunsby. "Optically sectioned imaging by oblique plane microscopy". In: *Optics express* 16.25 (2008), pp. 20306–20316.

[43] Edward J Botcherby et al. "An optical technique for remote focusing in microscopy". In: *Optics Communications* 281.4 (2008), pp. 880–887.

[44] Younghoon Shin, Dongmok Kim, and Hyuk-Sang Kwon. "Oblique scanning 2-photon light-sheet fluorescence microscopy for rapid volumetric imaging". In: *Journal of biophotonics* 11.5 (2018), e201700270.

[45] Manish Kumar and Yevgenia Kozorovitskiy. "Tilt-invariant scanned oblique plane illumination microscopy for large-scale volumetric imaging". In: *Optics letters* 44.7 (2019), pp. 1706–1709.

[46] Bin Yang et al. "Epi-illumination SPIM for volumetric imaging with high spatial-temporal resolution". In: *Nature methods* 16.6 (2019), pp. 501–504.

[47] Etai Sapoznik et al. "A versatile oblique plane microscope for large-scale and high-resolution imaging of subcellular dynamics". In: *Elife* 9 (2020), e57681.

[48] Maximilian Hoffmann and Benjamin Judkewitz. "Diffractive oblique plane microscopy". In: *Optica* 6.9 (2019), pp. 1166–1170.

[49] Hugh Sparks et al. "Dual-view oblique plane microscopy (dOPM)". In: *Biomedical optics express* 11.12 (2020), pp. 7204–7220.

[50] Leihao Chen et al. "Electrically tunable lenses: a review". In: *Frontiers in Robotics and AI* 8 (2021).

[51] HJ Landau. "Sampling, data transmission, and the Nyquist rate". In: *Proceedings of the IEEE* 55.10 (1967), pp. 1701–1706.

[52] Stefan M Jahnel, Manfred Walzl, and Ulrich Technau. "Development and epithelial organisation of muscle cells in the sea anemone Nematostella vectensis". In: *Frontiers in zoology* 11.1 (2014), pp. 1–15.

[53] Florian O Fahrbach, Philipp Simon, and Alexander Rohrbach. "Microscopy with self-reconstructing beams". In: *Nature photonics* 4.11 (2010), pp. 780–785.